Scanning Tunneling Microscopy and Spectroscopy at Low Temperatures: Development of a 1 K-Instrument and Local Characterization of Heterogenous Metal Systems

Rastertunnelmikroskopie und Rastertunnelspektroskopie bei tiefen Temperaturen:
Entwicklung eines 1 K-Instruments und lokale Charakterisierung heterogener Metallsysteme

Dissertation zur Erlangung des akademischen Grades
des Doktors der Naturwissenschaften (Dr. rer. nat.)
an der Universität Konstanz
Fachbereich Physik

vorgelegt von

Gero Wittich

Dissertation der Universität Konstanz
Tag der mündlichen Prüfung: 18.07.2005
Referenten: Prof. Dr. Klaus Kern
Prof. Dr. Günter Schatz

meinen Eltern

Zusammenfassung

Im Rahmen dieser Arbeit wurde ein Ultrahochvakuum-Rastertunnelmikroskop (STM) für Temperaturen unter 1 K mit 14 T Magnet entwickelt und gebaut. Es ermöglicht lokale Rastertunnelspektroskopie (STS) mit extrem hoher Energieauflösung und die Untersuchung physikalischer Effekte wie z.B. Supraleitung, die nur bei tiefen Temperaturen auftreten. Ferner ermöglicht die Kombination von tiefsten Temperaturen und hohen Magnetfeldern die Detektion der Zeemann-Aufspaltung einzelner Moleküle und die Untersuchung stark korrelierter Elektronensysteme. Der experimentelle Aufbau wird im ersten Teil der Dissertation beschrieben. Die hohe räumliche und energetische Auflösung des Mikroskops bei sehr tiefen Temperaturen wird mittels STS an einzelnen Co-Atomen auf einer Au(100) Oberfläche und der Messung der BCS-Bandlücke von supraleitendem Pb demonstriert. Darüber hinaus zeigen spektroskopische Messungen der Au(100)-Bildladungszustände mit hoher Ortsauflösung einen starken Einfluss der (5x27) Rekonstruktion auf die elektronische Struktur der Oberfläche.

Während unlegierte Oberflächen bereits intensiv studiert wurden, sind Struktur und elektronischen Eigenschaften binärer Metalloberflächen weitaus weniger gut charakterisiert. Im zweiten Teil werden daher STM/STS-Untersuchungen zum Wachstum von Pb auf Ag(111) und zu den elektronischen Eigenschaften der entstehenden Strukturen für Bedeckungen unterhalb einer Monolage (ML) vorgestellt. Es zeigt sich, dass Pb auf Ag(111) trotz der Mischungslücke im Festkörper eine Oberflächenlegierung in der ersten Atomlage bildet. Ein komplexer Mechanismus führt zur Legierung bei Raumtemperatur: Während des Aufdampfens von Pb bilden sich reine Bleiinseln auf der Silberoberfläche, die sich über die Oberfläche bewegen. Während dieser Bewegung gelangt das Blei durch statistische Austauschprozesse mit Silberatomen in die Substratoberfläche.

STS auf einem einzelnen Pb Atom *in* der Silberoberfläche zeigt einen gebundenen Zustand direkt unterhalb der Bandkante des Ag(111) Oberflächenzustandes aufgrund der Wechselwirkung des Pb Atoms mit dem umgebenden 2D Elektronengas. Das demonstriert die Universalität dieses Effektes, der bislang nur für verschiedene Adatome beobachtet wurde.

Durch thermisches Ausheilen von 0.33 ML Pb entsteht eine geordnete ($\sqrt{3}$x$\sqrt{3}$)R30° Pb/Ag-Oberflächenlegierung, die bemerkenswerte elektronische Eigenschaften besitzt. Ein zweidimensionaler (2D) Zustand mit parabolischer Dispersion zu niedrigen Energien hin ist in der 2D Struktur entstanden, währendhingegen die nicht modifizierte Ag(111) Oberfläche einen Shockley-artigen Oberflächenzustand mit umgekehrter Dispersion aufweist. Darüber hinaus zeigen Photoemissionsexperimente eine starke Aufspaltung des neuen Zustandes aufgrund von Spin-Bahn-Kopplung. Die gefundene Aufspaltung ist viermal größer als die des Au(111)-Oberflächezustands und kann über die resultierende Singularität in der Zustandsdichte erstmals auch mittels STS detektiert werden.

Höhere Pb-Bedeckungen bewirken aufgrund der Mischungslücke eine Segregation der Bleiatome aus der Oberfläche. Die segregierte reine Bleilage ist um 4.5° zur Substratorientierung rotiert. Dies bewirkt eine Rekonstruktion der Silberoberfläche und äußert sich in der Ausbildung eines Moiré-Musters.

Zum Abschluss werden die elektronischen Eigenschaften dieser reinen Bleilage und deren Wechselwirkung mit dem Silbersubstrat beleuchtet. Eine spannungsabhängige Umkehr des Bildkontrasts lässt sich auf den wechselnd starken Beitrag von Energiebändern, deren Bandkante sich in Abhängigkeit von der lateralen Position verschiebt, zum Tunnelstrom zurückführen. Die räumliche Ausdehnung der Elektronenwellenfunktionen in diesen Bändern verursacht vermutlich Schwebungseffekte, die zu einer zusätzlichen langreichweitigen periodischen Modulation der Zustandsdichte führen und in STM-Bildern zu sehen sind.

Contents

Chapter 1

Introduction

The Scanning Tunneling Microscope (STM) is a unique experimental tool to analyze simultaneously both, structural and electronic properties of a surface on the atomic scale [1]. While the high spatial resolution is inherent in the working principle of a STM, the energy resolution in Scanning Tunneling Spectroscopy (STS) is determined by the temperature. Very low temperatures improve the spectroscopical resolution according to $\Delta E = 3k_BT$. A high energy resolution is e.g. necessary to study many-body effects that appear on an energy scale of a few meV. Several phenomena like the Kondo effect [2], charge density waves [3, 4], magnetism [5, 6, 7] and superconductivity [8, 9], could be traced by STS already at a base temperature of 4 K.

Nevertheless "there is plenty of room at the bottom". Improving the energy resolution by making STM/STS work at even lower temperatures may result in a better quantitative understanding. Additionally there are many new effects with a critical temperature below 4 K. These concern in particular interacting electron systems like heavy fermion or p-wave-superconductors [10, 11, 12], Kondo lattices or fractional quantum hall systems. The critical temperature T_c of superconductors depends on material, size and dimensionality [13]. Studies at ultra-low temperatures regarding the influence of size and dimensionality on T_c of conventional superconductors and the interaction with magnetic nanostructures [14] are promising approaches to gain deeper insights in the nature of superconductivity and its interplay with magnetism.

In order to get access to these phenomena a STM capable to reach temperatures below 1 K has been set up. The experimental setup together with the demonstration of its performance is described in Ch. 3 and Ch. 4, respectively. Ultra high vacuum provides an environment that allows for atomically clean samples and in situ sample preparation. The implemented 14 T magnet is a further tunable parameter for the investigation of effects like the spin flip of single adatoms [15], of the spin-splitting of electronic states, or for inducing a Zeeman splitting of states in single molecules.

While in the last years structural and electronic properties of elementary metal surfaces have been studied to a great extent also by STM there is rising interest to study growth, structure and electronic properties of alloys, especially surface alloys. Surface alloying is a common phenomenon which appears for elements that are immiscible in the bulk due to their atomic size mismatch but form an alloy in the very first surface layer [16, 17]. It is an attractive method for modifying the structural and electronic properties at the surface [18]. By this surface alloying can change the chemical reactivity of a surface [18, 19], lead to improved catalytical properties [20] and induce enhanced magnetic moments [21].

The detailed STM investigation of the sub-monolayer growth of Pb on Ag(111) in Ch. 5 reveals the mechanism of surface alloying and segregation at higher coverages and yields the effect of two-dimensional faceting upon segregation which is induced by the pure Pb overlayer. The resulting electronic properties of different evolving structures are studied in Ch. 6 taking advantage of the high local resolution of a STM.

One key observation of this thesis is the formation of an ordered $(\sqrt{3} \times \sqrt{3})\mathrm{R}30^\circ$ Pb/Ag(111) surface alloy which reveals unique surface electronic properties. This surface alloy was studied by STM/STS at low temperatures and photoemission spectroscopy. The Shockley type surface state of the bare Ag(111) surface that is located in the projected Ag bulk band gap is replaced by a two-dimensional state confined to the surface alloy layer. While the Ag(111) surface state exhibits a free-electron like parabolic dispersion towards higher energies the alloy state electrons disperse towards lower energies which indicates the dominance of *p*-electrons. The photoemission measurements show furthermore, that the new state shows a strong spin-splitting. Signatures originating from the spin-splitting can be traced for the first time in the local density of states (LDOS) by means of STS.

Chapter 2

Scanning Tunneling Microscopy

The large majority of the results presented in this thesis are obtained by Scanning Tunneling Microscopy (STM) and Spectroscopy (STS) measurements. Thus, in this chapter the theoretical principles of STM and STS that are relevant for this thesis are introduced. While the basic theory of STS based on the model of Tersoff and Hamann as described in Ch. 2.2 neglects finite temperatures, the temperature dependent energy resolution obtainable in STS is discussed in Section 2.5. The improvement of energy resolution with decreasing temperature is the main motivation for building a STM working at very low temperatures.

2.1 STM Principle

The working principle of a STM is illustrated in Fig. 2.1. A bias voltage in the regime of some mV to V is applied between a sharp metallic tip and the sample. When the tip is approached to the surface up to a few Åthe wave functions of tip and surface overlap resulting in a tunneling current I in the order of some 10 pA to nA. The lateral tip position x, y and the tip sample distance z is controlled in the pm-range by applying a voltage signal to the piezoelectric scan electrode.

When moving the tip laterally over the surface a feedback loop adjusts the tip sample distance such that the detected tunneling current stays constant. The resulting z-signal is recorded and coded into a color or gray-scale image, which is the so called constant current image. Due to the exponential distance dependence of the tunneling current an extremely high z-resolution of a few

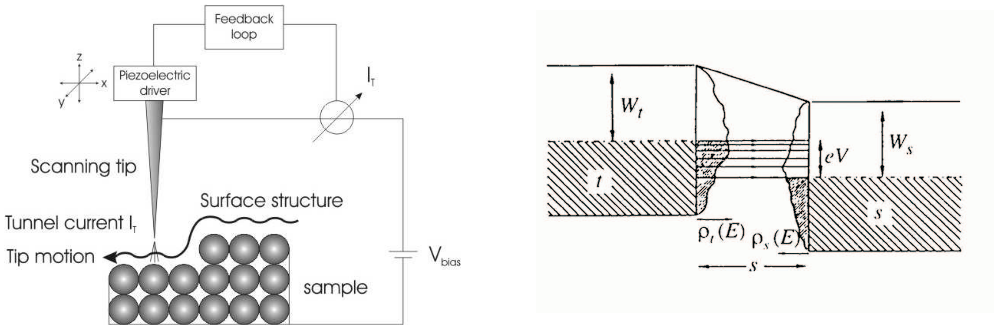

Figure 2.1: Working principle of a STM and corresponding potential energy diagram.

pm can be achieved provided the STM is stable. A further advantage of the exponential distance dependence is that the tunneling current flows mainly through the few atoms at the very apex of the tip. That allows also for a lateral resolution on the atomic scale. It costs quite some effort to achieve an optimal resolution in the real experiment (see Ch. 3.2).

2.2 Tersoff-Hamann Model

The tunneling current I can be described in the framework of the widely used Tersoff-Hamann model (TH-model) [22]. It is related to the local density of states (LDOS) of the tip $\varrho_t(\epsilon)$ and the LDOS of the sample $\varrho_s(\epsilon)$. The latter depends on the lateral tip position. In the TH-model the tunneling current $I(V)$ as a function of bias voltage V is approximated by

$$I(V) \propto \int_{-\infty}^{\infty} \rho_{\rm s}(E)\rho_{\rm t}(E-eV)\mathcal{T}(E,V,z)\left(f(E-eV,T)-f(E,T)\right)\,dE, \tag{2.1}$$

where $\mathcal{T}$ is the transmission matrix of the tunneling gap. An often used expression for $\mathcal{T}$ derived from a trapezoidal barrier is

$$\mathcal{T}(E,V,z) = \exp\left(-2z\sqrt{\frac{m_{\rm e}}{\hbar^2}(\Phi_{\rm s}+\Phi_{\rm t}-2E+eV)}\right). \tag{2.2}$$

$\Phi_{\rm t}$ and $\Phi_{\rm s}$ are the work functions of tip and sample, respectively. As mentioned above the the exponential dependence of the tip-sample distance

z governs the tunneling probability. Neglecting the finite temperature the influence of which will be discussed separately in Ch. 2.5 the fermi functions in Eq. 2.1 can be approximated by step-functions which simplifies Eq. 2.1 to

$$I(V) \propto \int_0^{eV} \rho_\mathrm{s}(E)\rho_\mathrm{t}(E - eV)\mathcal{T}(E, V, z)\; dE. \tag{2.3}$$

For experiments performed with bias voltages V close to the Fermi level $\mathcal{T}$ can be assumed to be bias independent since $V \ll \Phi$. It follows that $\mathcal{T}$ can be approximated to

$$\mathcal{T}(z) = \exp\left(-2z\sqrt{\frac{m}{\hbar^2}(\Phi_\mathrm{s} + \Phi_\mathrm{t})}\right). \tag{2.4}$$

These assumptions, i. e. zero temperature and small bias voltages, further simplify the description of the tunneling current Eq. 2.1 and finally lead to the expression

$$I(V) \propto \mathcal{T}(z) \int_0^{eV} \rho_\mathrm{s}(E)\rho_\mathrm{t}(E - eV)\; dE. \tag{2.5}$$

2.3 Topography

Topographic STM images can be obtained in two modes, the constant height mode and the constant current mode. In the constant height mode the tip stays in a constant distance from the sample surface while it is scanned over the surface. In this way height differences modulate I according to Eq. 2.1. The only image mode used in this work is the constant current mode, where the tip-sample distance z is adjusted by a feedback loop during the scan to keep I constant. Thus, to calculate a topographic image from Eq. 2.1 the current is set to a constant I_0 and the tip-sample distance z is obtained by

$$z(V, x, y) = z_0 + \frac{1}{2\sqrt{\frac{m_\mathrm{e}}{\hbar^2}(\Phi_\mathrm{s}(x, y) + \Phi_\mathrm{t})}} \ln \frac{\int_0^{eV} \rho_\mathrm{s}(E)\rho_\mathrm{t}(E - eV, x, y)\underset{\cdot}{\mathrm{E}}}{I_0}, \tag{2.6}$$

which is valid for small V and using the approximation of Eq. 2.4.

Because also the electronic surface structure can exhibit a quite strong spatial variation on the surface, always a combination of topographic and electronic surface properties is visualized in a STM image.

2.4 Spectroscopy

2.4.1 I(V) and dI/dV-Spectroscopy

In Scanning Tunneling Spectroscopy (STS) I-V curves or equivalently dI/dV-curves are measured under open feedback loop conditions. Thus, the tunneling current can be calculated from Eq. 2.5. Under the assumption that ρ_{t} and the transmission matrix $\mathcal{T}$ are independent of V the dI/dV-signal is directly proportional to the LDOS

$$\frac{\mathrm{d}I}{\mathrm{d}V} \propto \rho_{\mathrm{s}}(eV)\rho_{\mathrm{t}}(0). \tag{2.7}$$

This proportionality accounts in the limit of very low temperatures and small bias voltages.

In dI/dV images the lateral distribution of the LDOS at distinct energies is mapped. This technique is frequently used in this work and combines spectroscopic information with a high spatial resolution.

2.4.2 z(V)-Spectroscopy

While small bias voltages V close to the Fermi level can be neglected in the transmission matrix $\mathcal{T}$ in Eq. 2.4, the transmission through the tunneling gap increases exponentially with higher V. By this the dynamic range needed to acquire dI/dV spectra grows rapidly with higher V. Two different approaches are useful in this bias voltage regime to acquire spectroscopic information nevertheless. The first possibility is to take spectra with the feedback loop closed. Then the current is kept constant by retracting the tip from the surface while ramping V, thereby the dI/dV signal is reduced in dynamic range.

The alternative is to record directly the relative change of the tip-sample distance z during the voltage ramp. This is useful to map image potential states, which have been discussed quite early in STM literature [23]. The properties of image potential states and their interaction with the surface structure and defects will be discussed for Au(100) in Ch. 4.

2.5 Energy Resolution

When deriving Eq. 2.7 the temperature T was assumed to be $T = 0$. Taking into account a finite temperature in the Fermi functions in Eq. 2.1 results in a limited energy resolution of the measurement of the LDOS. A delta function $\varrho_{\mathrm{s}}(E)$ for example is measured as a gaussian in the dI/dV signal with a width of $(\Delta E)_T \approx 3k_BT$. This thermal broadening is one limiting factor in the theoretical possible energy resolution.

The dI/dV-spectra are recorded using a lock-in technique. For that the bias voltage is modulated with an AC signal V_{mod} with an amplitude between 1 and 100 mV. This leads to a decrease in energy resolution of $(\Delta E)_{LI} \approx 2.5\, e\, V_{mod}$. Considering both effects leads to an energy resolution of

$$\Delta E \approx \sqrt{(3k_BT)^2 + (2.5eV_{mod})^2} \tag{2.8}$$

This implies a thermal energy resolution of 1 meV at 4 K, 500 μeV at 2.5 K and 140 μeV at 700 mK. The description of the experimental setup in Ch. 3 will show that these values are the theoretical limit in energy resolution. Many experimental challenges have to be solved to get close to these physical limits. A great effort is necessary to reach very low temperatures while maintaining the required low mechanical and electrical noise levels.

Chapter 3

Experimental Setup: 1 K-UHV STM with 14 T Magnet

In this chapter the setup of the low temperature UHV-STM with 14 T magnet is presented. It has been developed and assembled within the frame of this work, and some challenging and crucial aspects regarding a reliable STM performance are discussed. A schematic overview over the whole system is shown in Fig. 3.1, details will be discussed in the following subsections. The UHV system (Ch. 3.1) is mounted on two frames that are decoupled from vibrations by a set of active and passive dampers, respectively (Ch. 3.2). The ^{3}He-Joule-Thomson cryostat with 14 T magnet (Ch. 3.3) is attached to the UHV system from below. The STM (Ch. 3.4) is mounted to a copper heat exchanger at the bottom of the long UHV tube reaching the center of the magnet. The horizontal and the vertical manipulator are used for sample preparation and sample transfer (Ch. 3.5).

3.1 The UHV-System

Scanning tunneling microscopy is a technique that requires very clean surfaces to work with. Clean working conditions on an atomic scale require an ultra high vacuum (UHV) environment for most of the surfaces, where all experimental steps - sample cleaning, preparation and STM measurements - have to be performed. In this section the experimental realization of the UHV environment is described.

The UHV system consists of two main chambers, the preparation cham-

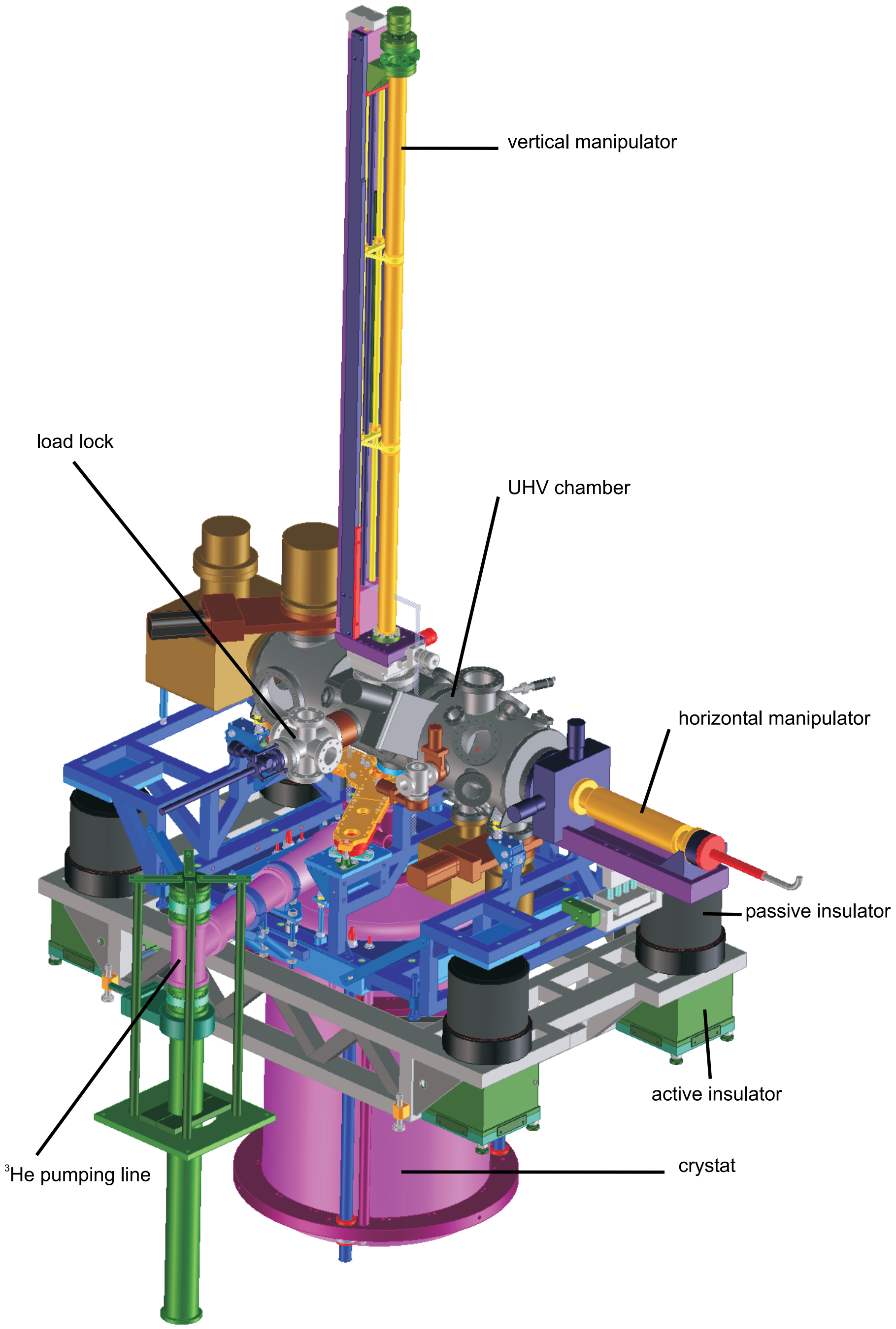

Figure 3.1: Overview over the whole STM system. The UHV-chamber is mounted on a combination of two frames that are vibrational decoupled. The cryostat with STM inside is attached from below. The ^{3}He pumping tube connects to the pump and the valve system for the Joule-Thomson cooling circuit one floor below.

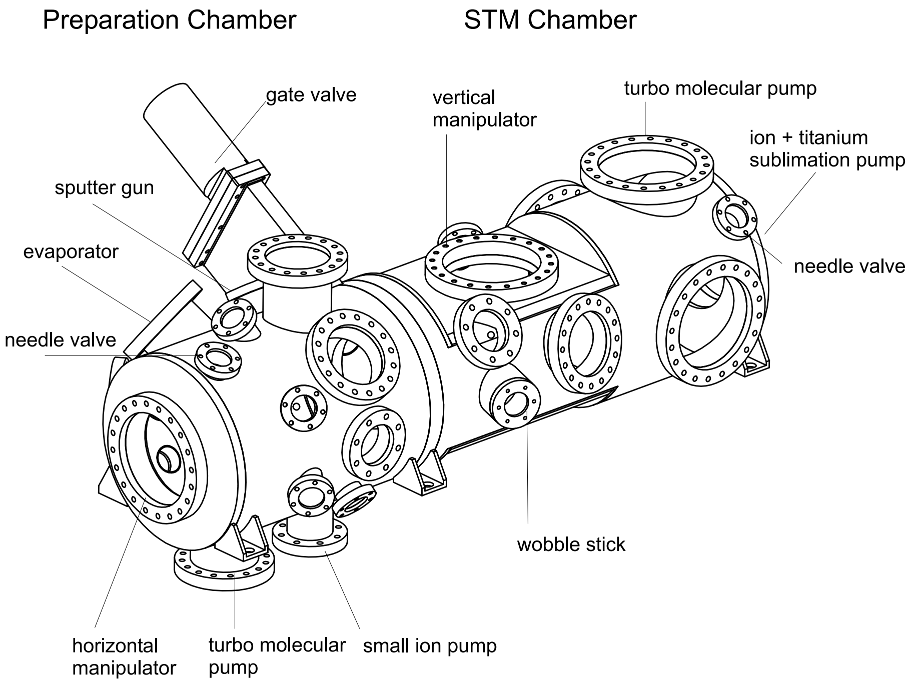

Figure 3.2: Schematic drawing of the bare UHV-chamber. It is divided in two main parts, preparation and STM-chamber separated by a built in valve. Beside various pumps, two manipulators and a "wobble stick" for the sample transfer various facilities for sample preparation are attached.

ber and the STM-chamber, which can be separated by a gate valve (see Fig. 3.2). It is made of a non magnetic steel, which guarantees the compatibility with the 14 T magnet. In the preparation chamber the samples are cleaned by means of Ar ion sputtering and successive annealing by electron bombardment. Metals and molecules can be evaporated from an electron beam evaporator or a Knudsen cell. Two evaporators are mounted to the preparation chamber. Valves between evaporator and UHV-chamber enable an exchange of evaporants without breaking the vacuum in the main system. During cleaning and preparation the sample is placed on the horizontal manipulator, which is a continuous-flow cryostat suited for cooling with liquid nitrogen and liquid helium. It will be discussed in more detail in Ch. 3.5.

In the main chamber the STM experiments are performed. A long tube extends the UHV region into the cryostat. The STM is mounted on a copper block at the end of the tube, which acts as heat exchanger (see Fig. 3.3, Fig. 3.4 and Ch. 3.3). The vertical manipulator is mounted on top of the chamber. It is used to transfer the sample to the STM; it is furthermore designed to carry exchangeable filaments to evaporate single atoms in situ on the cold sample (see Ch. 3.7.2). A fast load-lock entry is attached to the STM-chamber which offers the possibility of a fast sample or filament exchange without venting the whole system. Leak valves in the preparation chamber and the STM-chamber allow for a defined gas dosing.

Both main chambers are pumped by a turbo molecular and an ion pump each. A titanium sublimation pump is attached to the STM-chamber, while in the preparation chamber a hydrogen getter pump reduces the amount of hydrogen effectively. For STM measurements the tubomolecular pumps are switched off in order to minimize any mechanical vibrations. The prevacuum system consists of a small turbomolecular pump in conjunction with a membrane pump. This provides an oil free pumping and avoids contamination of the UHV-system. In both chambers the base pressure at room temperature is in the order of 1×10^{-10} mbar which further improves in the STM-chamber after cooling down.

3.2 Vibrational Damping

Due to the extremely close tip-sample distance of only some Å and the exponential distance dependency of the tunneling current, a scanning tunneling microscope is very sensitive to vibrations.

The whole STM system is located in the sixth floor of the institute building. Thus, beside mechanical and acoustical vibrations, also the motion of the building at low frequencies must be damped to achieve a high STM stability. The complete damping system is illustrated in Fig. 3.3. To attenuate building oscillations efficiently, which are typically in the range of 10 - 100 Hz, the *first damping stage* consists of an active damping system carrying a first frame. The feedback of these active dampers levels out the low frequency oscillations by destructive interference. The complete UHV system including the magnet cryostat is located on a *second frame* which is mounted on pneumatic passive dampers.

To decouple the STM from any noise inside the cryostat — for example boiling Helium and the vibrations of the ^{3}He pump — a *third damping stage* is implemented. It consists of three small pneumatic dampers that support

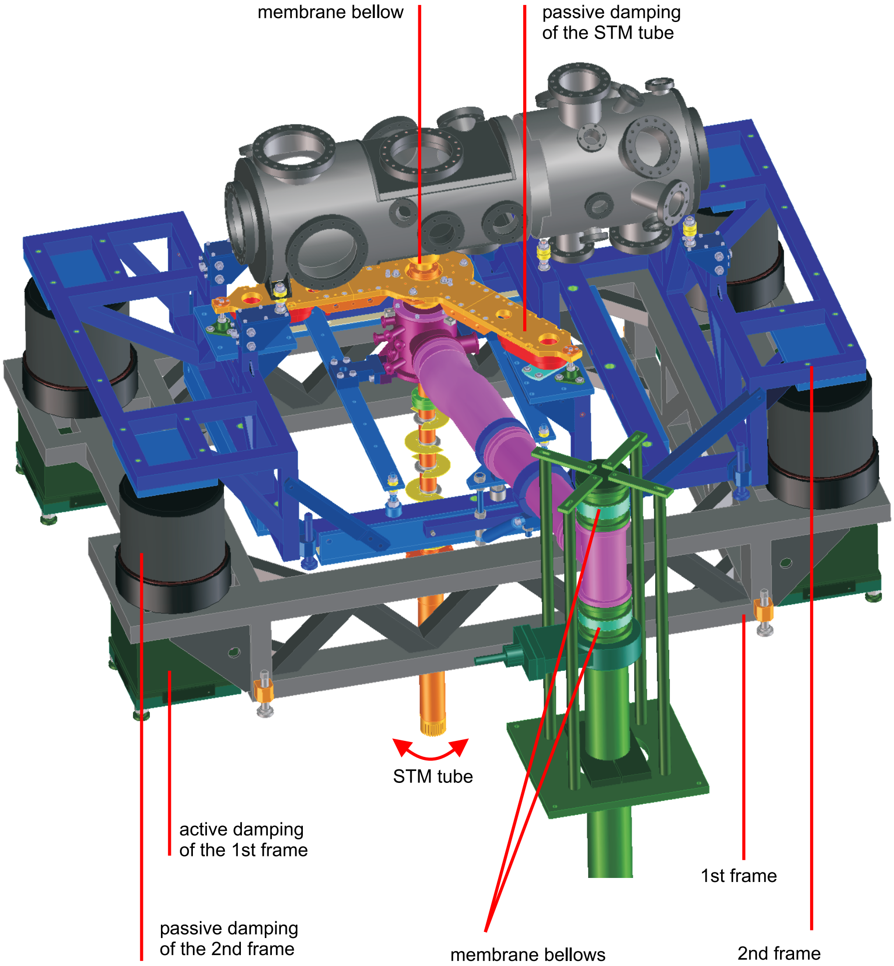

Figure 3.3: Illustration of the three main damping stages consisting of: actively damped first frame, pneumatically damped second frame and pneumatically damped STM tube that is hanging freely like a pendulum. Two membrane bellows damp the vibrations coming from the ^{3}He pump and the pumping line and two further bellows decouple the STM tube from UHV-chamber and cryostat.

the long UHV tube with the STM at the lower end via a star-like construction. This damping stage is mechanically decoupled from UHV-chamber and cryostat by two membrane bellows. By this construction the STM tube becomes a free pendulum inside the cryostat.

This third damping stage is of fundamental importance. As soon, as the tube touches the inner wall of the cryostat, the noise level increases by more than one order of magnitude. To achieve an efficient precooling of the ^{3}He for an optimal cooling power during the Joule-Thomson expansion (see Ch. 3.3) the distance between the tube and the inner wall of the cryostat should be minimized. In this setup the tube radius and the wall radius differ only by 1 mm as can be seen in Fig. 3.4. A three segmented sensor is attached to the lower end of the STM tube and to the level where the UHV tube enters the narrow cryostat region. This sensor system is absolutely necessary to level out the UHV tube by using micrometer screws.

A way to reduce the influence of any external vibrations on the STM is to rise its eigenfrequency which is above 1 kHz for the STM presented here. The effective noise level measured for this system is about 2 pm and still below 5 pm with the pump of the Joule-Thomson cooling cycle running.

3.3 Magnet Cryostat

3.3.1 Cryostat

To reach temperatures below 1 K it is no longer possible to work with only a liquid helium bath cryostat, which leads at best to the liquid helium temperature of 4.2 K. The cryostat used in the system presented here is a so called “Joule-Thomson cryostat”. A cross section is shown in Fig. 3.4. The cryostat provides a 92 l liquid helium bath as first cooling stage, which is equipped with a superconducting helium level meter. It is shielded from room temperature by a superinsulating vacuum. With this isolation no liquid nitrogen is needed for shielding.

The cryostat contains furthermore a high vacuum inset - the ^{3}He-volume - that can be pumped separately. It is embedded in the liquid He bath which acts as a precooling stage. A double walled titanium tube at the lower end of the inset can be evacuated and allows for thermal isolation from the ^{4}He-bath. The key part of the Joule-Thomson cooling cycle is a capillary that ends at the bottom of the double walled tube (not visible in the drawing). ^{3}He is compressed in the capillary to a pressure of 2 bar and expands at its end in the ^{3}He-volume which is constantly evacuated to about 0.5 mbar. This Joule-Thomson expansion of ^{3}He effects the cooling process. By instantaneously pumping the ^{3}He and compressing the exhaust

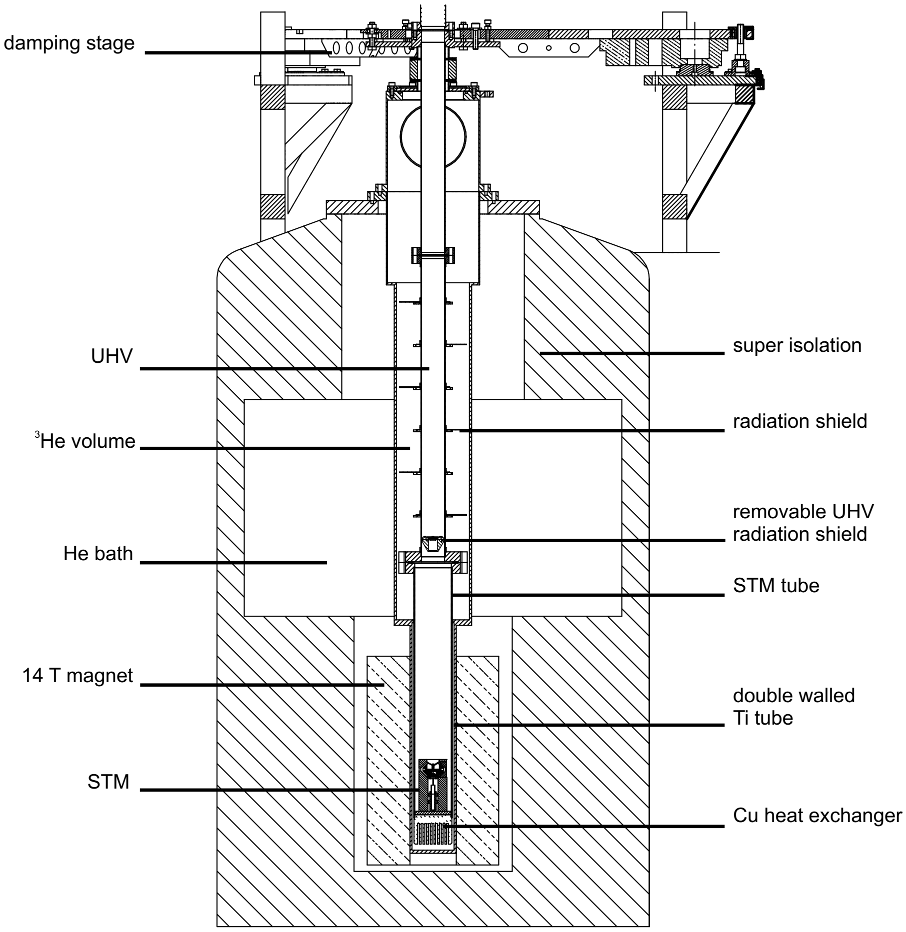

Figure 3.4: Cross section through the cryostat system with the UHV tube hanging in the high vacuum Joule-Thomson inset. The capillary (not visible here) ends directly below the copper heat exchanger with the STM mounted on top to achieve the optimal cooling performance.

back into the capillary a permanent cooling cycle is realized. For a detailed description of the working principle of a Joule-Thomson cryostat see Ref. [24]. The copper heat exchanger with the STM on top is placed directly above the ending of the capillary. This assembly releases the cooling power, which is ideally 10 J/gm at 3 K for ^{3}He, directly to the STM.

A schematic overview over the valve handling to safely run the circuit is given in Fig. 3.5. To run the cooling cycle the ^{3}He has to be suck out of the reservoir and cleaned by cycling it through a cold trap. This circuit is marked blue in Fig. 3.5. After cleaning for about half an hour the valves to the cryostat regions are opened and the Joule-Thomson process starts. The ^{3}He is then circulating on the path marked in red. The dashed red lines mark alternative paths through one auxiliary cold trap or without any cold trap. When the cycle is stopped the gas is pressed back to the reservoir along the green line. Several pressure gauges and a ^{3}He flux meter help controlling the circuit performance. Additionally, emergency valves have been installed in case that a cold trap is blocked for example. The gas is guided back to the reservoir then which avoids losses of the valuable ^{3}He. The emergency lines are plotted as thin solid lines.

The final temperature of a system is always reduced by heat intake, which has to be minimized. Beside the introduction of heat by the conduction through material like the STM tube or the cable connections also the heat radiation is an important factor for heat losses. These losses P are calculated using the Stephan-Boltzmann-law:

$$P = \sigma \cdot \varepsilon \cdot A \cdot (T_1^4 - T_2^4), \tag{3.1}$$

where $\sigma = 5.67 \cdot 10^{-8}\,\mathrm{W/m^2K}$ is the Boltzmann constant, $\varepsilon(T)$ is the emissivity of the material, A the surface of emitting or receiving body, T_1 the temperature of the body emitting and T_2 the temperature of the body receiving the radiation. Assuming an ideal emissivity $\varepsilon = 1$, a circular radiating surface with a diameter of 4 cm, a thermal emitter at room temperature ($T = 300\,\mathrm{K}$) and the receiving sample at 4 K, the resulting heat losses are 1.15 W. Decreasing the temperature of the emitter to 70 K or 50 K reduces the heat losses due to heat radiation to 3 mW or even 0.9 mW.

This simple estimation clearly shows the necessity of shielding the STM from room temperature radiation. Therefore a radiation shield is implemented in the system which can be put in the UHV tube and taken out with the vertical manipulator. Such a radiation shield is visible above the STM tube in Fig. 3.4. It is cooled by the thermal contact to the cold tube walls and thus strongly reduces the heat losses at the STM. With this shielding the STM reaches a base temperature of about 4.3 K in the normal bath cryostat configuration. Without the radiation shield the STM reaches a temperature of only about 9 K.

The lowest measured temperature with the ^{3}He-cycle running is 2.53 K. Fig. 3.6 shows that within 25 min from starting the cooling process the base

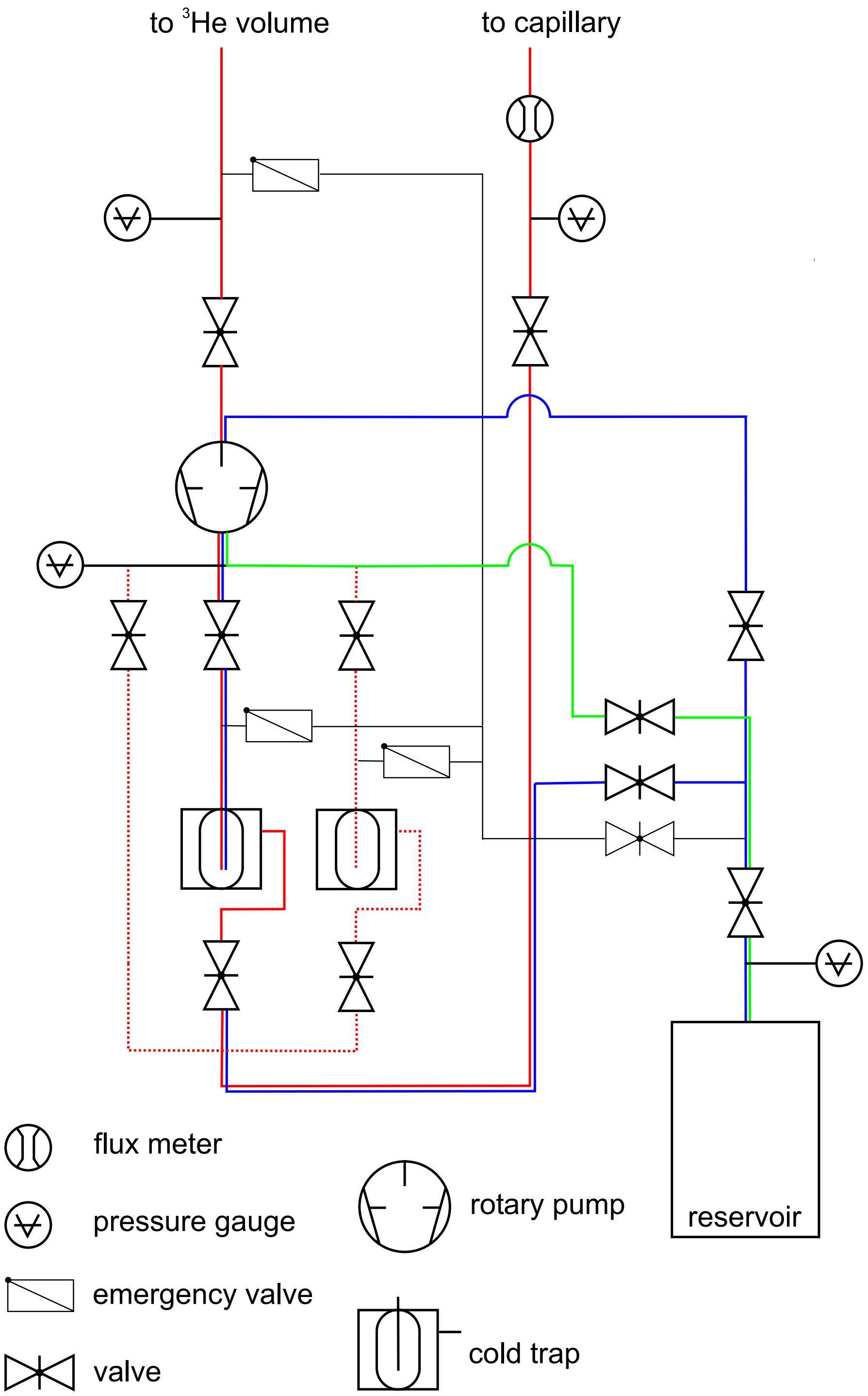

Figure 3.5: Schematic overview over the handling of the Joule-Thomson circuit. Thin lines represent the emergency lines which guide back ^{3}He escaping in case of a blocked cold trap or high pressure in the ^{3}He volume.

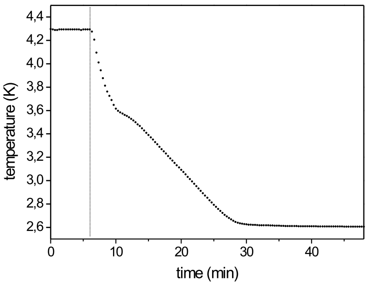

Figure 3.6: STM temperature as function of time. The dashed line marks the starting of the Joule-Thomson cooling cycle. After 25 min the base temperature is reached.

temperature is reached. This temperature is still half an order of magnitude above the theoretically reachable temperature. After running the cooling cycle for some ten minutes, one observes a decrease of the ^{3}He pressure in the capillary. This indicates that the ^{3}He has been liquified and condensed in the double walled tube. ^{3}He condensates at 0.6 K in a surrounding pressure regime of 1 mbar. This observation proves the functionality of the Joule-Thomson circuit itself. Thus, the major reason for the heat loss is expected to be an insufficient thermal anchoring of the wiring, especially of the coaxial cables.

3.3.2 Magnet

The 14 T magnet is hanging at the bottom of the liquid helium bath. It is a single coil magnet with a core diameter of 3 inches. The field homogeneity in the center of the magnet is specified to deviate only some tenth of a percent over one centimeter which guarantees an extremely homogenous magnetic field at the sample position.

3.4 STM

For the experimental setup presented here the STM has to operate reliably in ultra high vacuum at temperatures reaching from room temperature down to less than 1 K in magnetic fields up to 14 T. Due to these constraints only materials that are UHV compatible and non-magnetic like Molybdenum, Copper, sapphire or Macor are used. The STM body is machined out of a single Macor piece, which results in a high stiffness, i. e. eigenfrequency.

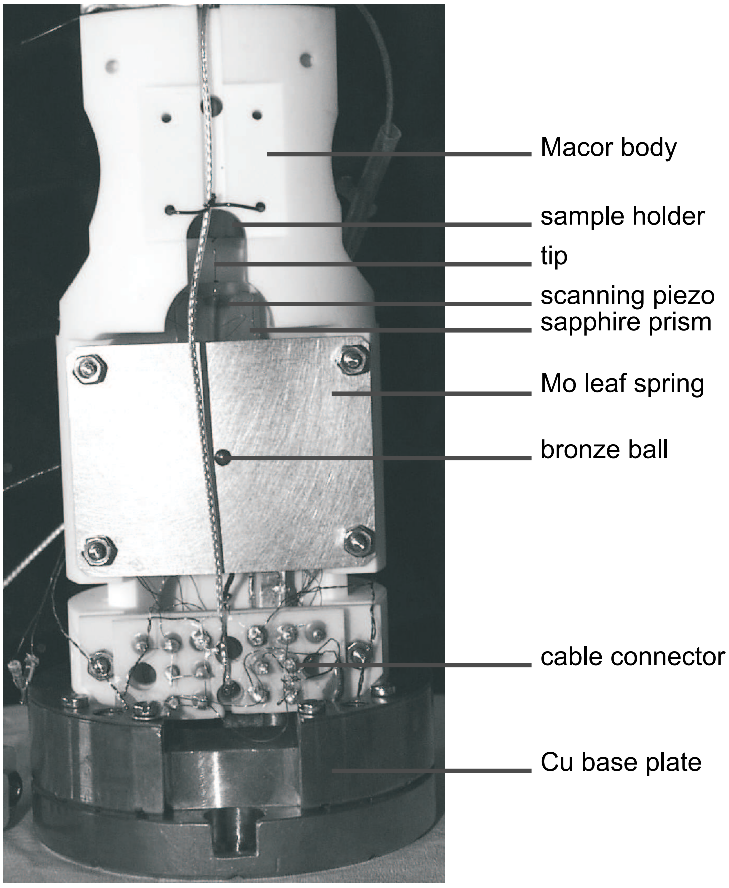

Figure 3.7: Picture of the STM as it is used. It is based on a Cu plate, directly above the wiring is connected to an Al_2O_3 adapter plate. In the middle part the tip approach is assembled (see also Ch. 3.4.1). At the upper end the sample receptacle is mounted. The tunneling current cable is crossing the front of the STM, while all other cable connections are on the back. This spatial separation minimizes electrical cross talk and interference.

Limited by the bore of the magnet it has a diameter of 46 mm and a length of 110 mm. Besides avoiding short circuits in the wiring of the STM, the advantage of a ceramic material in strong magnetic fields is, that during ramping up or down the field no eddy currents can be induced in the STM base body. These would lead to heating of the STM at low temperatures and induce instabilities due to thermal drift. A picture of the STM is shown in

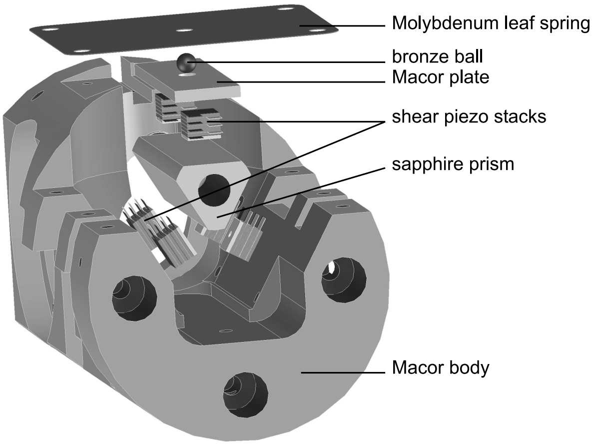

Figure 3.8: Schematic drawing of the tip approach mechanism. The sapphire prism is clamped to the Macor body by two triplets of shear piezos. By adjusting the force of the Mo leaf spring and applying an asymmetric sawtooth voltage signal to the piezos the prism makes the typical slip-stick motion due to its inertial mass and moves also against gravity.

Fig. 3.7.

The STM is mounted on a Copper base plate which is fixed to the Copper heat exchanger at the bottom of the UHV tube. At the lower end of the microscope an Al_2O_3 board with pin connectors is installed. All the electric wiring can be easily plugged and unplugged there which avoids any damages of the wires inside the STM. The sample is inserted from the top by the vertical manipulator and points downwards. Therefore the tip approach moves the tip against gravity towards the sample as will be discussed below.

3.4.1 Tip Approach

The approach mechanism has been originally designed by Pan et al. [25, 26]. In Fig. 3.8 the working principle is illustrated. A sapphire prism with polished faces is placed on four shear piezo stacks, that are glued on a V-shaped grove in the Macor body. Two more shear piezos are glued onto a Macor plate which is pressed against the sapphire prism with a Molybdenum leaf spring. A bronze ball clamped between leaf spring and Macor plate allows for an isotropic force distribution.

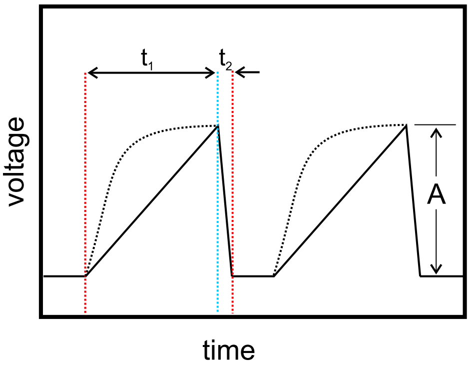

Figure 3.9: Driving sawtooth signal for the coarse tip approach. The time of the fast voltage cut of t_2 must not exceed a few μs to allow for a successful motor movement. The dashed line is the really applied signal.

All shear piezos are covered with 0.5 mm thick Al_2O_3 pads. By applying an asymmetric sawtooth voltage signal (see Fig. 3.9) simultaneously to all piezo stacks the prism moves together with the piezos during their slow shear motion, i. e. during the slow voltage ramp (ramping time t_1). During the fast voltage cut off (t_2), the sheared piezo stacks relax rapidly such that the prism remains at the former position due to its inertial mass. A periodic repetition of this slip-stick motion at the Al_2O_3-sapphire interface moves the sapphire prism over several millimeters with an accuracy in the range of some ten nanometers. The inertial slider motor is also powerful enough to move the prism against gravity.

The duration of the fast voltage cut off t_2 has to be in the order of a μs to move the piezos against the static sapphire prism. In Fig. 3.9 the time interval t_2 appears enlarged just for illustration. In contrast, the longer time for the slow voltage ramp t_1 can be chosen arbitrarily as well as its signal shape. The dashed curve shows the slow ramp signal applied in this setup. The piezo motor moves at room temperature already with a voltage amplitude $A = 70\,\mathrm{V}$, at 4.2 K an amplitude of about 220 V is needed for a reliable motion. The motor works at frequencies from 100 Hz up to some kHz and was driven at 180 Hz in the experiments.

In this context it should be mentioned, that the choice of the right material combination is crucial for a successful and reliable motor performance. The interface of slider and piezo stack defines the friction coefficients that allow for sticking of the sapphire prism and slipping at the right time scale. The Al_2O_3-sapphire interface fulfills these requirements for the whole temperature range.

Also the material of the leaf spring plays a fundamental role for a temperature independent slider movement. As the coefficient of thermal expansion is quite large for Copper-Beryllium, the leaf spring will contract by cooling down and exert a higher pressure at low temperatures. It has been experienced that the piezo motor fails after cooling down. A Molybdenum leaf spring with a three times smaller coefficient of thermal expansion keeps the force almost constant while cooling down and the sapphire prism moves still reliably.

3.4.2 Electrical Connections

All electrical connections to the STM are running from the electronics through the ^{3}He inset of the cryostat and enter the UHV at Sub-D multipin feedthroughs in the STM tube. The most sensitive connections — tunneling current I, z-scan and bias — are realized by coaxial cables to achieve the most effective screening and thus the lowest possible noise. Since all electrical leads introduce heat to the microscope, all wirings have to be thermally anchored efficiently. Inside the ^{3}He volume stainless steel coaxial cables (LakeShore) for I, z and bias and 0.1 mm thick manganin wires for all other connections have been chosen due to there low thermal but reasonable electrical conductivity. Even though they are cooled by the flow of cold He gas they are additionally glued to Cu radiation shields with GE varnish. At the STM they are again glued to the thermally anchored Macor body with epoxy glue.

Special attention has been paid to separate the tunneling current cable from all other wiring to minimize the electrical crosstalk. In addition all power cables that go inside the experiment to connect the power supplies have carefully separated from all cables connected to the STM.

3.5 Sample Handling

An easy and safe sample handling is a key issue to perform successful experiments. Several requirements have to be fulfilled for a well controlled sample cleaning, preparation, transfer and storage. All these different aspects of sample handling have to be combined and realized by a possibly simple design of the sample holder.

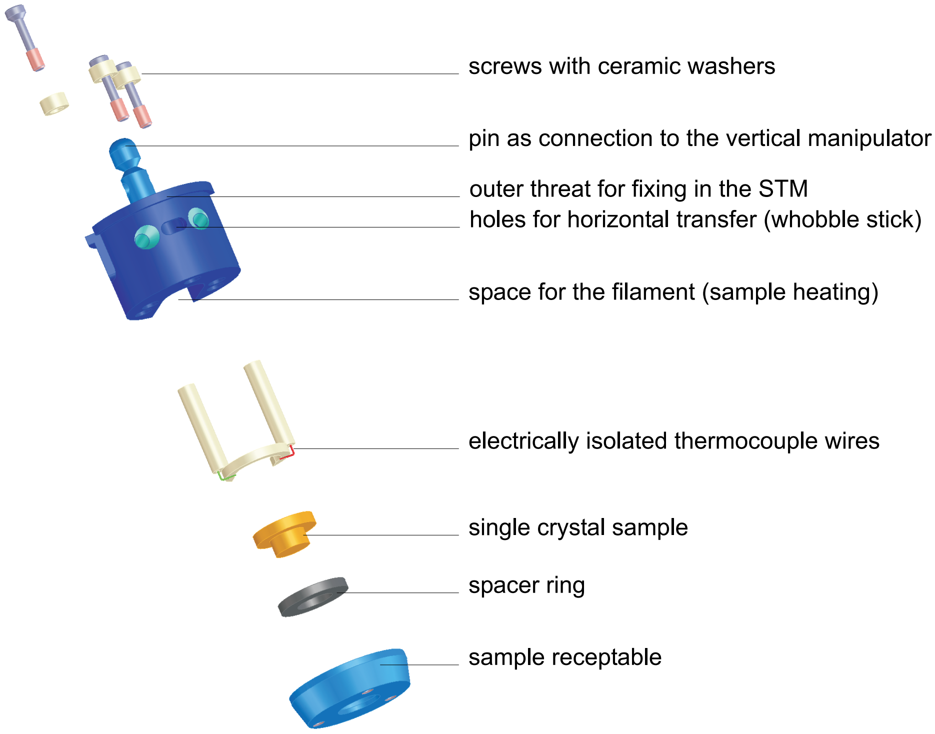

Figure 3.10: Detailed view on the sampleholder parts and construction.

3.5.1 Sample Holder

The sample holder has to fulfill the following electrical requirements: The sample has to be mounted such that it is insulated from ground. Otherwise it would neither be possible to measure the ion current from sample to ground during sputtering nor to apply a high positive voltage with respect to ground for an effective electron bombardment during annealing. In Fig. 3.10 the parts of the sample holder are shown separately. The lower part of the sample holder contains the sample. It is electrically insulated from the upper part by an Al_2O_3 ring segment and Al_2O_3 washers that prevent the screws that connect the upper and the lower part from making short contacts. In the STM the bias voltage is applied to the sample by contacting the lower part of the sample holder with a Copper-Beryllium spring.

For a controlled annealing it is also inevitable to measure the temperature directly at the sample. For this reason two “type K” thermocouple wires are guided to the sample through small Al_2O_3 tubes and form small contact areas

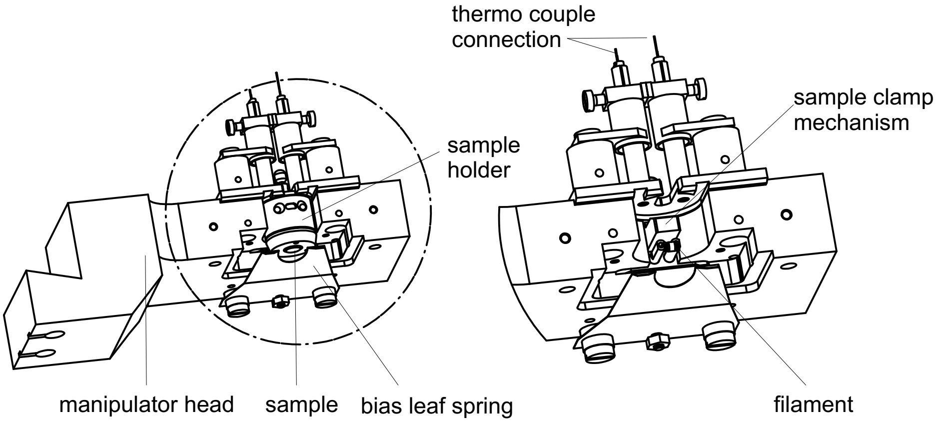

Figure 3.11: Head of the horizontal manipulator with and without the sampleholder attached.

on top of the sample holder.

Due to the high temperatures during annealing the material of the sample holder must have a high melting point. Molybdenum is the right material which is non-magnetic and combines a high melting point with a quite high thermal conductivity.

3.5.2 Sample Preparation

To clean a single crystal sample by the standard sputtering and annealing cycles it is clamped to the horizontal manipulator head as shown in Fig. 3.11. The isolated lower part is contacted via a Molybdenum leaf spring, the upper part of the sample holder is grounded. In this configuration one can measure the ion current from the sample to the ground during sputtering.

By putting the sample holder in the manipulator also the temperature measurement is enabled: A pair of thermocouple wires from the manipulator side is pressed against the thermocouple wires on top of the sample holder with a spring. This leads to a direct thermocouple connection to the sample and a reliable measurement of the single crystal temperature. The filament for electron bombardment is located in the gap at the backside of the sampleholder (see Fig. 3.10) about 1 mm above the sample. This allows for an effective electron bombardment heating up to 800 K at voltages between 300 and 400 V and a filament current of 2.6 A.

Beside cleaning the sample there are various possibilities for further sample preparation. Two evaporators can be attached to the preparation chamber simultaneously for evaporating metals or molecules via Knudsen cell or electron bombardment. Because of the load-lock system with a separate turbo molecular pump and valves between evaporators and preparation chamber they can be easily exchanged without breaking the vacuum inside the preparation chamber. In addition a needle valve is attached to the vacuum chamber, that allows for a well defined dosing of gases as well.

The horizonal manipulator is a flux cryostat suited for cooling with liquid Nitrogen and liquid Helium. Thus, the sample can be cooled down during preparation which offers the possibility to deposit single atoms or molecules and study different growth modes.

3.5.3 Sample Transfer

After cleaning and preparing the sample on the horizontal manipulator in the preparation chamber, it has to be transferred reliably to the STM. This is achieved by three transfer steps. In the first step the sample holder is picked up from the horizontal manipulator by the “wobble stick”. Its three pins fit in the holes at the front of the sample holder. The middle pin is rotatable and acts as a key that locks the sample holder and prevents it from falling off the “wobble stick”.

In the second step the sample holder is plugged to the vertical manipulator. After pulling out the “wobble stick” the transfer to the STM can start by moving down the vertical manipulator. Up to this step the transfer could still be controlled by eye. The sample has to be put into the STM without any visual control. To prevent any damages during this phase a simple mechanical sensor is implemented in the manipulator head and the applied forces are reduced and controlled.

Therefore, the manipulator head is designed such that it is pushed up elastically against three springs (Fig. 3.12) as soon as it is touching any rigid barrier like the STM in case of the sample transfer. By this an electrical contact opens indicating that the sample can be screwed in the receptacle. Two small pins at the edge of the manipulator heads ending fit in gaps in the sample holder and make its rotation possible. For taking out the sample the pin on top of the sample holder has to be fastened to the manipulator. For this procedure slightly larger forces might be applied. In that case an upper position sensor closes an electrical contact before the springs are completely compressed.

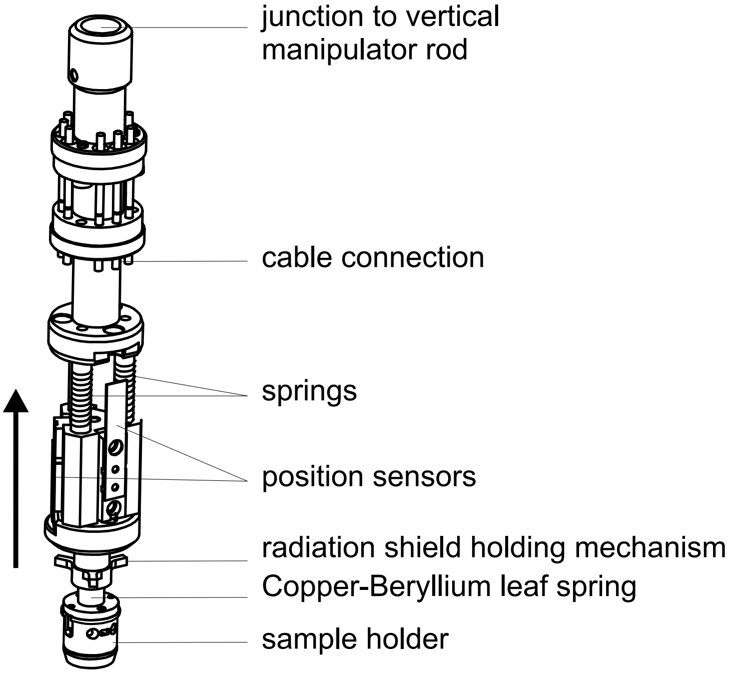

Figure 3.12: Head of the vertical manipulator with the sampleholder attached.

This mechanism also works for the transfer of the radiation shield. While the sample holder is plugged to the manipulator head the radiation shield is attached to the manipulator head and locked with the three pins by turning the manipulator about 60°.

3.6 STM Performance

In this section the topographic and spectroscopic capabilities of the new STM system are presented. A reference sample to test the topographic STM stability and spectroscopy is the Au(111) surface which has been imaged in Fig. 3.13a. The monatomic step appears sharp and the 22 x $\sqrt{3}$ "herringbone" reconstruction of the surface with alternating fcc and hcp stacking regions (see also inset) is well resolved. From that image one can derive that the topographic noise level is below 3 pm. The dI/dV-spectrum plotted in Fig. 3.13b yields the onset of the Shockley type surface state at -0.51 eV in good agreement with low-temperature STS [27] and photoemission [28]

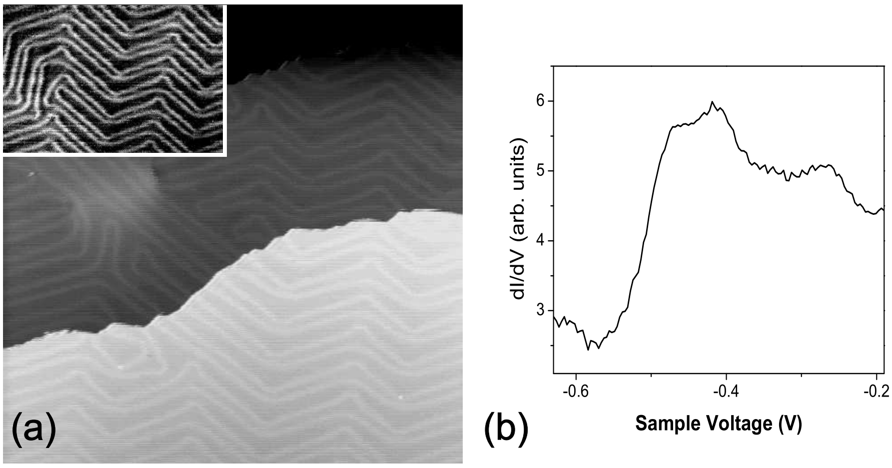

Figure 3.13: (a) 80×80 nm^2: STM image of the Au(111) with the $22\times\sqrt{3}$ “herringbone” reconstruction. (b) dI/dV-spectrum showing the onset of the Shockley type surface state at -0.51 eV.

results.

The Au(100) surface is an other low index face of a gold single crystal. It exhibits a quasi-hexagonal surface reconstruction that will be discussed in more detail in Ch. 4 in the context of its electronic properties. Besides the reconstruction lines also steps and boundaries separating two equivalent domains of the reconstruction are visible in Fig. 3.14. On can see that impurity atoms have nucleated at step edges and domain walls. The Au(100) surface was used to demonstrate the high spatial resolution of the new STM system also in spectroscopical measurements. For that purpose a minute amount of Co atoms has been evaporated on the surface with a commercial electron beam evaporator at a substrate temperature of 200 K. Immediately after the preparation the sample was transferred back to the STM. By this procedure single Co atoms remain isolated on the surface as shown in Fig. 3.15a. Their preferential adsorption site is on top of the reconstruction lines and at the crossing points of two reconstruction lines. The local electronic structure of the adatom is revealed by Scanning Tunneling Spectroscopy (STS).

In Fig. 3.15b a dI/dV spectrum acquired on top of a Co adatom is plotted in direct comparison with an “off-spectrum‘” on the bare Au(100) surface. While the “off-spectrum” is flat, a strong feature around the Fermi energy is apparent in the spectrum on the Co adatom. It can be fitted by a Fano line

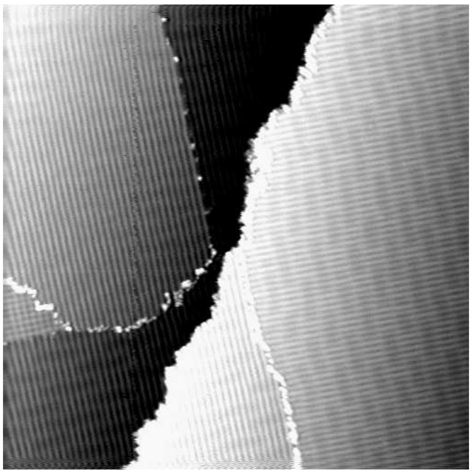

Figure 3.14: $90{\times}90\,\mathrm{nm}^2$: STM image of the bare Au(100) surface. The quasi-hexagonal reconstruction is apparent. Impurity atoms have nucleated at step edges and domain walls.

shape. This line shape is characteristic for the Kondo effect which is due to a resonant coupling of the adsorbate spin with the substrate electrons [29]. The fit result is a Kondo temperature $T_K = 286\,K$. It is significantly larger than the various T_Ks measured on different noble metal surfaces. Further measurements are necessary to reproduce the results and to clarify if this large value might be due to the influence of the reconstruction. This example in Fig. 3.15b proves that the STM is mechanically stable enough to record dI/dV point spectra on top of single atoms.

BCS - Gap

The results on different gold surfaces have been obtained at temperatures around 9 K. During these experiments the radiation shield was not in place (see Ch. 3.3.1). An appropriate way to demonstrate both, very low temperatures and high spectroscopical resolution is to resolve the BCS-gap of a superconductor. According to the theory of Bardeen, Cooper and Schrieffer (BCS-theory) [30], an energy gap around E_F opens in the density of states when a material becomes superconducting below the transition temperature T_c:

$$\varrho(E) \propto \frac{|E|}{\sqrt{E^2-\Delta^2}} \qquad |E| > \Delta, \tag{3.2}$$

$$\varrho(E) = 0 \qquad |E| < \Delta, \tag{3.3}$$

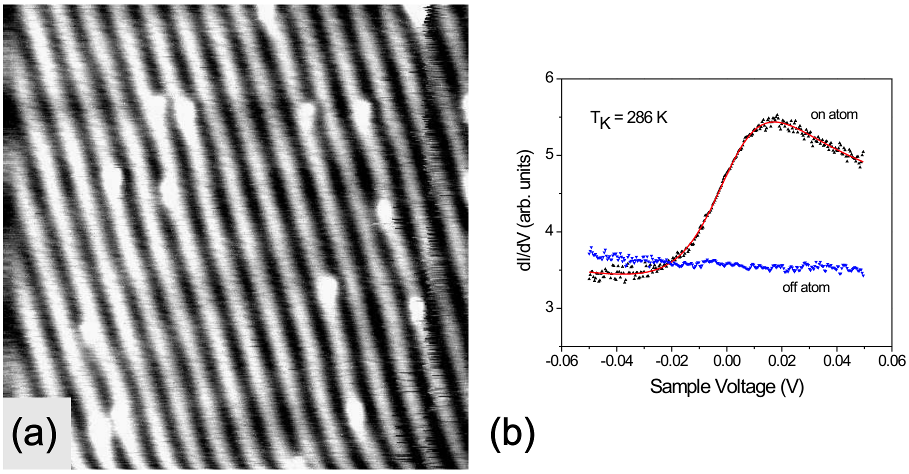

Figure 3.15: (a) 20×20 nm^2: Single Co atoms on the Au(100) surface. The preferential adsorption site is on top of the reconstruction lines and their crossing points. (b): Spectrum on top of a single Co atoms and off spectrum.

where the $T = 0\,K$ gap energy Δ is related to the critical superconducting temperature T_c by $\Delta = 1.764\,k_B\,T_c$. Therefore, a Pb crystal with a critical temperature of $T_c = 7.2\,K$ has a gap energy $\Delta = 1.3\,\text{meV}$. Because in STS the gap is measured symmetrically around E_F the resulting width is 2Δ. At finite temperatures the gap gets smeared out and a nonzero signal remains also in the gap region.

From the experimental point of view, also the amplitude of the Lock-In signal, radio frequency (RF) noise and drift effects during the measurements are factors that contribute to a broadening of the observed gap feature.

A Pb(111) single crystal was used to demonstrate the capabilities of the STM regarding low temperatures and high resolution spectroscopy. It was prepared by several cycles of sputtering and annealing at 450 K. Two tunneling spectra recorded on the Pb(111) surface at 4.3 K and 2.6 K are plotted in Fig. 3.16. For both spectra a gap feature symmetrical around E_F is evident. At 2.6 K this feature is more pronounced and the gap is deeper. The different vertical position of the maxima in the dI/dV signal is due to the slightly different tunneling contact impedances of 8.7 MΩ and 10 MΩ of the red and the black curve, respectively. The width of the gaps is 6.8 meV for the spectrum at 4.3 K and 5.6 meV for the measurement at 2.6 K.

The observed gap feature is explained by assuming a tip which is covered

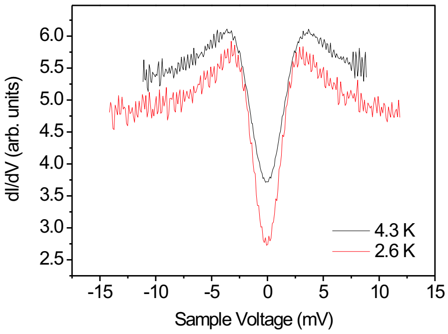

Figure 3.16: BCS-gap of Pb measured with a superconducting Pb tip at 4.3 K and 2.6 K.

with Pb and thus superconducting. In this case one expects the spectra of a superconductor-insulator-superconductor (SIS) junction. Such spectra show maxima at $\Delta_s(T_s) - \Delta_t(T_t)$ and $\Delta_s(T_s) + \Delta_t(T_t)$, where $\Delta_s(T_s)$ and $\Delta_t(T_t)$ are the temperature dependent energy gaps of sample and tip, respectively. The signal of the maximum inside the BCS-gap is still covered by the residual noise of the experiment.

It is reasonable to expect a superconducting Pb tip, because the tip is generally dipped into the sample several times to obtain optimal imaging conditions. Furthermore it is well known that Pb tends to jump to the tip and form a neck contacting tip and sample [31]. When approaching to the Au(100) surface the first time after the experiments on the Pb(111) surface the tip lost a large amount of material polluting the surface in the range of a micrometer, which is an other indication for a Pb coated tip. The measured superconducting gap spectrum proves that the spectral resolution of the STM system is below 1 meV.

3.7 Outlook

3.7.1 Next STM Generation

The next optimized STM which is slightly modified is already set up and will replace the Macor STM used so far soon. Two major improvements — a new material and a rotatable sample holder — have been implemented as will be discussed below. Furthermore it will be mounted in a new UHV tube with a 1 mm smaller radius. Thus, it will be much easier to avoid any mechanical contact with the cryostat resulting in more stable and better controllable measurement conditions.

Shapal STM

The new STM is made of Shapal M which combines both, the benefits of a metal and of a ceramic. While it is still a non magnetic insulator with a small thermal expansion coefficient, it has a thermal conductivity a hundred times higher than Macor. This will strongly reduce thermalization times for cooling down, sample transfer and running the Joule-Thomson cooling cycle. Its low temperature compatibility for the tip approach mechanism have already been proven by testing it in a liquid-He glass cryostat. Also the STM is tested at ambient conditions and shows the same stability as the Macor STM. The scanning piezo can be easily unmounted from the sapphire prism. This allows for an implementation of a tip exchange mechanism by just replacing the piezo by a suitable scan head.

Rotor

The possibility to rotate the sample around the horizontal axis has several advantages. First it is helpful to change the scanning area on the crystal surface. So far, this was achieved by turning the sample holder with the vertical manipulator which in consequence requires thermalization time before measurements can be continued. With the rotor only a few tenth of degrees of rotation are sufficient to reach a new spot on the surface. With the sample face rotated upwards it will be also possible to evaporate single atoms in situ on the cold sample as will be described in Ch. 3.7.2.

The rotor is illustrated in Fig. 3.17. It is driven by a piezo motor similar to the one of the tip approach. Two sapphire cones are glued to the Molybdenum rotor body. The rotor is clamped between two triplets of shear piezo stacks that are reversibly mounted on the Mo rotor holders. Al_2O_3 pads are glued on top of the piezo stacks. By this, the reliable Al_2O_3-sapphire interface for the slip-stick motion is obtained. One of the rotor holders is fixed rigidly to the Shapal body while the other one is pressed against the rotor by a Mo leaf spring to tune the clamping force. The spring is fixed only in the center of the holder such that the holder stays flexible and self adjusting during the entire rotor motion.

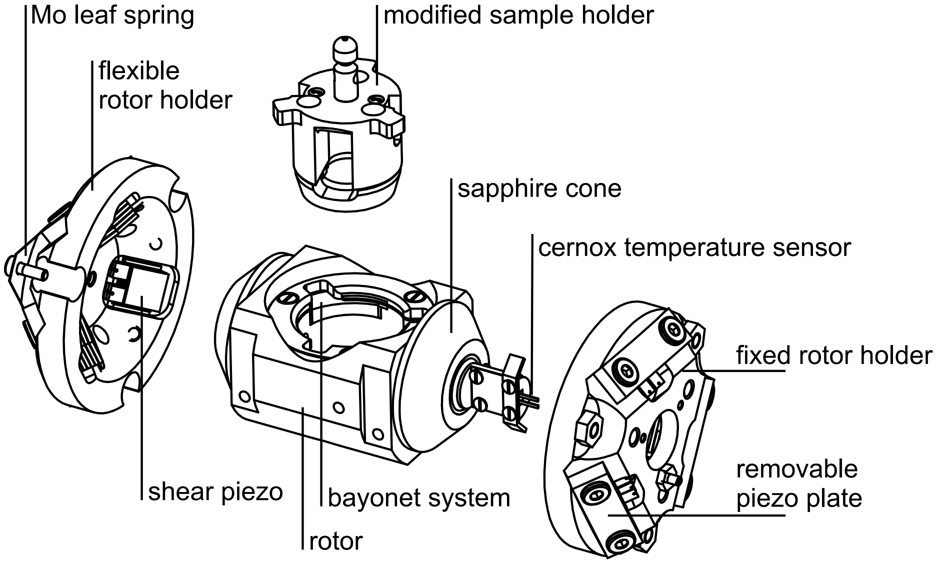

Figure 3.17: Schematic drawing of the rotor that allows for a sample rotation in the STM. This is helpful to change the scanning area on the crystal surface. With the sample face pointing upwards single atoms can be evaporated in situ at low temperatures.

The sample is fixed in the rotor body by a bayonet mechanism in contrast to the Macor STM where the sample was screwed in a thread in the sample receptacle. In that case it takes several turn arounds of the sample holder to be fixed and when taking out the sample it is difficult to judge if the sample holder is lose already or still inside the thread. The bayonet has been chosen because it takes only a third of a turn around to fix the sample holder in a well defined, reliable and reproducible way.

3.7.2 In Situ Evaporation

The vertical manipulator is designed such that filaments of different materials can be picked up like a sample holder and moved down towards the STM. In combination with the rotor it will be possible to evaporate single atoms in situ on the cold sample which is rotated by 180° for this purpose. This facility offers the possibility to study electronic properties of single adatoms also on crystal surfaces with a very low energy barrier for surface diffusion like the noble metal (111) surfaces. Because filaments can be exchanged fast

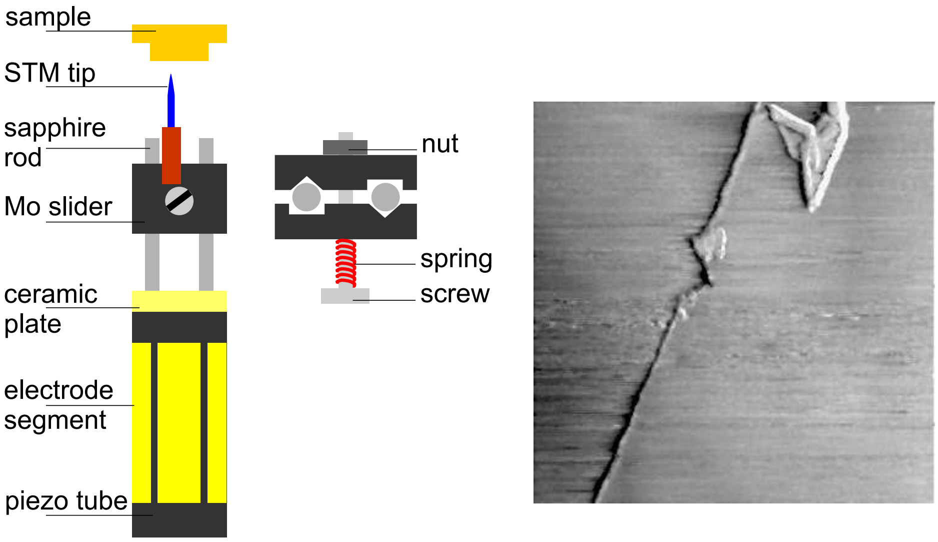

Figure 3.18: Schematic drawing of the mini-STM design. A first STM image on graphite at ambient conditions shows a monatomic step.

and easily it is a flexible and versatile way for in situ preparation.

3.7.3 Mini STM

As alternative to the STM design realized in the Macor and the Shapal STM as discussed above a STM with different design has been developed in parallel. It is based on the approach system developed by Renner *et al.* which just needs a piezo tube to move up and down a slider on two parallel sapphire rods [32]. Also in this case the slider movement is based on the slip-stick mechanism. By applying a cycloidal voltage signal to the piezo electrodes the slider follows the slow piezo movement and keeps its position during the rapid relaxation of the piezo due to its inertial mass. Renner uses one piezo tube for the approach of the sample to the tip and an additional smaller scanning tube with the tip attached which is placed inside the approach piezo.

The design presented here merges the approach and scan facility in one single piezo tube. The slider carries the tip and approaches to a fixed surface.

The piezo tube has four electrode segments on the outer and one electrode on the whole inner face. To gain an elongation of the tube in the approach mode the four outer electrodes are connected forming one large z-electrode with the inner electrode kept on a fixed potential. After reaching the tunneling contact the outer electrodes are disconnected and drive the scan movement in x- and y-direction while the inner electrode controls the z-movement.

A first STM image of graphite at ambient conditions in air is shown in Fig. 3.18. Only one pneumatic damper was used to damp the mechanical noise. However, one can clearly recognize a monatomic step crossing the image from the lower left to the upper right. The image quality proves the high stability and functionality of this STM design.

The advantages of this STM are obvious: It is very small — about 1 cm in diameter and less then 4 cm long — and light. Thus, it is well suited for experiments with spatial constraints. Its low mass rises the eigenfrequency and thus increases the stability. It is suited for UHV conditions and high magnetic fields. Even more the approach mechanism works at 4 K and below as has been tested in the liquid-He glass cryostat and reported by Renner. Only seven cables have to be connected to run the STM. This is advantageous for applications at very low temperatures like some mK, because any heat loss has to be minimized to reach this temperature regime. In addition the setup becomes more simple and robust.

Chapter 4

Reconstruction and Image Potential States on Au(100)

In this chapter a study regarding the influence of the Au(100) surface reconstruction and surface defects on the image-potential states is presented. A surprisingly strong shift of the image state onset energy at surface defects is observed. Also at reconstruction lines a significant modulation of the state onset is found and discussed in terms of changes of the electronic configuration and of the work function on a local scale. The measurements presented here have been performed using the new STM system.

Image-potential states are quantized electronic states that are confined in front of a metal surface. These states can be populated by exciting an electron from the Fermi level to almost the vacuum level by optical means [33] but also by injecting electrons into the states by STM [23]. The electrons are then bound by the attractive image potential which originates from the Coulomb interaction between the electron and its image charge in the crystal. The image charge is the net result of the interaction of the electron with all electrons in the surface. Similar to surface states the crystal potential prevents the propagation of electrons into the crystal [34]. The appearance and the electron dynamics of image-potential states have been investigated by means of inverse photoemission [35, 36] and two electron photoemission [33, 37, 38] in great detail.

It has also been demonstrated that scanning tunneling spectroscopy is a powerful technique to detect image-potential states. They appear at sample bias voltages of 4-8 V. The electric field between tip and sample induces a Stark shift of the states' energetic positions towards higher energies [23, 39],

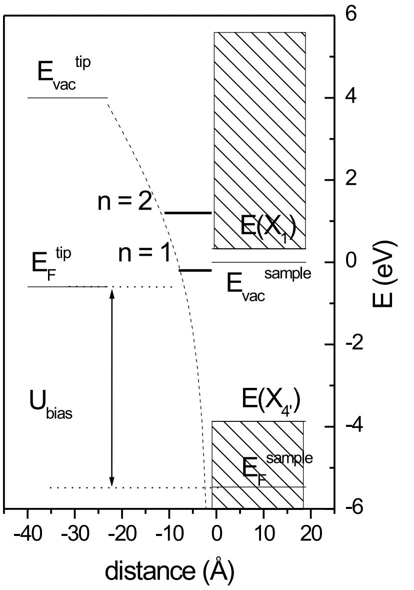

Figure 4.1: Schematic drawing of the energy levels of the image potential states, the Fermi levels of tip and sample, the bulk band edges of the Au(100) crystal [$E(X_{4'})$ and $E(X_1)$] and the potential in the tunneling gap (dashed line).

but does not influence the motion of the electrons parallel to the surface [39]. Fig. 4.1 shows schematically the resulting energy level diagram. It was found that the electronic structure of a surface influences the energetic position of the image-potential states significantly [23, 40]. Thus the image-potential states can be used to achieve chemical contrast for metals on metal surfaces on the nanometer scale [40, 41].

The $z(V)$-spectroscopy is an appropriate tool to measure the energies of the Stark-shifted image-potential states (see Ch. 2.4.2). A typical spectrum is plotted as red solid line in Fig. 4.3b. The first two image-potential states can be identified at 5.27 and 6.67 V, respectively. These are the energies of the Stark-shifted states as measured from the Fermi energy of the sample.

By STS it will now be demonstrated that the image potential states are influenced laterally by changes of the electronic structure of a pure Au(100) surface due to reconstruction, steps and surface defects. The STM image in Fig. 4.2a reveals the quasi-hexagonal (5×27) reconstruction of the Au(100) surface which is schematically drawn in Fig. 4.2b [42]. The driving force for

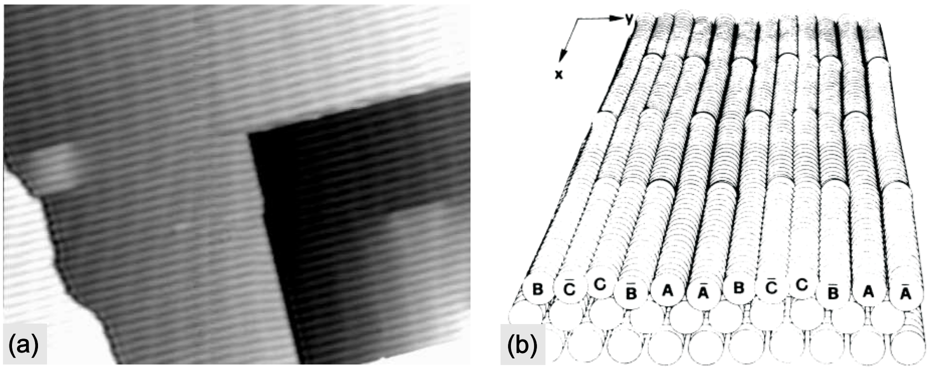

Figure 4.2: (a) $68\times50\,\mathrm{nm}^2$, The reconstructed Au(100) surface. (b) Model of the quasi-hexagonal reconstruction [42].

the reconstruction is the minimization of the surface energy by increasing the atom density which results in larger overlap of s- and d-orbitals. The small parallel rows are oriented approximately along the $\langle 110\rangle$ direction and have an apparent height of 40 pm. Two atomic rows form the dark and the bright lines, respectively. They a separated by a further single atomic row forming an AABCCB order. The contraction in the perpendicular direction induced by the increase in density is not uniform but localized in soliton-type regions, stacked to give rise to a slightly distorted and about 10 pm high rectangular superlattice.

At the left and the right border of the STM image two surface defects that are oriented along the atomic rows are visible. Fig. 4.3a is a zoom in such a defect. The reconstruction lines perpendicular to the surface defect are obviously distorted. In Fig. 4.3b the $z(V)$ spectrum on the bare Au(100) surface is compared with the spectrum on the upper edge of the surface defect. It appears that the image state onset energy at the defect site has strongly decreased by 0.3 eV. Furthermore the prior steep step-like onset has smeared out. For a more detailed and spatially resolved analysis of this effect $dI/dV(E,x)$ spectra across the surface defect have been recorded with the feedback loop closed. The dI/dV signal is plotted in gray scales as function of the lateral distance x and of bias energy $E = eV$ with respect to E_F in Fig. 4.3d. The spectra are taken along the first scan line of the topographical image in Fig. 4.3c. This spectra plot reveals nicely the site dependent relative energy shift of the image potential states. The strong energy shift induced by the surface defect is confirmed by this spectroscopy method. The lateral

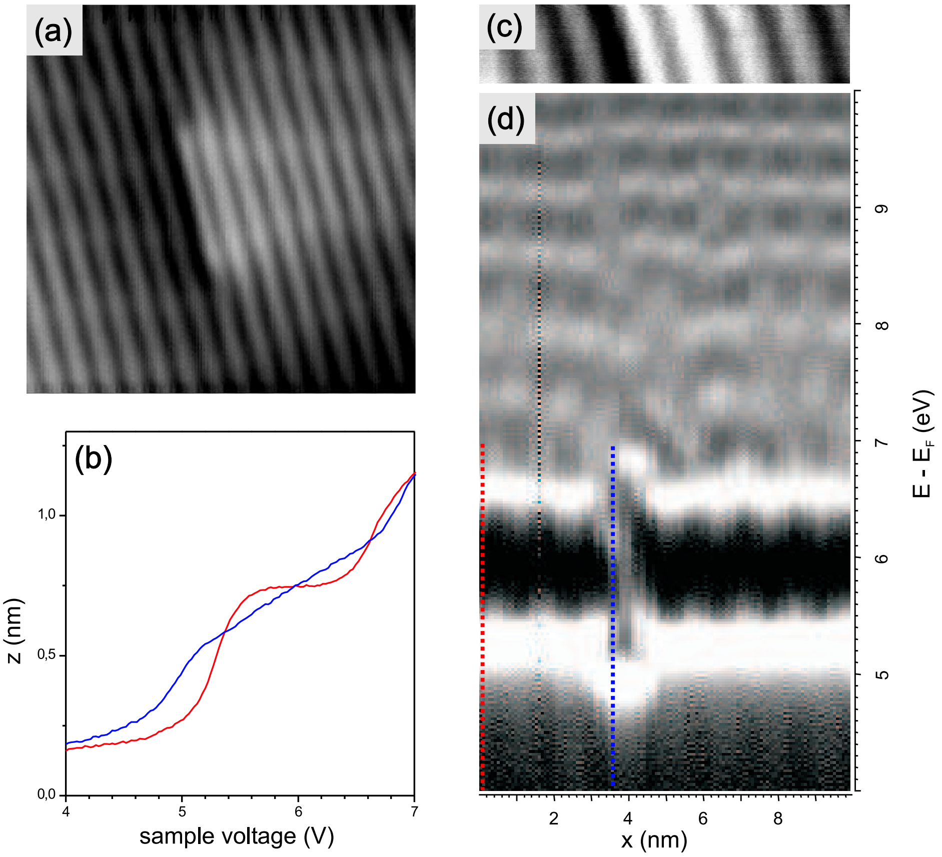

Figure 4.3: (a) 20×20 nm^2. Surface defect along the atomic rows of the reconstruction. (b) $z(V)$ spectra on top of the defect (blue line) and on the bare Au(100) terrace (red line). (c) Scan across the defect. (d) Plot of the differential conductance dI/dV as function of the lateral distance x and of bias energy $E = eV$ with respect to E_F. The spectra are taken along the first scan line of the image (c).

extension of the shift is found to be 1.3 nm.

The local density of states on the surface at distinct energies is furthermore recorded in dI/dV images of the image state regime. A sequence of 11 dI/dV images in the bias voltage range from 5.01-5.65 V is shown in Fig. 4.4. This range covers the whole ascending step in the $z(V)$ spectrum (red line in Fig. 4.3b). The first image resembles the corresponding topography. The white arrow points towards one of the surface defects apparent in this sur-

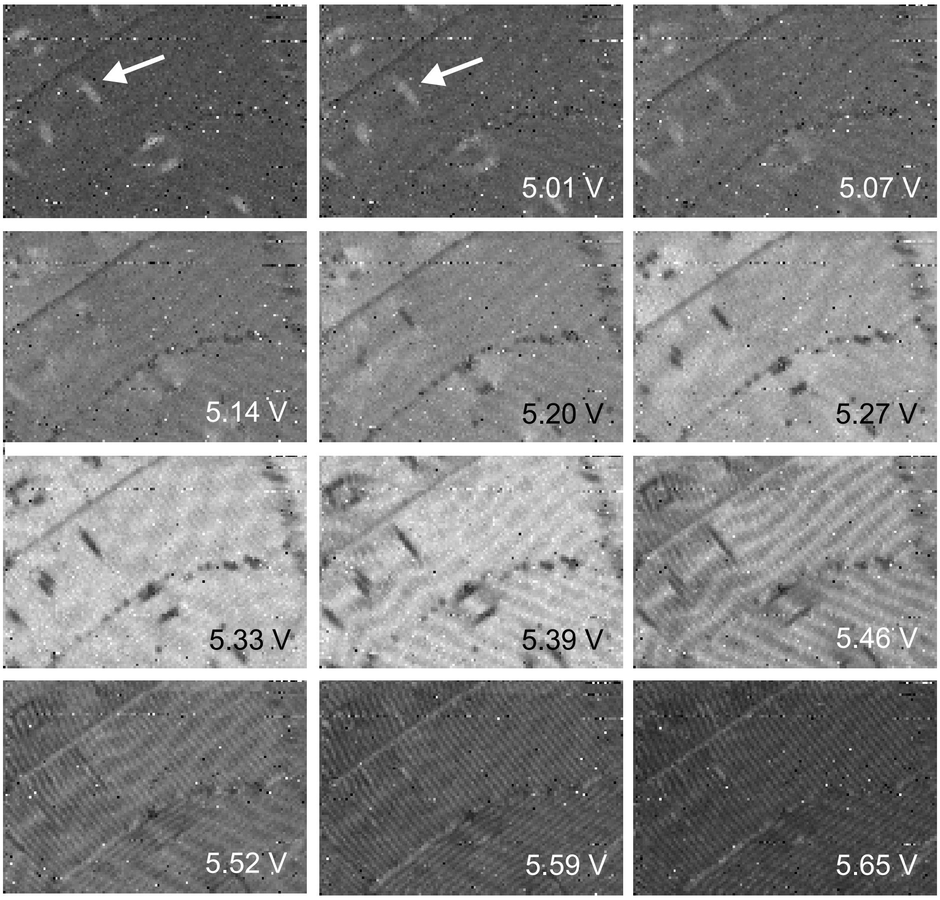

Figure 4.4: $60{\times}42\,\mathrm{nm}^2$, topography of Au(100) (first image) with a sequence of 11 corresponding dI/dV images recorded with increasing bias voltage. The white arrow marks one surface defect

face area. Following the sequence, a strong change in image contrast can be observed. At low bias voltages only the surface defects appear bright due to the energy shift just described. While at higher voltages the surface defects appear black the intensity of the terraces increases gradually accompanied by a change in the reconstruction appearance. At 5.46 V bright distorted rectangular reconstruction lines dominate the image contrast. Their contribution gets weaker again on cost of the reconstructed atomic rows that remain visible up to 5.65 V.

The comparison of this technique with the mapping of the local work function by recording the $d(\ln I)/ds$ signal [43] shows that the observed effects do not originate from changes in the work function at the surface defects and the reconstruction lines. At monatomic steps in contrast a strong downward shift of the work function by more than 1 eV is observed due to the Smoluchowski effect [44] analogous to Ref. [43]. According to Smoluchowski, redistribution or smoothing of the electron cloud at surface protrusions can reduce the kinetic energy of the electrons and thus the total energy of the surface [45, 43]. Charge flows from the top region of the step towards the lower corner. This leads to the formation of local dipoles that are antiparallel to the normal surface dipoles of flat surfaces which finally results in the observed lowering of the work function in the direct vicinity of the step. This effect is only very weak at surface defects and the surface reconstruction lines.

Thus, the dI/dV images at image state energies are an impressive demonstration of the sensitivity of the image-potential states on changes in the surface electronic structure despite only minor changes in the local work function. It appears that already corrugation changes in the order of some ten pm due to the surface reconstruction strongly influence the local electronic band structure at the surface.

Chapter 5

Sub-Monolayer Growth of Pb on Ag(111)

The investigations of epitaxial growth processes are triggered by the aim to fabricate ultrathin films, to produce structures on a nm scale and by this to be able to modify and possibly tailor the magnetic, electronic and chemical properties of a surface. Changes in the lattice parameter, the reconstruction of the surface or alloy formation can induce these surface modifications [46]. Surface alloys have already been proven to be excellent candidates to develop modified surfaces with an electronic structure, element concentrations and a geometric arrangement of the surface optimized for heterogenous catalysis [20]. Recent experiments also reveal a strongly enhanced magnetic moment for the Fe/Pt surface alloy compared to the Fe overlayer [21].

In this work the formation of a surface alloy with peculiar electronic properties is reported for Pb on Ag(111). A prerequisite to study the electronic surface structure is the complete characterization of the surface structures that appear upon Pb deposition. Island formation, step faceting, alloying and segregation are some examples for various phenomena that occur when a metal is deposited on a single crystal face of another metal [47, 48]. Therefore the growth of Pb on Ag(111) is characterized as function of Pb coverage and the subsequent annealing temperature in this chapter. It is found in particular that the Pb atoms are alloying with the atoms of the first Ag layer and form a well ordered $(\sqrt{3}\times\sqrt{3})$R30° alloy structure, even though Pb and Ag are completely immiscible in the bulk. This two-dimensional intermixing in the first substrate layer is known as surface alloying and has been observed for a variety of binary metal combinations [49, 50]. In Ch. 6 the detailed investigation of the electronic properties of the ordered $(\sqrt{3}\times\sqrt{3})$R30° Pb/Ag(111) surface alloy yields a new two-dimensional electronic state, which is confined to the surface alloy layer and exhibits a large band splitting due to spin-orbit interaction.

No detailed microscopic study regarding the growth of Pb on Ag(111) exists so far. Only a combined LEED, RHEED and AES study by Rawlings et al. [51] and a STM study which is focussed on higher coverages [52] give a rough overview over the growth behavior. In the LEED measurements the $(\sqrt{3}\times\sqrt{3})$R30° structure for coverages below a third of a ML is visible. The stability of the $(\sqrt{3}\times\sqrt{3})$R30° structure could not be explained because the LEED measurements can not prove a surface alloy formation. For higher coverages the $(\sqrt{3}\times\sqrt{3})$R30° LEED pattern fades and new spots appear. They are rotated by ±4.6° with respect to the Ag substrate, indicating a hexagonal Pb overlayer with a slightly larger lattice constant compared to Ag(111) that forms two possible rotational domains.

A related system that is thoroughly investigated is the Pb/Cu(111) surface alloy [53]. There a disordered alloy consisting of local $(\sqrt{3}\times\sqrt{3})$R30° and p(2×2) ordered patches is reported. The local order is restricted to a scale of only a few nm. From coverages above 0.22 monolayers (ML) on the Pb atoms segregate out of the Cu surface layer. This segregation is the logical consequence of the immiscibility of Pb and Cu in the bulk. It is also called de-alloying. The surface alloy phase coexists then with a pure Pb phase which shows a 4×4 reconstruction and a moiré pattern.

The detailed STM study of the growth of Pb on Ag(111) in the submonolayer regime performed in this work does not only reveal the structures that evolve in the growth process. The measurements also indicate that the alloying mechanism is analogous to the one observed for Sn on Cu(111) [54]. According to that two-dimensional pure Pb islands, some 100 nm in diameter, exchange Pb atoms with Ag surface atoms while moving over the surface, leaving an alloyed surface behind. Also the de-alloying mechanism is discussed. It is found that the pure Pb phase forms preferentially at steps and induces a two-dimensional step faceting.

The results will be presented as follows. The first part, Ch. 5.1, is attributed to the Pb deposition at room temperature without subsequent annealing. Two characteristic growth regimes are distinguished depending on the Pb coverage. While at low coverage the alloying process governs the growth, segregation sets in from about 0.15 ML on until the surface is completely de-alloyed. The consequences of annealing at 520 K are reviewed in chapter 5.2. The most striking annealing effect is the formation of a well ordered $(\sqrt{3}\times\sqrt{3})$R30° surface alloy with unique electronic properties (Ch. 6). Finally, chapter 5.3 is focussed on a more detailed description of the pure Pb phase, combined with results of evaporating Pb on an annealed surface alloy layer. The interplay of step faceting by the pure Pb phase and the formation of large alloy islands on terraces that exceed a width of 180 nm offers new ways to tailor geometrical nanostructures on a surface.

The experiments presented in the following chapters were performed with a home-built low temperature STM, operating at 6 K in the UHV with a base pressure of 1×10^{-10} mbar. The Ag(111) single crystal sample was prepared by standard sputtering and annealing cycles. After cleaning the sample, Pb was evaporated at room temperature (RT) with an electron beam evaporator at a pressure of about 1×10^{-9} mbar. Afterwards the sample was either annealed 2 min at 520 K or directly transferred into the STM. The definition of one monolayer refers to the Ag lattice.

Finally, a nomenclature for the observed structures is established here to avoid uncertainties during the discussion. Islands on top of the surface are assigned to be *alloy islands*, if they consist of the ordered surface alloy phase. They are called *pure Pb islands* if they contain only Pb atoms. One exception are the large islands that appear upon annealing. They are referred to as *droplet islands*. In analogy, ordered structures that are embedded in the surface are called either *alloy* or *pure Pb patches*.

5.1 Room Temperature Deposition

5.1.1 Surface Alloying by Exchange Processes with a Moving Pure Pb Island

Already at Pb coverages of some thousandth of a ML, deposited at RT, one observes small Pb clusters and single atoms embedded in the first Ag layer on terraces in Fig. 5.1a. A seam of 2 nm apparent width of Pb atoms decorating the step edges is visible in the inset. The atoms appear as small bright spots with a height of some pm or as depletions depending on the sample bias (see Ch. 6.2). It is evident that the atoms and clusters are spread over the terrace not homogenously. Regions with a higher Pb density appear to be interconnected. The dashed white line indicates a possible interconnection path and acts as a guide to the eye.

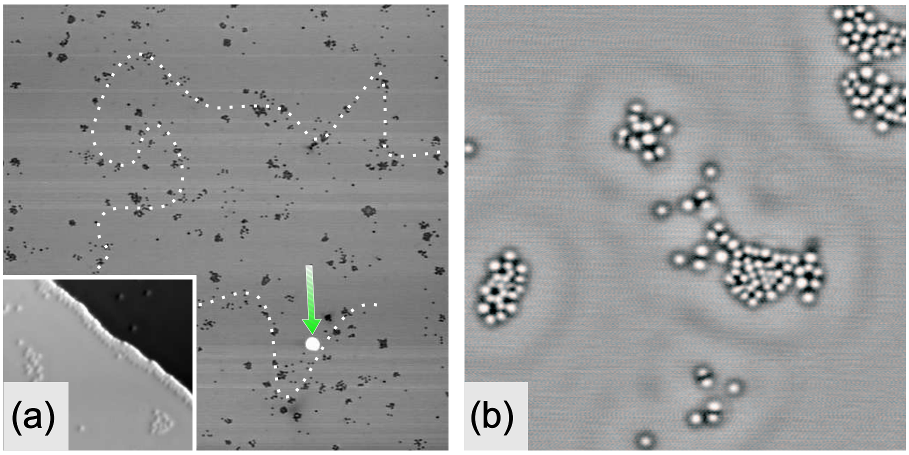

Figure 5.1: Surface morphology after deposition of 0.003 ML Pb on Ag(111). (a) $200{\times}200\,\mathrm{nm}^2$, 1 V: Large scale image of Pb atoms and clusters embedded in the Ag surface layer. They are left behind after exchange processes of moving pure Pb islands with the substrate. A possible track of such an island is indicated by the dashed line. A small surface alloy island on top is marked by the green arrow. Inset: $44{\times}37\,\mathrm{nm}^2$, -0.5 V: Steps are decorated by a seam of Pb atoms with 2 nm apparent width (b) $35{\times}35\,\mathrm{nm}^2$, 0.1 V: Zoom into a single cluster. The atoms that appear small in the center of the patch have arranged in a $(\sqrt{3} \times \sqrt{3}\,)\mathrm{R}30^\circ$ distance.

Fig. 5.1b reveals Friedel oscillations due to the scattered electrons of the Ag(111) surface state around the atoms and small clusters. They prove, that the surface around the atoms and small clusters is the clean Ag surface. A closer look to one of the embedded clusters in Fig. 5.1b reveals, that the Pb atoms turn out to appear in different apparent sizes. The atoms that are arranged closest have the smallest size. They exist mainly inside the clusters. These dense regions are local patches of atoms in the $(\sqrt{3}{\times}\sqrt{3})\mathrm{R}30^\circ$ distance, as can be derived from the comparison with the substrate orientation in an atomically resolved image. Mainly at the border of the cluster, one can find larger atoms. They are aligned in substrate direction and have a spacing of 1-2 Ag atoms. The smaller size of atoms inside the cluster is most probable an electronic effect. Due to the smaller next-neighbor distance of the Pb atoms in the $\sqrt{3}$ configuration, their wave functions gain a larger overlap and are thus less localized.

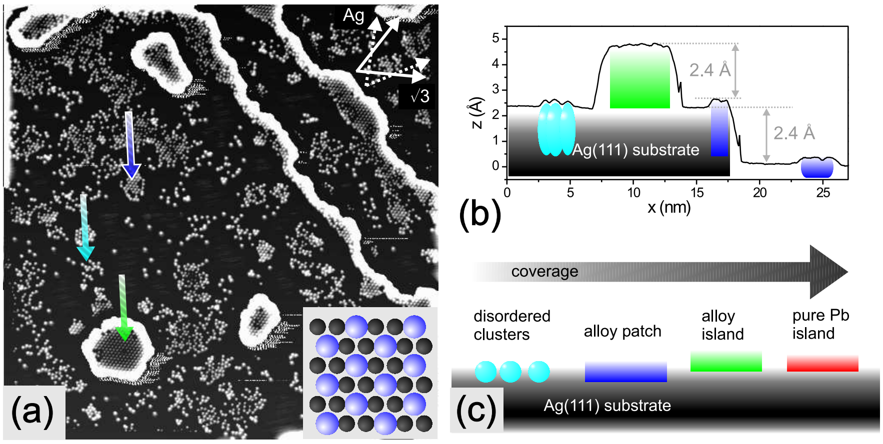

Figure 5.2: (a) 75×75 nm^2, 0.04 ML at RT preparation: Embedded clusters coexist with surface alloy islands with a size of 10 − 20 nm, the image is Fourier filtered to remove the step induced contrast. Inset: model of the $(\sqrt{3}\times\sqrt{3})R30^\circ$ alloy phase. Only the Pb atoms (blue) are atomically resolved in the STM images. (b) STM line scan across alloy patches, an alloy island and a Ag step. The apparent height of the structures proves the incorporation of the patches. The color code is related to the schematic drawing in (c). It gives an overview over the structures that appear depending on the coverage. The colored arrows link the scheme to (a),(b) and Fig. 5.1a.

The green arrow points towards an about 5 nm large island on top. The height difference between a cluster and the island is exactly the Ag(111) step height. At increased coverage more islands of this kind exist. Fig. 5.2a shows a Ag(111) surface covered with some percent of a ML Pb after room temperature deposition. Five small islands on top, 5-10 nm in size, are visible. They have the same apparent height as the island in Fig. 5.1a and show an atomically resolved corrugation with a next neighbor distance of 5 Å which is $\sqrt{3}$ times the Ag lattice constant (2.89 Å). Thus the island consists of a well ordered $(\sqrt{3}\times\sqrt{3})R30^\circ$ Pb/Ag surface alloy structure where only the Pb atoms of the alloy are visible, while the six Ag atoms, surrounding each Pb atom are not resolved atomically. In this alloy structure the Pb atoms substitute every third Ag atom of the Ag layer as illustrated in the inset of Fig. 5.2a. These islands will be called *alloy islands* as declared above.

In Fig. 5.2a at 0.04 ML the single Pb atoms and small clusters in the

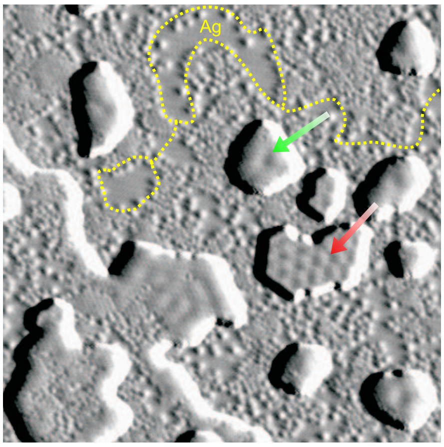

Figure 5.3: 50×22 nm^2, 0.14 ML: The density of clusters on the terraces has increased. Besides the surface alloy islands a few islands consisting of pure Pb appear, showing a moiré pattern (red arrow).

first Ag layer have increased in number. In addition patches of the ordered $(\sqrt{3}\times\sqrt{3})$R30° alloy structure, called alloy patches, that are embedded in the Ag surface and decorate the steps have developed. The steps are no longer straight but appear rough due to the decoration. Increasing the coverage to 0.14 ML Pb as shown in Fig. 5.3 the density of the embedded clusters and alloy patches has further increased. Only a few spots of the bare Ag surface are still visible. Beside the surface alloy islands that cover about ten percent of the surface, islands consisting of pure Pb cover an area fraction in the order of one percent. They can be recognized by their about 35 pm lower apparent height compared to an alloy island and by a periodic surface modulation (red arrow in Fig. 5.3) which is a moiré pattern as will be discussed in detail in Ch. 5.3.

The schematic drawing in Fig. 5.2c summarizes the evolving structures observed so far. The colored arrows in Fig. 5.1a, Fig. 5.2a and Fig. 5.3 relate the schematic view to the STM images. The drawing relates also schematically the apparent heights for negative bias voltages. A measured line scan across embedded Pb atoms, an alloy island, alloy patches and a Ag step is plotted in Fig. 5.2b. The height difference between alloy patch and alloy island equals exactly the height of a Ag step. This is a strong indication that the Pb atoms, clusters and alloy patches are really incorporated in the Ag surface layer and that the islands grow on the bare Ag substrate. The fact that Pb atoms form a seam decorating the step edges points also towards an incorporation of the Pb atoms in the first substrate layer at the steps. It is plausible to assume that the Pb atoms stick out of the surface due to their larger size compared to Ag atoms. This rumpling has already been observed for Sb on Ag(111) and Cu(111) [55].

Discussion

There is strong evidence to explain the observed RT growth behavior in analogy to the alloying mechanisms found for Sn on Cu(111) at very low coverages [54]. Schmid *et al.* discovered that upon Sn evaporation at room temperature large Sn islands form on the Cu surface. These islands diffuse across the surface and exchange Sn atoms within the islands randomly with Cu atoms in the surface. These exchange processes result in a trace of single embedded Sn atoms and clusters incorporated in the Cu(111) surface layer. In addition, small immobile $(\sqrt{3} \times \sqrt{3})\mathrm{R}30^\circ$ Sn/Cu alloy islands are left behind, containing the Cu atoms that have left the surface layer caused by the exchange. The driving force for the island movement is the strong repulsion between embedded Sn atoms and the pure Sn islands. Thus the surface free energy is lowered by an island motion towards unalloyed regions. This mutual repulsion influences the islands trajectory such that a travelling island avoids the track of itself or of other islands. After a few minutes the Sn islands are completely dissolved and cannot be observed anymore.

In the following the similarities between the growth of Pb on Ag(111) and of Sn on Cu(111) are pointed out and the evolution of this growth mechanism is discussed also for higher coverages. The key conditions that make growth in these two systems comparable are fulfilled: The vacancy formation energy of Ag(111) and Cu(111) is of the order of 0.6-0.9 eV [56], while the activation energy for self-diffusion on the surface is much lower in the range of 100 meV [57, 58]. The embedded clusters and single atoms at very low coverages presented in Fig. 5.1 look similar to the ones in the study of Sn on Cu(111). Also their inhomogeneous distribution implies this alloying mechanism. The dashed white line in Fig. 5.1a mark possible tracks of a pure Pb island that leaves an alloyed surface stream behind.

The small alloy island in the lower right corner of Fig. 5.1a is a further indication for the suggested exchange mechanism. As mentioned before, an alloy island nucleates inside the moving island due to exchange processes and is then left behind like the embedded patches. A logical consequence within this picture is the increasing number of alloy islands at higher coverages which is then directly correlated with the increasing cluster density in the surface.

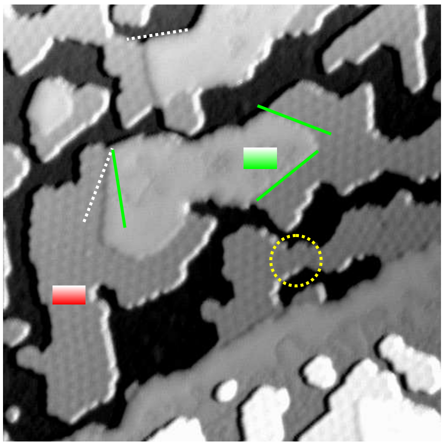

Figure 5.4: 55×55 nm^2, 0.35 ML: The pure Pb islands have grown and connect the alloy islands, which still have the same size distribution as at lower coverages. Dashed white and solid green lines show Ag(111) and surface alloy orientation, respectively. The dashed yellow circle marks a boundary between two domains of the moiré pattern.

The more Pb is deposited the more difficult it becomes for the pure Pb islands to move along bare Ag regions. The regions in the surface that are already contaminated with Pb repel the pure Pb island. In case that the pure Pb island is stopped by the surrounding alloy without enough pure Ag around it to find a way out or to form the alloy phase, the pure Pb island remains on top of the surface. Such an island is always surrounded by the alloyed surface. This is indeed what is observed in Fig. 5.3 at a higher coverage of about 0.14 ML. Consequently, the immiscibility of Pb and Ag in the bulk induces a new growth mode from this coverage on. The growth changes from alloying to de-alloying.

5.1.2 De-Alloying and the Formation of a Pure Pb Overlayer

The results of the changed growth mode are visible at higher coverage in Fig. 5.4. The amount of pure Pb on the surface has significantly increased at the coverage of 0.35 ML. While at 0.14 ML only occasionally some isolated pure Pb islands appeared, they have interconnected at 0.35 ML forming a meandering network and surrounding the surface alloy islands. A closer look to the network reveals that the moiré pattern can have different orientations. Furthermore junctions of two necks can be found where domains of different orientations merge. One example is marked by a dashed yellow circle in Fig. 5.4.

The alloy islands have not changed their size significantly but their den-

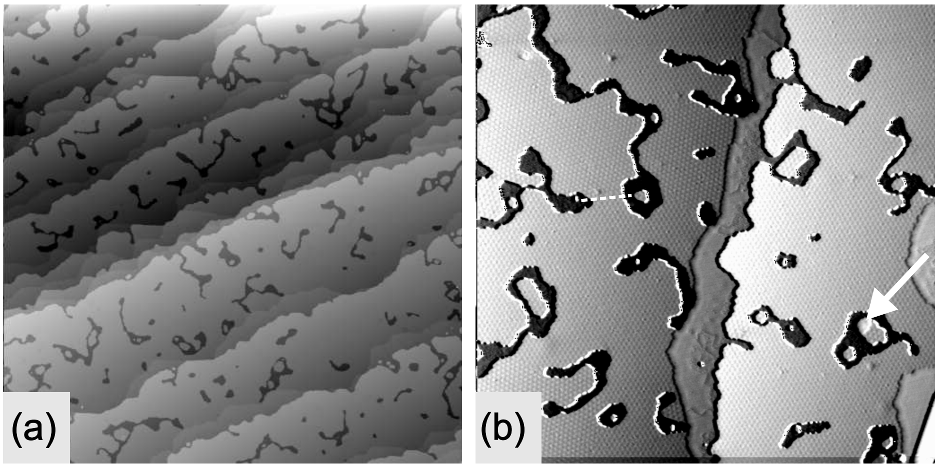

Figure 5.5: (a) $300{\times}300\,\mathrm{nm}^2$, 0.8 ML: The pure Pb islands have further connected and form an almost complete overlayer. The alloy islands have disappeared. (b) $144{\times}144\,\mathrm{nm}^2$: Two different orientations of the moiré pattern still exist. The black "worm-like" regions consist of the disordered surface alloy. The white arrow marks a non dissolved alloy island attached to a pure Pb island and the dotted line a domain boundary in the pure Pb island.

sity has decreased. Compared to Fig. 5.2 the alloy islands shape appears to be more triangular. The edges follow either the substrate or surface alloy orientation, or their orientation is rotated with respect to substrate and alloy in a defined angle, such that the edges follow the maxima of the moiré pattern. This faceting of step edges is a universal phenomenon and will be discussed in more detail in Ch. 5.3. For comparison the Ag(111) and the $(\sqrt{3}\,\mathrm{x}\,\sqrt{3}\,)\mathrm{R}30^\circ$ alloy directions are indicated at selected edges of two alloy islands in Fig. 5.2a by a dashed white line and a solid green one, respectively. The periphery around the islands is found to be still formed by a disordered alloy. Only at steps also the ordered phase exists.

At even higher coverages (Fig. 5.5) the alloy islands are almost completely dissolved and the pure Pb network is predominant and has become more dense. The black "worm-like" areas in Fig. 5.5a and b are still formed by the residual disordered alloy phase. Also at this high coverage the pure Pb phase does not reach the step edges which appear to be still rough and consist of the surface alloy. The white arrow in Fig. 5.5b points towards the rare event of a remaining surface alloy island attached to a pure Pb island.

Discussion

At coverages at which the pure Pb islands remain on the surface because they are stopped by the surrounding alloy, a few spots of the pure Ag surface are still visible (see for example the areas marked by yellow dashed lines in Fig. 5.2b). They appear to be interconnected by less dense regions in the disordered alloy. Only in these regions pure Pb islands can exist without experiencing the repulsive potential of the embedded Pb atoms. With increasing coverage more and more incorporated Pb atoms have to segregate out of the surface and join the pure Pb islands to avoid any unfavorable higher coordination.

The de-alloying process is assumed to happen preferentially at the step edges of the alloy islands because they contain Ag atoms that in turn fill the vacancies that emerge from segregation. The scheme in Fig. 5.6 illustrates the de-alloying mechanism. Pb atoms without an appropriate adsorption site reach an alloy island step edge. The island is already surrounded by embedded Pb atoms. Thus, the additional Pb induces the exchange process of incorporated Pb atoms with Ag atoms of the alloy island (Fig. 5.6 (1) and (2)). The released Pb atoms of the alloy join the other Pb atoms and form a pure Pb island on top of the bare Ag substrate. In consequence the pure islands form at the expense of the alloy islands which are finally dissolved. This growth scenario is confirmed by the observed decrease of the surface alloy island density with increasing coverage. The observation that the pure Pb

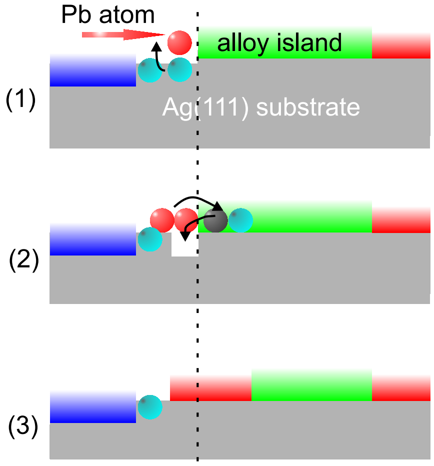

Figure 5.6: Illustration of the three process steps during de-alloying at an alloy island step edge. (1) Additional Pb atoms on top induce the segregation of embedded Pb atoms. (2) The resulting vacancies are filled by Ag atoms of the alloy island. (3) The Pb atoms form a pure Pb island on top of the bare Ag substrate. By this process the alloy island shrinks.

islands moiré orientation remains unchanged supports furthermore the idea that the Pb islands expand and connect to a meandering network. The initial difference in moiré orientations leads then to different domain orientations meeting at some network junctions.

The "worm-like" residues of the disordered alloy that are completely surrounded by the pure Pb network can be explained as follows. If the alloy islands are already dissolved and no more Ag is available to replace Pb atoms in the disordered alloy the de-alloying process is expected to be inhibited. A source of free Ag atoms that could replace the Pb atoms in the "worm-like" areas is missing there and therefore the disordered alloy remains.

For the pure Pb phase LEED experiments by Rawlings *et al.* [51], the results of which have been reproduced within this work, show that the pure Pb phase grows only on pure Ag. In studies concerning the surfactant properties of Pb during growth of Cu or Co on Cu(111) [59, 60] the continuous segregation of Pb towards the surface is observed as well. The observed surface alloying despite the immiscibility of Ag and Pb in the bulk indicates that the higher coordination of a Pb atom in bulk Ag is the driving force that leads to segregation. At the surface this coordination is reduced from 12 to 9 nearest neighbors. Thus the Pb atom that is too large to fit in a Ag bulk vacancy has apparently enough space on the substitutional surface site. It is found also theoretically that the atomic size mismatch leads to segregation from the bulk to the surface [16, 17, 61]. The apparent height difference between alloy patch and alloy island which is exactly the height of a monatomic Ag step indicates also that the area below the alloy islands consists only of Ag atoms as well. It will be further confirmed in Ch. 6.1 by using the electronic properties of the alloy phase.

To briefly summarize, the growth of Pb on Ag(111) upon room temperature deposition is dominated by surface alloying up to about 15 % of a monolayer. Migrating pure Pb islands drive the alloying process. They exchange Pb atoms with Ag surface atoms while moving across the surface and leave a trace, consisting of embedded Pb atoms and clusters together with immobile alloy islands on top, behind. The driving force for the pure Pb island motion is the strong repulsion between the pure Pb island and the incorporated Pb. From a sufficiently high coverage on, the pure Pb island motion is stopped by the large amount of embedded Pb atoms. Pb segregation and de-alloying sets in and governs the growth. The final result is a pure Pb overlayer on top of a bare Ag(111) substrate.

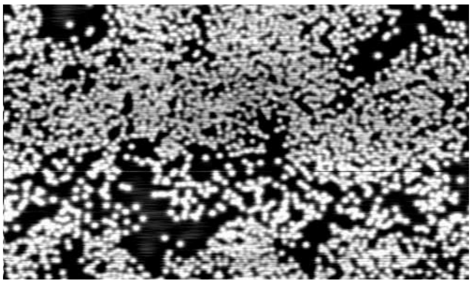

Figure 5.7: 70×40 nm^2, 0.14 ML. Annealing the Pb/Ag system of Fig.5.2a at 410 K for 2 min leads to the incorporation of Pb atoms. The atom density in the surface layer is inhomogeneous.

5.2 Annealing Effects

Annealing allows the system to relax into a thermodynamically more stable configuration. For thermally activated processes the annealing temperature plays a crucial role.

5.2.1 Disorder-Order Transition in the Surface Alloy

Fig. 5.7 shows the surface after annealing 0.04 ML Pb at 410 K for 2 minutes (see Fig. 5.2a for room temperature deposition of 0.04 ML). All islands have vanished and the Pb atoms are incorporated in the first surface layer. One can clearly distinguish between regions with a high density of Pb atoms and some almost Pb free areas. The interatomic distances of the Pb atoms are dominated by the $\sqrt{3}$ and the 2×2 distance in the dense spots. The average Pb-Pb distance increases towards the Pb free regions, even some separate Pb atoms appear.

Increasing the annealing temperature from 410 K to 520 K results in a more homogenous Pb distribution. Fig. 5.8a has been recorded after annealing 0.14 ML Pb at 520 K. The Pb density is no longer inhomogeneous like in Fig. 5.7 and the embedded Pb atoms are distributed equally over the whole surface. In general, annealing of Pb on Ag(111) at 520 K causes the formation of a disordered surface alloy from the very low coverage regime on up to 1/3 ML. It is illustrated in the series from Fig. 5.8 to Fig. 5.9 with an intermediate coverage of 0.25 ML in Fig. 5.8b. While in Fig. 5.8a the single Pb atoms of the disordered alloy can still be resolved, they form a blurred network in Fig. 5.8b. They can only be partially resolved by imaging a smaller area (see inset in Fig. 5.8b) which reveals still the disordered alloy phase. The apparent atom height is no longer the same everywhere, but some bright spots appear, indicating a varying surface electron density.

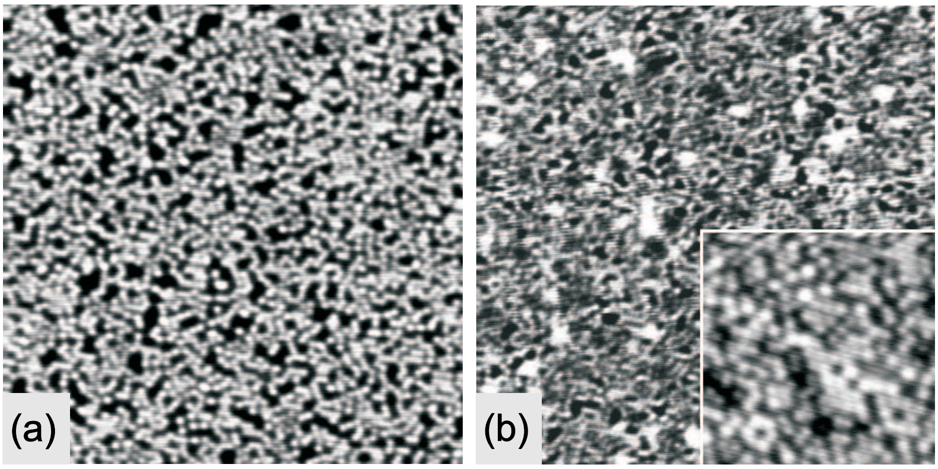

Figure 5.8: (a) 40×40 nm^2, 0.14 ML. After annealing at 520 K all alloy islands have vanished and the Pb atoms are equally distributed over the whole surface. (b) 43×43 nm^2, 0.25 ML. The Pb atoms form still a disordered surface alloy in the Ag surface layer but they appear blurred and can not be distinguished anymore on that length scale. Inset: 10×10 nm^2. A zoom into the structure resolves the Pb atoms again.

A significant change in the surface morphology appears after deposition of about 0.3 ML Pb and subsequent annealing at 520 K. The Pb atoms arrange in a $(\sqrt{3} \times \sqrt{3})$R30° surface alloy structure that is well ordered in a range of 100 nm and covers the whole surface. In Fig. 5.9a this long-range ordered surface alloy is apparent. Analogous to the alloy islands and patches in Fig. 5.2a, only the Pb atoms can be seen, the six Ag atoms surrounding each Pb atom are not resolved. They are schematically drawn in Fig. 5.9b as white circles while the imaged Pb atoms are surrounded by black circles. Also the new unit cell of the $(\sqrt{3}\,\mathrm{x}\,\sqrt{3})$R30° surface alloy is marked. Although this surface alloy phase is well ordered over a long-range, still a high concentration of black spots and lines is visible. They will be discussed in Ch. 5.2.2.

The effect of annealing more than 1/3 ML Pb is a separation of the alloy phase and the pure Pb phase. In Fig. 5.10 the steps are covered by a broad seam of pure Pb. The width of the seam depends on the Pb coverage. Finally, at a full ML the whole surface is covered by a complete layer consisting of pure Pb. The steps are no longer rough and one observes a straight boundary also to the ordered surface alloy phase.

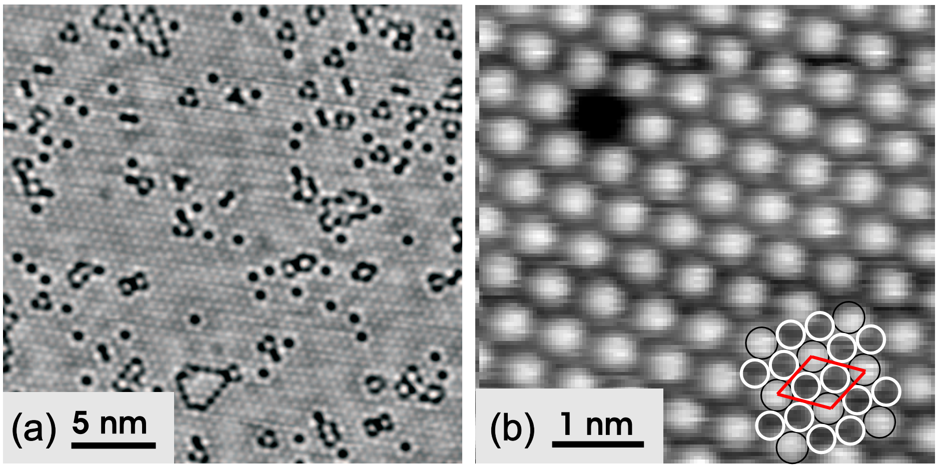

Figure 5.9: 0.32 ML of Pb after annealing at 520 K: (a) 26×26 nm^2, a long-range ordered $(\sqrt{3}\times\sqrt{3})$R30° surface alloy has formed. The image is Fourier-filtered in order to reduce the contribution of the standing waves that is due to the new electronic state that evolves in the ordered surface alloy (see Ch. 6.1.2). (b) Only the Pb atoms of the surface alloy can be seen, the Ag atoms, surrounding each Pb atom are not resolved atomically, but drawn as bright circles together with the surface alloy unit cell in the model.

Discussion

Annealing causes the incorporation of Pb in the Ag surface layer because at elevated temperatures the probability for vacancy formation in the Ag surface is enhanced. The preferred formation of a disordered alloy can be explained by the entropic contribution to the free energy. For 0.1 ML Sb on Ag(111) this entropic contribution has been calculated to be sufficient to cause disordering with respect to the $(\sqrt{3}\times\sqrt{3})$R30° arrangement. Only small energies are necessary in this case because due the effective in plane screening provided by the surrounding substrate atoms the Sb atoms interact only weakly with each other [61].

Theoretical examinations in the hard hexagon model which describes a triangular lattice gas with nearest-neighbor exclusion lead also to the conclusion that disorder is favored. This model furthermore predicts a disorder-order transition at a coverage of 0.28 ML [62, 63]. This is, within the error of coverage determination, in good agreement with the order transition observed in Figs. 5.8 and 5.9. The observation of a long-range ordered surface

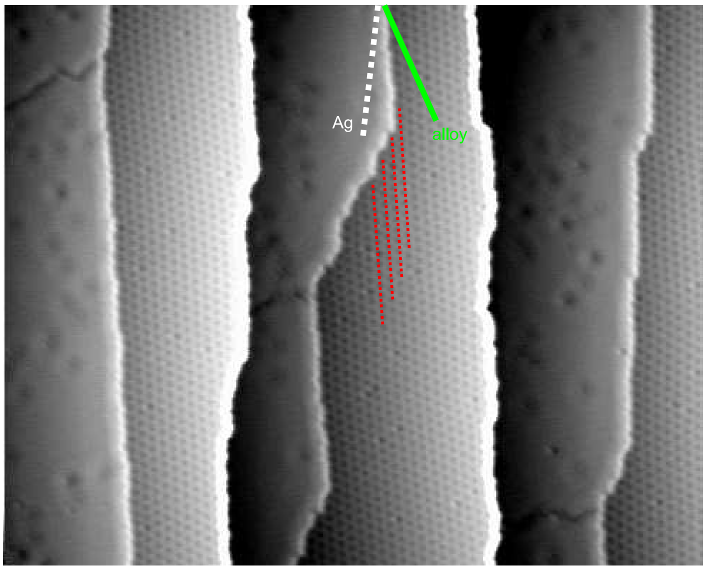

Figure 5.10: Upon annealing at 520 K the pure Pb phase forms at steps with a straight border to the surface alloy. The dashed white line and the solid green line indicate the substrate and surface alloy symmetry, respectively. The dashed red lines show the orientation of the moiré pattern and indicate the Pb induced two-dimensional facetting discussed in Ch. 5.3.1.

alloy is a striking difference to the growth of Pb on a Cu(111) surface, where only a disordered surface alloy is observed. The 13% larger lattice constant of Ag compared to Cu is the main difference of these two systems. Thus it appears that the shorter $\sqrt{3}$ distances between the Pb atoms in Cu(111) lead to a mutual repulsion of the large Pb atoms.

The apparently high activation energy for Pb diffusion which is reflected in the slow diffusion even at 410 K (see Fig. 5.7) proves again that the Pb atoms are incorporated in the surface layer. The diffusivity of atoms adsorbed on top of a fcc(111) surface would be orders of magnitude higher and the adatoms would reach a thermodynamical more stable configuration faster and already at significantly lower temperatures [57]. In fact, the diffusion behavior described here is quite similar to the diffusion of Pb in Cu(111) which also forms the disordered alloy phase.

It has been found recently that in that system diffusion is dominated by two rather slow processes, vacancy-mediated diffusion and adatom exchange. The contribution of fast mass transport processes to the diffusion process, i. e. step-edge running and adatom evaporation and condensation at steps, is negligible [64]. In the vacancy-mediated process [65, 66] embedded Pb atoms exchange with surface vacancies. In the STM investigation of Anderson *et al.* monitoring the Pb diffusion away from monatomic Cu(111) steps it was found that beside the slow diffusing Pb atoms single Pb atoms suddenly disappeared from the STM image. This observation is ascribed to the adatom exchange diffusion which is based on exchanging embedded Cu with thermal Pb adatoms that can diffuse rapidly and vice versa. At lower annealing temperatures like 400 K the vacancy-mediated diffusion process governs the diffusion kinetics. With higher temperatures more thermally generated exchange processes take place and accelerate the diffusion kinetics.

The alloy formation by deposition at room temperature proposed in Ch. 5.1.1 originates from Pb-Ag exchange processes in the pure Pb islands that move across the Pb free Ag surface. These pure Pb islands slowly dissolve by leaving behind embedded alloy patches and alloy islands on top of the surface (Fig. 5.2). At higher coverages this pure Pb island is expected to be stopped by the surrounding disordered surface alloy due to its higher roughness. One can expect that upon annealing at elevated temperatures the island diffusion sets in again. By this, the exchange processes can continue until the $(\sqrt{3} \times \sqrt{3})\mathrm{R}30^\circ$ surface alloy structure is complete. At these higher temperatures the removed Ag atoms diffuse to the steps where they are incorporated. When the saturation coverage, i. e. 0.33 ML, is exceeded, de-alloying sets in at step edges. As explained in Ch. 5.1.2 and illustrated in Fig. 5.6 the steps act as a source for Ag atoms that exchange with Pb atoms in the lower terrace. By this the alloy at the upper edge is converted into pure Pb which resides on the bare Ag substrate leading to a seam of pure Pb decorating the step edge.

5.2.2 Defects and Domain Walls in the Pb/Ag Surface Alloy

As briefly mentioned before, defects that appear as dark spots are distributed over the whole ordered surface alloy (Fig. 5.9 and 5.11). Their amount is of the order of one percent of the surface alloy area. In Fig. 5.9b a single defect is resolved. The apparent depth of these defects depends on the sample bias

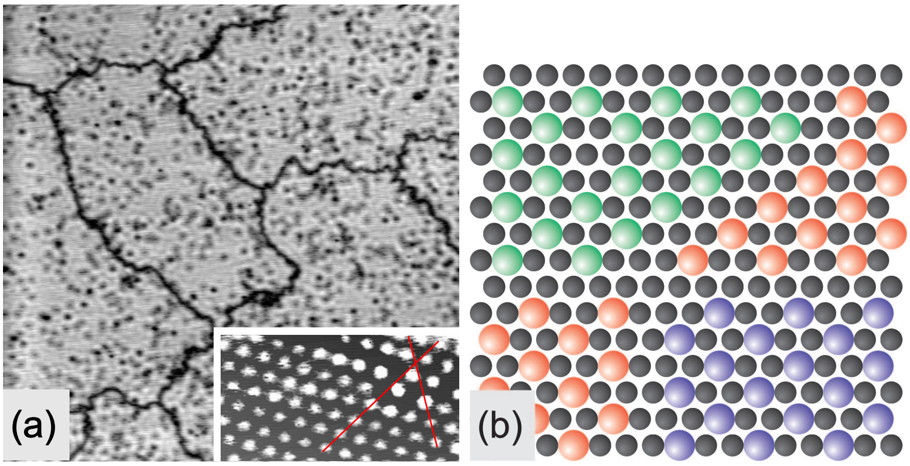

Figure 5.11: (a) 135×135 nm^2, 0.28 V, 1 nA. Domain wall network on a large terrace, separating the three commensurate domains with different $\sqrt{3} \times \sqrt{3}$)R30° surface alloy occupation sites. The Pb atoms around the domain wall are atomically resolved in the inset. (b) Domain wall model for a light wall system. The dark gray circles represent the Ag atoms, whereas the colored atoms are the Pb atoms of the different commensurate surface alloy domains. In the upper left domain a Ag atom that has not been substituted is visible. This is the model for the point defects.

and is in the order of 10 pm and the position of the neighboring Pb atoms is not influenced. Taking into account the similarity of these defects and the fact that the alloy forms by substitution of Ag atoms, there is strong evidence that the spots can be attributed to Ag atoms, that are not substituted by a Pb atom. Further results concerning the influence of the defects on the electronic properties of the surface alloy provide further indication for this interpretation (see Ch. 6.2.3).

The histogram in Fig. 5.12 shows the distribution of the nearest neighbor distances for the defects. It was obtained from 14 different and statistically independent STM images. The expected random distribution which is corrected for geometric effects [67, 68] is plotted as a red line for comparison. The peaks in the histogram are due to the discrete distribution of possible defect sites, but the general shape of the histogram is closely related to a random defect distribution. In Fig. 5.12 the trend appears that distances larger

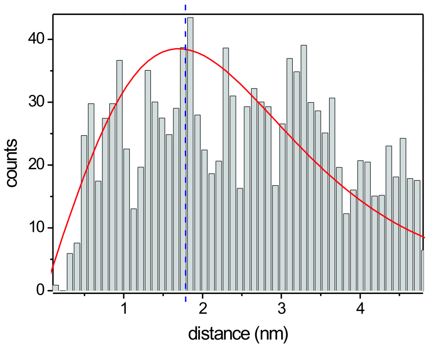

Figure 5.12: Histogram of the nearest neighbor distances of surface alloy defects in comparison with a random defect distribution (red line). The dashed blue line indicates the fermi wavelength λ_F of the new surface alloy state (see Ch. 6.1.2).

than 3 nm exist more often than expected from a random defect distribution. To verify this, further experiments have to be performed in order to get improved statistics. The dashed blue line marks the value of half the fermi wavelength λ_F of the new electronic state that arises upon the formation of the ordered surface alloy as will be discussed in detail in Ch. 6.1.2.

Besides the point defects also one-dimensional defect structures are observed. One finds that these lines are domain walls separating three commensurate surface alloy domains as illustrated in the simple model in Fig. 5.11b. The Pb density in the domain wall region is smaller than in the domains, thus the domain wall network can be classified as a so called light-wall system [69, 70]. Some small triangular domains consisting of only a few Pb atoms are apparent in Fig. 5.9a. On large terraces a domain-wall network has developed, which is shown in Fig. 5.11. The average domain size is in the order of some hundred nanometers. In the inset, the Pb atoms of two neighbored surface alloy domains are resolved atomically.

5.3 Structural Properties of the Pure Pb Overlayer

Having studied the structure of the ordered surface alloy in detail, the pure Pb overlayer will be investigated in this section. Already at a coverage of 0.14 ML one observes small islands with a periodic pattern (see Fig. 5.2b). A number of arguments, for example the LEED results or the increasing area fraction with increasing coverage, led to the conclusion that this structure consists of pure Pb. These observations have been described in detail in Ch. 5.1.1, 5.1.2 and 5.2. In this section the origin of the observed moiré pattern will be explained. It is due to a slight rotation of the Pb overlayer compared to the Ag substrate. Furthermore, it is demonstrated that the overlayer is only weakly bound to the substrate. Even though the substrate-overlayer coupling is weak the study of the electronic properties of the pure Pb in Ch. 6.3.1 shows the consequences of the interaction. The first Ag layer below the Pb overlayer is found to reconstruct in order to avoid the energetically unfavored Pb sites on top of Ag atoms. The same reconstruction has been reported for a monolayer Pb on Cu(111) [71]. The observed substrate reconstruction in turn is believed to be responsible for a Pb induced two-dimensional faceting of steps and pure Pb islands which will be discussed in Ch. 5.3.1.

Fig. 5.13a shows the atomically resolved pure Pb overlayer. The atomic corrugation is superimposed by a modulation with a periodicity of 16.5 Å. The maxima of this pattern are rotated by 25° with respect to the direction of the atomically resolved atoms. The nearest neighbor distance of the Pb atoms is 3.5 Å which is a factor of 1.2 larger than the nearest neighbor distance of the substrate Ag atoms.

This distance is in agreement with the LEED studies by Rawlings *et al.* [51]. The schematic drawing in Fig. 5.13b leads to the conclusion that the observed modulation is a moiré pattern. This pattern results from a rotation of the overlayer with respect to the substrate lattice. With knowledge of the lattice constants of substrate d_{Ag} and overlayer d_{Pb} together with the angle β between the overlayer atoms and the superstructure maxima the rotational angle α between substrate and overlayer can be calculated [72, 73] by

$$\alpha = [(d_{Pb} - d_{Ag})/d_{Pb}]\beta. \tag{5.1}$$

It gives $\alpha = 4.5°$. In Fig. 5.13b the atoms of the Ag surface layer and the Pb overlayer are plotted as black and red spheres, respectively. A rotation of the Pb overlayer by 4.5° with respect to the substrate leads to a very good agreement with the STM observation in Fig. 5.13a. Therefore one can conclude that the overlayer is rotated by $\pm 4.5°$ with respect to the substrate which results in two different domains that can be observed by STM and LEED.

The observed rotation of an adlayer has already been theoretically predicted by Novaco and McTague in 1977 [72]. They have shown that the energy of a monolayer is dependent on its orientation relative to the substrate. In particular, the orientation which minimizes the strain energy is

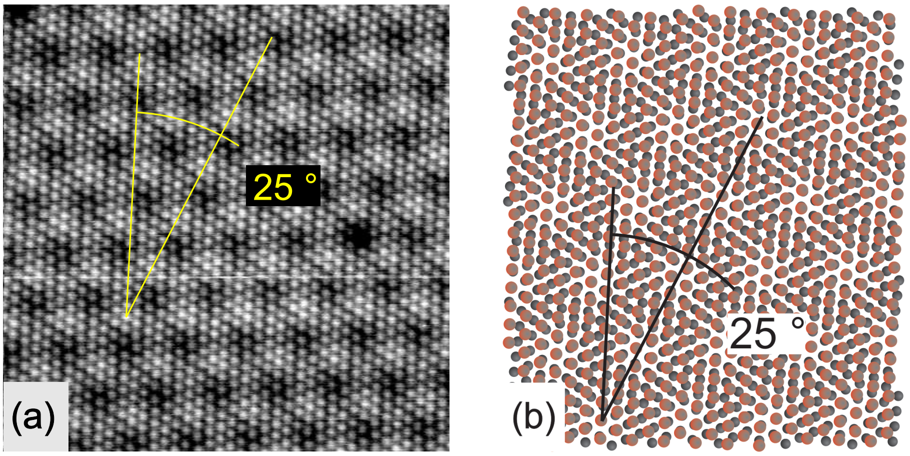

Figure 5.13: (a) 13×13 nm^2: STM image of the pure Pb overlayer. The atomic corrugation is superimposed by a moiré pattern. The nearest neighbor distance between Pb atoms is 3.5 Å. The moiré pattern is rotated by 25° with respect to the Pb atom orientation. (b) A schematic drawing with the respective lattice parameters reproduces that pattern. According to simple geometric considerations [73] the Pb layer is rotated by 4.5° with respect to the Ag substrate.

expected to deviate from the main symmetry directions of the substrate. The occurrence of a moiré pattern and the rotation of the overlayer with respect to the substrate are furthermore indications that the overlayer is only loosely bound to the substrate and that the intra-layer interactions between the Pb atoms are much stronger than the interaction with the Ag substrate.

Experimental evidence for this weak substrate-overlayer interaction is given by an annealing experiment where about 0.4 ML Pb are annealed up to 700 K. After this flash annealing only the surface alloy remains, covering the whole surface, while the pure Pb layer has been desorbed. This way of removing the pure Pb overlayer offers the possibility to easily fabricate the well ordered surface alloy structure. That is very helpful especially for experimental setups that do not allow for the fine adjustment of preparation parameters like sample temperature, Pb flux et cetera. Using this recipe enables one to investigate the well defined surface alloy without prior careful structural characterization of the surface. This is advantageous also for the photoemission experiments presented in Ch. 6.1.3.

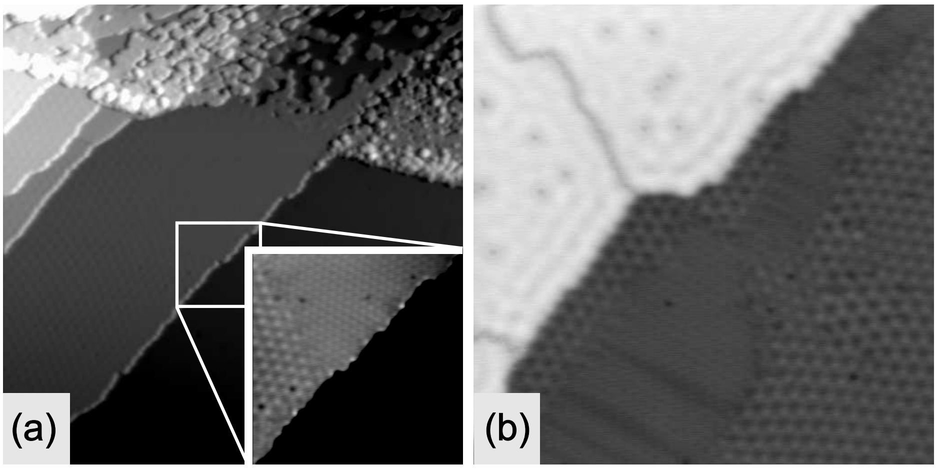

Figure 5.14: (a) 84×84 nm^2: STM image of an area, where the pure Pb overlayer has been destroyed accidentally by the STM tip (upper part). The influence on the environment is shown in the inset. The moiré pattern changes amplitude, periodicity and orientation. (b) 48×48 nm^2: 60 nm away from the destroyed area the Pb overlayer is still strongly distorted.

The weak coupling to the substrate leads to a flexible overlayer as can be observed by STM. Already slight changes in the overlayer lattice constant and the rotational angle influence the observed angle between moiré maxima and Pb atoms. Any local expansion or compression of the Pb overlayer is visualized by a change in the direction of the moiré pattern. These elastic effects can already be seen at the meandering pure Pb islands of Fig. 5.4 and Fig. 5.5. Due to the bent borders and the interconnection with islands of different moiré orientation the Pb atoms have to relax under the constraint of the given conditions.

An intriguing example for the weak coupling of the Pb layer to the substrate is given in Fig. 5.14. In the upper part of Fig. 5.14a the smooth overlayer has been destroyed accidentally by the STM tip. A zoom into the destroyed area reveals that the bare Ag surface is uncovered because some Pb atoms immersed in the characteristic standing waves of the Ag surface state electrons are visible. On the large terrace in the center of the image the moiré pattern disappears. A magnification of the area of interest (see inset) reveals a domain boundary separating two moiré-type modulations. The domain close to the uncovered Ag region yields a different angle, orientation and smaller amplitude of the pattern. Thus, at the boundary the rotational angle and the lattice constant of the Pb overlayer have changed. About 60 nm away from the destruction of the overlayer the tip influence can still be observed. In Fig. 5.14b the pure Pb overlayer is strongly distorted along the border to the surface alloy which in turn has not been affected by the tip demonstrating its higher stability.

5.3.1 Pb Induced Two-Dimensional Faceting

In the following the interaction between the pure Pb phase and its boundaries is discussed more in detail. In that context a sample is studied, where additional Pb is evaporated on the annealed surface alloy layer at room temperature. After discussing the evolving pure Pb structures it will be shown that their facet shapes and facet directions are determined by the orientation and periodicity of the observed moiré pattern. These findings can be extended to all Pb structures described so far.

The additional evaporation leads to an increase in coverage from 0.30 ML to 0.36 ML. The annealed surface alloy before the evaporation of additional Pb is shown in Fig. 5.15c. After the evaporation it coexists with pure Pb regions (Fig. 5.15a) which show the moiré pattern with a usual periodicity between 16 and 17 Å. These regions are either attached to step edges, have formed elongated islands, up to 50 nm long with a width of about 10 nm, or they appear as patches embedded in the coexisting surface alloy.

The pure Pb patches and islands are locally related. In many cases, one border of an embedded patch touches one facet of an island or the patch is located very close to an island. The surface alloy in the vicinity of the closed packed regions shows furthermore much less deviations from the perfect order than in areas more far away from these regions. An example for this is depicted in Fig. 5.16. The pure Pb patch that is embedded in the alloy layer at a step edge is surrounded by a belt of perfectly ordered surface alloy without any vacancies. In the upper left of the image the defects appear again.

The local relation between embedded Pb patches and pure Pb islands on top supports the explanation for patch and island formation, which is similar to the one supposed by Nagl *et al.* for the same effect observed during growth of Pb on Cu(111) [53]. The mechanism differs from the pure Pb formation during annealing. The origin of this difference is believed to be due to the residual kinetic energy of the evaporated Pb atoms. An incoming Pb atom pushes Ag atoms of the surface alloy out of the surface layer. The surface

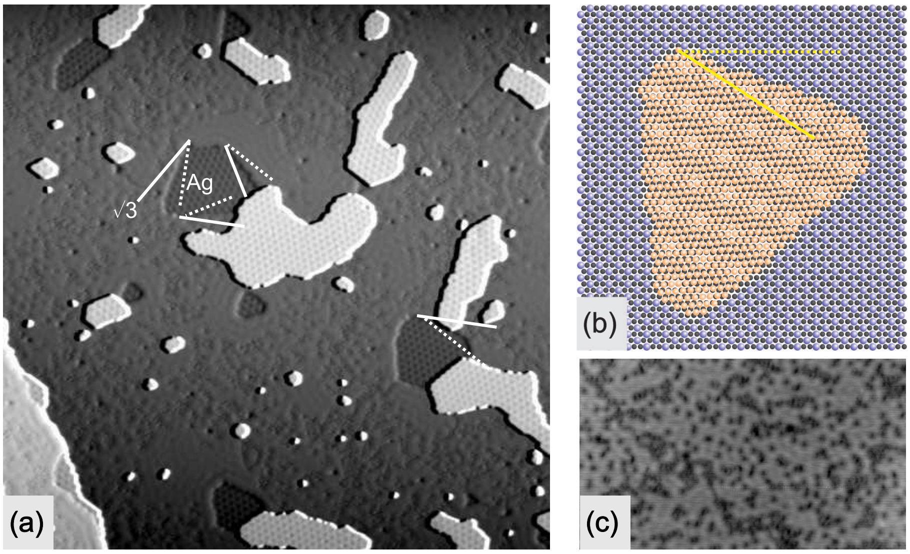

Figure 5.15: (a) After deposition of 0.06 ML additional Pb at RT on top of the annealed surface alloy layer, the surface alloy coexists with pure Pb islands (bight) and patches of pure Pb embedded in the alloy layer (dark). (b) Ball model of an embedded Pb patch. The edges are aligned with the maxima of the moiré pattern. 145×145 nm^2. (c) 75×37 nm^2. Annealed surface alloy at 0.30 ML

diffusion of these Ag atoms is limited at room temperature by the alloy. Due to the higher strain in the surface layer which is caused by the excess Pb atom, the Ag atoms exchange with Pb atoms of the surface alloy in the neighboring region. By this mechanism an embedded patch solely consisting of Pb atoms can form with a clean Ag region covered by a pure Pb island directly beside.

The fact, that the step height between an embedded patch and an pure Pb island equals that of a Ag step, supports this hypothesis. It is quite plausible that the defects in the surface alloy are Ag atoms, that have not been substituted by Pb atoms (see Ch. 5.2.2). Thus, the formation of the perfectly alloyed regions around the embedded patches can be explained by the incorporation of incoming Pb atoms, that did not fit into the pure Pb patches.

The embedded pure Pb patches in Fig. 5.15a show a well defined triangular or sometimes hexagonal shape. The edge direction deviates from

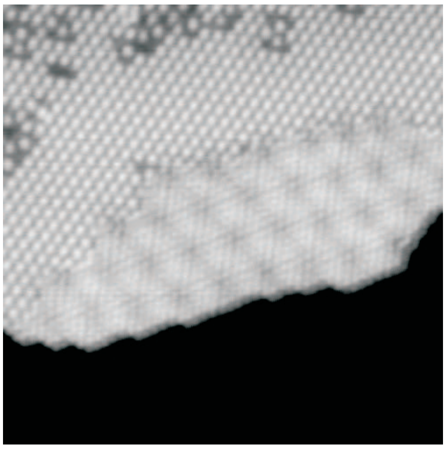

Figure 5.16: 18×18 nm^2. An embedded pure Pb patch at a step edge is surrounded by the surface alloy. In the direct vicinity of the patch the surface alloy is free of defects.

substrate (dashed lines) and surface alloy orientation (solid lines). Instead the edges are aligned along the maxima of the moireé pattern with its two possible orientations. The simple ball model in Fig. 5.15b depicts one possible atomic configuration for an embedded Pb patch. The blue spheres are the Pb atoms of the surrounding surface alloy and the smaller spheres in a dark gray resemble the Ag atoms of the surface alloy. The Pb atoms forming the patch are plotted as orange spheres in that scheme. They are assumed to have the same lattice constant, 3.5 Å, and the same rotational angle of 4.5° as the pure Pb layer on top of the surface. The edges are chosen such that they border the moiré maxima. The substrate and alloy orientation are plotted as yellow lines as a guide to the eye. The direct comparison of the model with the patch in the lower right in the STM image shows an excellent agreement between model and experiment. The length of the patch edges is neither arbitrary. In Fig. 5.17 the length of numerous patch edges L is plotted versus the ratio of L to the periodicity of the moiré pattern d. It is obvious that only integer multiples of half the moiré periodicity occur.

The shape of the elongated pure Pb islands on top is also influenced by the moiré superstructure. First and foremost it originates from the history of the sample preparation. In this peculiar case presented here the coverage before the evaporation of additional Pb was 0.30 ML which means that the surface alloy shown in Fig. 5.15c was not yet completely developed. There are regions with a lower Pb density compared to the ordered alloy. Pb atoms on top of the surface are known to be repelled by alloyed Pb atoms (Ch. 5.1.1). In consequence the additional Pb atoms are likely to form compact pure Pb islands

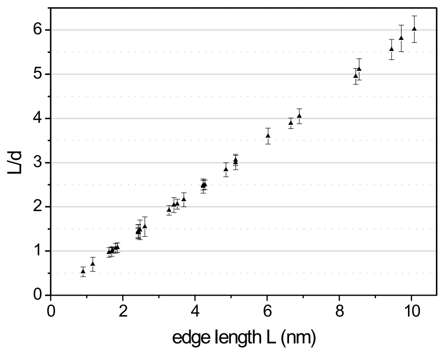

Figure 5.17: Ratio of the edge length L of several embedded Pb patches to the periodicity of the respective moiré pattern d versus edge length L. The length of patches is apparently always an integer multiple of half the periodicity of the moiré pattern.

in the Pb-poor regions, because less Pb atoms have to segregate compared to the ordered and Pb-rich $\sqrt{3}$-alloy. The regions of low Pb density form along domain walls and are consequently elongated in distinct directions. By this also the pure Pb islands on top get an elongated shape.

A closer look confirms that the moiré pattern appears always complete even at the borders of the pure Pb islands. The islands facets follow the shape of the moiré pattern. This observation can be extended to all Pb structures observed. It is evident that the island shapes are governed by the moiré pattern. Also the borders to the surface alloy that form upon annealing at 520 K and the step edges are found to reconstruct such that they follow the periodicity and the orientation of the moiré maxima. This is indicated by the dashed red lines in Fig. 5.10.

This two-dimensional faceting due to the Pb overlayer is hard to understand when the observed moiré pattern is believed to originate only from the rotation of the Pb overlayer with respect to the substrate. In that case an energy gain by the formation of straight steps in substrate or alloy direction is expected whereas no reason for a lowering in the total energy by completing the moiré pattern is evident. But the investigation of the electronic structure of pure Pb (Ch. 6.3) implies that the Pb overlayer induces a reconstruction of the Ag substrate. By the rearrangement of Ag atoms the energetically disfavored constellation of a Pb atom on top of a Ag atom is avoided. This results in a lowering of the total energy. Apparently, this energy gain is higher than the one for the formation of straight steps in substrate or alloy direction, i. e. the step directions are determined by the second layer rearrangement.

In contrast to the two-dimensional faceting reported so far for metal-on-metal and molecule-on-metal growth [74, 75, 76] which is directly adsorbate-induced it appears that the faceting in case of Pb on Ag(111) is generated indirectly by the overlayer induced reconstruction of the substrate.

Droplet Formation

In Ch. 5.2 it was described that upon annealing at 520 K the pure Pb and surface alloy islands dissolve and get completely incorporated in the surface layer up to a coverage of 1/3 ML. In this section one exception will be discussed. It is the formation of large droplet-like surface alloy islands during annealing on very wide terraces. At coverages above 0.33 ML seams of pure Pb are attached to the droplet islands and govern their shape.

This is shown for 0.35 ML Pb annealed at 520 K. The 380×380 nm^2 large STM image in Fig. 5.18a reveals an array of large scale droplet islands accompanied by two small droplet islands. In the inset an image of the non annealed sample with small alloy islands surrounded by the pure Pb network (see Ch. 5.1.2) is plotted for comparison. The droplet islands have a diameter of about 120 nm (35 nm for the small droplet islands). They are only observed on terraces with widths exceeding 180 nm and consist of the ordered surface alloy enclosed by pure Pb. The surface of the droplet islands has the same composition as the terrace surface.

The islands shape in this coverage regime is well defined but quite extraordinary. A triangular shape with flattened corners dominates the alloy part of the droplets. The pure Pb is attached preferentially to the long edges like Pb decorating the step edges on the surface (Fig. 5.10). One finds that at higher coverages also droplet islands evolve that only contain pure Pb. They have the same size as the large droplet islands in Fig. 5.18a.

In this context it is an important fact that the droplets only form upon post-annealing a sample that has been prepared at room temperature. They do not evolve during evaporation of Pb at an elevated substrate temperature of 520 K. That means, the mobility of the Ag atoms is reduced by the presence of the Pb atoms. The low mobility in turn hinders the reorganization of the surface, which sets in with the priority to form a homogenous surface alloy. In case of very large terraces the Ag atoms that have been removed from the surface layer are pinned then by an alloy island before they reach a step edge. Finally these Ag atoms form the droplet islands together with the Pb atoms that move across the surface as meandering and mobile pure Pb islands.

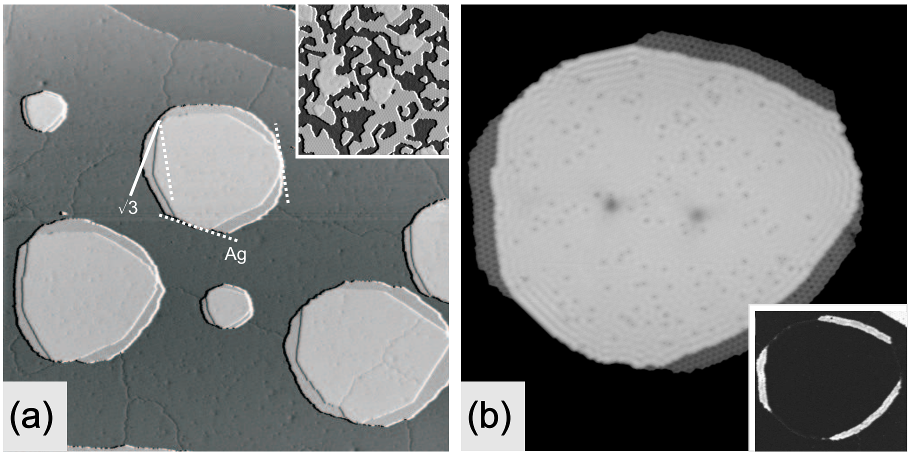

Figure 5.18: (a) 380×380 nm^2: Annealing 0.35 ML (inset 90×90 nm^2) leads to droplet islands consisting of the surface alloy enclosed by pure Pb. The substrate and alloy orientation are indicated by dashed and solid lines, respectively. The orientation of the droplet island edges reveals the Pb induced two-dimensional faceting. (b) 104×104 nm^2. A closer look reveals that the islands edges are indeed aligned with the moiré maxima. Inset: dI/dV image at 2.6 V. The different electronic structures of surface alloy and pure Pb (see Ch. 6) can be spatially arranged by taking advantage of the droplet formation mechanism in combination with the Pb induced faceting.

At 0.35 ML the surface alloy coexists with pure Pb before and after annealing. Upon further deposition the surface alloy is then converted into pure Pb by exchange processes at the step edges. The formation of pure Pb upon annealing has been discussed in detail in Ch. 5.2 (see also Fig. 5.4b). The formation of pure Pb is believed to take place also at the step edges of the droplet islands. The Pb induced two-dimensional faceting discovered in Ch. 5.3.1 governs finally the edge orientation. This is demonstrated in Fig. 5.18a by the dashed and solid lines resembling substrate and alloy symmetry, respectively. In Fig. 5.18b one can directly recognize that the island edges are aligned with the moiré maxima. From Fig. 5.18a it appears furthermore that step edges along the substrate direction are most stable. They resist the faceting process until the Pb coverage gets too high.

The dI/dV image of the droplet island at 2.6 V shown in the inset of Fig. 5.18b illustrates the spatial distribution of the different electronic structure of the pure Pb overlayer with respect to the surface alloy (see Ch. 6).

5.4 Summary

The investigation of the growth of Pb on Ag(111) demonstrates the rich variety of phenomena that appear in the coverage regime below one monolayer. While the large atomic size mismatch of Pb and Ag prevents alloying in the bulk, surface alloying on the other hand is strongly favored [16] up to a coverage of 0.33 ML. The bulk immiscibility of Pb and Ag induces de-alloying at higher coverages.

The alloying mechanism at room temperature is found to be equivalent to the one observed by Schmid *et al.* for the surface alloying of Sn on Cu(111) with LEEM [54]. Upon Pb deposition large pure Pb islands form on top. They are only weakly bound to the Ag substrate which allows for their motion across the whole Ag surface. During that motion Pb atoms of the island exchange randomly with substrate Ag atoms. In consequence the pure Pb islands dissolve leaving behind a track of embedded Pb atoms and clusters together with immobile alloy islands on top. The driving force for that motion is the strong repulsion between embedded Pb atoms and those in the pure Pb islands. That repulsive interaction confines the pure Pb islands to the bare Ag areas. The movement is stopped from coverages of 0.15 ML on, pure Pb islands remain and Pb segregation sets in with increasing coverage.

Annealing at elevated temperatures increases the mobility of Pb and Ag atoms on the surface alloy. Additionally more exchange processes take place upon annealing which leads to a homogenous incorporation of Pb up to 0.33 ML. A disorder-order transition in the surface alloy is observed around a coverage of roughly 0.3 ML, resulting in the well ordered $(\sqrt{3} \times \sqrt{3})$R30° Pb/Ag surface alloy. This transition is due to the entropic contribution to the free energy in analogy to the case of Sb on Ag(111) [61]. A simple hard hexagon model also predicts this order transition at 0.28 ML [63] in good agreement with the STM measurements. The surface alloy is a truly two-dimensional ordered structure at the surface with unique electronic properties as will be shown in the next chapter. The strong reduced mobility of Ag atoms on the alloyed terraces can furthermore explain the surfactant properties of Pb. Due to the alloying the energy barriers for diffusion on terraces and across steps become comparable. In consequence, layer-by-layer growth sets in [61].

The pure Pb overlayer is weakly coupled to the substrate. Despite its weak coupling to the substrate it induces a reconstruction of the underlying Ag surface (see Ch. 6.3 for more details) which is believed to be the driving force for the observed two-dimensional faceting. That is, all island and step facets are aligned with the maxima of the moiré pattern which correspond to the direction of the substrate reconstruction.

Large droplet islands form on wide terraces upon post-annealing more than 0.3 ML at 520 K. They consist of the ordered surface alloy and act as artificial terraces to effectively include the excess Ag atoms that could not reach any natural steps upon annealing due to their limited mobility. In coexistence with the pure Pb phase also the facets of the droplet islands are reoriented in order to follow the moiré maxima. The higher stability of facets along substrate direction leads to a selective faceting.

The ordered surface alloy can be easily prepared by evaporating an arbitrary amount of Pb above 0.33 ML on the Ag surface. The pure Pb fraction desorbs upon flash annealing to 700 K while the ordered alloy structure remains. This simple preparation is compelling because it reliably provides a well defined system also for experiments characterizing its electronic properties without access to structural information like photoemission as will be described in the next chapter.

Chapter 6

Electronic Properties of Pb/Ag(111)

The electronic structure of a surface is of fundamental importance because it governs surface processes including adatom diffusion [67, 68, 77], epitaxial growth [77], surface magnetism and surface chemistry [18, 19, 20]. Surface alloying is a promising approach to modify the electronic properties specifically of metal surfaces because the metal-metal bonds in bimetallic surfaces differ strongly from homonuclear bonds [78]. Thus, it has attracted much interest in recent years as an effective means to altering the catalytic properties of surfaces in order to functionalize them and to tailor new catalytic materials [18, 19, 20]. Nevertheless, most investigations so far concentrate on the structural analysis. Because surface structure and electronic properties are interrelated, there is great need to study and to understand also the electronic structure of surface alloys in detail. The investigation and discussion of the growth of Pb on Ag(111) in the submonolayer regime presented in Ch. 5 revealed a variety of surface alloy structures and their coexistence with pure Pb in several combinations. In this chapter the electronic properties of the different phases are characterized. Several new phenomena will be presented and discussed in the following showing also the close "entanglement" of structure and electronic properties.

At first, the existence of a two-dimensional electronic state that is confined to the ordered surface alloy is reported. In strong contrast to the Ag(111) surface state it shows a parabolic dispersion with a negative effective mass, which indicates a *p*-type band character. It is analyzed by STS and angle resolved photoemission in Ch. 6.1.2. The data of the photoemission experiments show a strong spin-orbit splitting of the alloy state band which is more than four times larger than the well known spin-orbit-split surface state band of Au(111) [79, 80]. The signature in the local density of states caused by this spin splitting, i. e. a peak at the alloy state onset, can be detected by scanning tunneling spectroscopy the for the first time.

The resonant electronic interaction of the Ag(111) surface state electrons with a single Pb atom is studied in Ch. 6.2.1. The surface state is expected to form a bound state at the Pb atom in case of an attractive adatom-induced potential in the region of the adatom-surface state overlap. This attractive potential is provided because the positively charged core of the embedded Pb atom is incompletely screened by the quasi-free electrons of the surface state. The resonant bound state appears to be broadened in the disordered surface alloy phase. This broadening might be a precursor of the formation of the new electronic state that evolves on the well ordered surface alloy phase. The influence of defects in the surface alloy on the new electronic state is also briefly discussed.

Finally, effects in the electronic structure of the pure Pb phase are studied in Ch. 6.3. The moiré pattern of the pure Pb phase turns out to change its contrast at a bias voltage of 2.6 V. This observation together with the appearance of a further superstructure at this distinct energy can be assigned to the onset of the Pb $6p_{x,y}$-bands and their site dependent shift in onset energy. A short summary closes this chapter.

6.1 The Ordered Pb/Ag Surface Alloy

6.1.1 Surface States and Spin-Orbit Splitting

The electronic structure of the bare Ag(111) surface is well investigated [28, 81, 82, 83, 84]. It is governed by a Shockley type surface state that exists due to the broken symmetry at the crystal surface. It is localized in a large *sp*-band gap of the bulk band structure projected onto the (111) surface. This gap reaches down below the Fermi energy at the center of the surface Brillouin zone and supports the occupied surface state. A Shockley type surface state exists for all fcc(111) surfaces of the nobel metals [85]. The electrons of this state form a well localized two-dimensional, quasi-free electron gas parallel to the surface. Thus, the state has a parabolic dispersion around $\overline{\Gamma}$

$$E = E_0 + \frac{\hbar^2}{2m^*}k^2, \tag{6.1}$$

with an effective mass $m^* = 0.4m_e$ and an onset energy $E_0 = -65\,\text{meV}$ for Ag(111) as measured by STS [82]. The electrons are confined to the vicinity of the top layer, decaying exponentially into both the vacuum and the bulk. The influence of overlayers and confinement on the surface state is of ongoing interest in order to learn how the electronic properties of the surface can be controlled and modified [86, 87, 88, 89]. Covering a noble metal surface with a rare gas or metal overlayer resulted up to now in a quenched surface state or in a slight variation in onset energy and effective mass.

An additional phenomenon that is — like surface states — related to the broken symmetry at the surface is the splitting of the surface state band caused by spin-orbit coupling (SOC). The SOC is a relativistic effect where an electron moving in an electrical field experiences a magnetic field in its rest frame. This magnetic field induces a Zeeman splitting that lifts the degeneracy of the different spin states causing a splitting in energy. This effect can be expressed by the Hamiltonian

$$H_{SOC} = \frac{\hbar}{4m^{*2}c^2}(\overrightarrow{\nabla} V \times \overrightarrow{p}) \cdot \overrightarrow{\sigma}, \tag{6.2}$$

where V is the potential in which the electrons move, $\overrightarrow{p}$ is the momentum and $\overrightarrow{\sigma}$ the Pauli spin operator.

Due to the conservation of both, inversion symmetry and time reversal symmetry, SOC-induced spin splitting is forbidden in crystals with inversion symmetry. That leads to a double degeneracy of each band [80, 90]. However, at the surface the inversion symmetry of the crystal is broken. Thus, the spin degeneracy can be lifted. The two-dimensional electron gas of the surface state is quasi-free in the surface plane and experiences therefore an electric field gradient along the surface normal. The result is a splitting of the original parabolic band into two branches with energy

$$E = E_0 + \frac{\hbar^2 k^2}{2m^*} \pm \alpha k = E_0' + \frac{\hbar^2}{2m^*}(k \pm k_0)^2, \tag{6.3}$$

where $\hbar^2 k_0 = m^*\alpha$ and $E_0' = E_0 - \hbar^2 k_0^2/(2m^*)$. The magnitude of the observed splitting is underestimated in the nearly free electron model by orders of magnitude [84, 80].

The first experimental observation of a split surface state band due to SOC was reported for the Au(111) surface state [79, 84]. Upon deposition of Ag on Au(111) the Au(111) band splitting is reduced with increasing Ag coverage. Annealing leads to the formation of a Ag/Au alloy and the splitting gets stronger again with increasing Au content in the alloy [91]. However, the band splitting in the alloy gets never stronger than for the pure Au(111) surface. An increase of the SOC-induced splittings was found for the W and Mo (110) surface after deposition of one monolayer Li [92]. Recently also for the low-index surfaces of Bi a strong SOC induced splitting of the surface state bands was reported [93]. The influence of SOC on the bare Ag(111) surface state is found to be extremely weak and could not yet be resolved experimentally [84].

All results just mentioned were obtained by angle resolved photoemission experiments. In STM measurements the dispersion of degenerate bands can only be accessed via the energy dependent standing waves in the LDOS (see Ch. 6.1.2). The SOC induced splitting of the Au(111) surface state can not be observed in standing wave images because electron waves with opposite spins do not contribute to the interference pattern. In consequence only an average k vector — resulting from scattering processes with spin conservation — is observed in the standing wave patterns and the dispersing band determined by STS is located just between the spin-split branches [80]. In contrast, it has been shown that signatures of SOC can be detected by STM for split surface state bands within a more complex Fermi surface. According to the study by Pascual *et al.* the interference of electron waves on Bi(110) is determined by spin-conserving scattering processes. That results in completely different wave patterns than expected for degenerate surface state bands [94].

In the following sections it will be shown that the ordered $(\sqrt{3}\times\sqrt{3})$R30° Pb/Ag(111) surface alloy provides — in striking contrast to the bare Ag(111) surface — a two-dimensional state that disperses towards lower energies with a negative effective mass. In particular a large spin-orbit-splitting of the alloy state band is found. This effect is quite surprising because of the vanishing SOC-induced band splitting of the Ag(111) surface state. The splitting causes furthermore a singularity in the local density of states which is detected by means of STS for the first time.

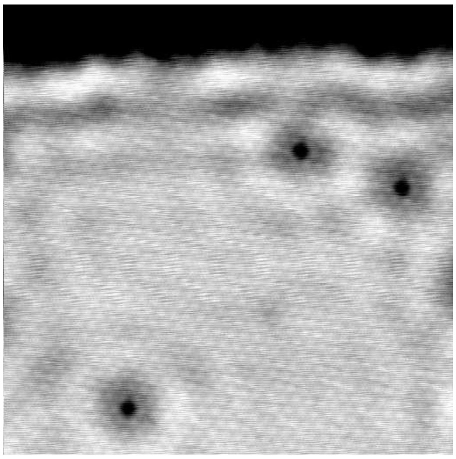

Figure 6.1: 20×20 nm^2. Topographic STM image where standing waves are apparent on the surface alloy phase, scattered off the alloy border and defects. The waves are superimposed to the atomic corrugation of to the Pb atoms forming the surface alloy.

6.1.2 A Two-Dimensional Electronic State in the Surface Alloy

In Ch. 5.2.1 it was found that by increasing the coverage to 1/3 ML the Pb structure on Ag(111) evolves into a long-range ordered surface alloy as is shown in Fig. 5.9. In the topographic STM image in Fig. 6.1 a quantum interference pattern of standing electron waves, caused by scattering of surface electrons at imperfections within the surface alloy, shows up. It is superimposed to the atomic corrugation of the alloy Pb atoms and indicates the existence of electronic states around E_F in the surface alloy.

By recording dI/dV maps on the surface alloy the standing wave pattern is used to analyze the electronic state in the alloy quantitatively. A topographic image of the area of interest can be seen in Fig. 6.2a, where the alloy structure is not atomically resolved but appears as a smooth structure in light gray. Defects in the alloy lattice appear as dark spots which act as scattering centers producing the standing wave patterns. The simultaneously recorded dI/dV maps are shown in Fig. 6.2b and c.

The standing wave patterns are shown for two different energies, +200 meV and +400 meV, in Fig. 6.2b and c, respectively. The wave length at +200 meV is smaller than at +400 meV, indicating a dispersion with a negative effective mass. The wave vector of the standing wave patterns is determined by calculating the Fourier transform of the image [95]. Fig. 6.2d shows the Fourier transform of Fig. 6.2b, i. e. the distribution of momentum values at a particular energy with light and dark areas corresponding to high and

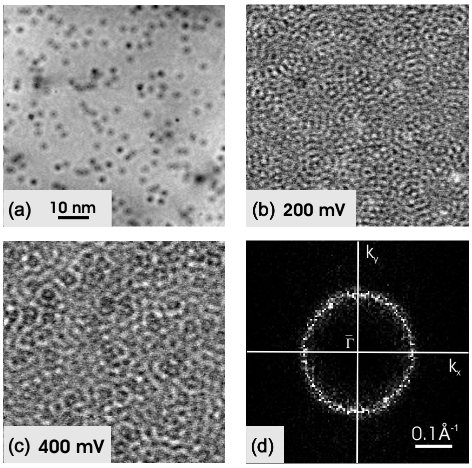

Figure 6.2: (a) The defects in the surface alloy phase (black spots) are equally distributed over the whole surface. (b)-(c) Mapping the LDOS at distinct energies yields standing waves around the imperfections, indicating a coherent state. (d) By Fourier transformation the respective values of $k_{||}$ are evaluated, leading to the dispersion relation of the new electronic state.

low amplitude, respectively. The distribution of momentum values is clearly circular with a radius of $k \approx 0.15\,\text{Å}^{-1}$ indicating an isotropic dispersion of the energy band. The momentum distribution in Fig. 6.2d is representative for standing wave images at other energies.

From these values of the Fourier transforms the full dispersion $E = E_0 + \hbar^2 k^2/2m^*$ was determined. This is shown in Fig. 6.3a. The data points have been fitted to a parabolic energy dispersion which yielded a band maximum at $E_0 = +0.64\,\text{eV}$ and an effective mass of $m^* = -0.19\,m_e$, where m_e is the free electron mass. For comparison the dispersion of the surface state of the bare Ag(111) surface is shown as a dashed line along with the projected bulk band structure of Ag as a hatched area. The effect of backfolding of the Brillouin zone due to the larger unit cell of the alloy phase can be excluded, because the measured k-range is still far away from the nearest zone boundary, which is $\overline{\text{M}}_{\text{alloy}} = 0.73\,\text{Å}^{-1}$ (see Fig. 6.3b).

From Fig. 6.3a it can be seen that the electronic structure of the Ag(111) surface changes dramatically in the Pb/Ag(111) surface alloy compared to the bare Ag(111) surface. The change in sign of the effective mass changes the electron-like Fermi surface of the bare Ag(111) surface state to a hole-like Fermi surface. The band dispersion of the alloy state can be traced well within the projected band structure of the Ag substrate.

A typical STS spectrum for the ordered alloy phase can be seen in Fig. 6.4. The dI/dV vs. V curve shows a step-like feature with a peak at the onset having a maximum at $E_0 = +0.64\,\text{eV}$. The step feature is interpreted as the onset of a two-dimensional band in the surface alloy. The orientation

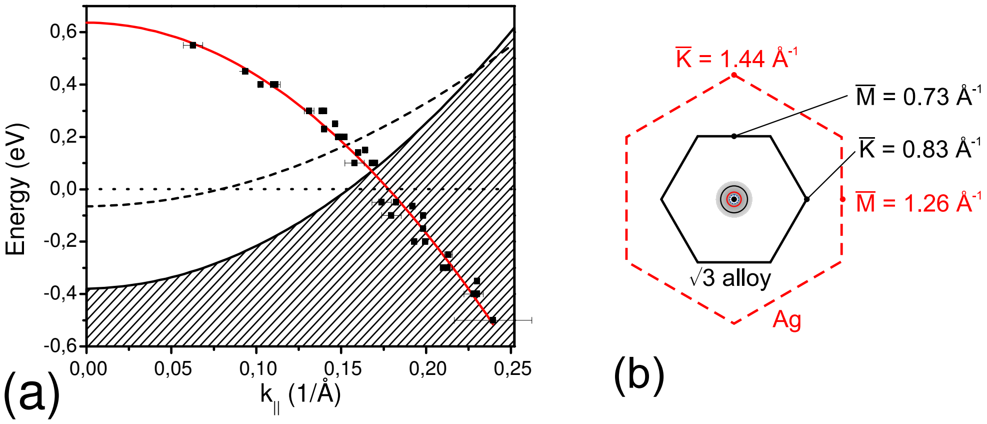

Figure 6.3: (a) Dispersion relation for the electronic state on the surface alloy. The black squares are the measured data points, the solid line is the result of a parabolic fit. One obtains an effective mass of $m_* = -0.19m_0$ and $E_{\overline{\Gamma}} = 0.64$. For comparison the Ag(111) surface state dispersion is plotted as dashed line. The hatched area is occupied by projected Ag bulk states. (b) Surface Brillouin zone for the bare Ag(111) surface (red) and the $(\sqrt{3} \times \sqrt{3})$R30° surface alloy (black). The area accessed by STS is indicated gray. Red and black circles show k_F for the Ag(111) surface state and the alloy state, respectively. Backfolding of the Ag surface state band can be excluded as origin of the surface alloy state.

of the step indicates a band which disperses towards lower energies with a negative effective mass in agreement with the just derived dispersion relation. The origin of the peak will be discussed further below in the context of SOC-induced splitting of the new state band. The features in the dI/dV-spectrum do not change as a function of lateral position on the surface alloy.

To investigate the nature of the new state first DFT calculations have been performed for the Pb/Ag(111) surface alloy structure. They reproduce the experimentally determined band in Fig. 6.3 [96]. The calculations show that the band has a sp_z-character around the $\overline{\Gamma}$ point. It acquires a more $p_{x/y}$-character for higher $k_{\|}$.

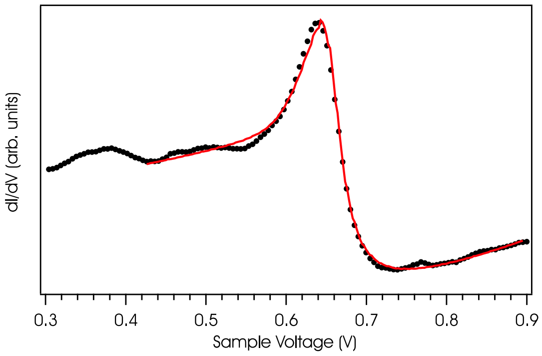

Figure 6.4: dI/dV point spectrum on the surface alloy. At +0.64 eV The onset of the surface alloy state that disperses towards lower energies occurs. It is superimposed by a strong peak. The read line is a fit of the LDOS assuming a singularity due to spin-orbit splitting.

6.1.3 Photoemission Spectroscopy on the Surface Alloy and Spin-Orbit-Splitting

Angle resolved photoemission experiments have been performed to obtain further results on the electronic properties of the new state in the surface alloy. Photoemission is in contrast to STS a spatially averaging technique, but it allows to resolve the k-space. Both, the symmetry points at the Brillouin zone boundaries and occupied states at energies several eV below E_F can be explored with this technique, while unoccupied states above E_F are not accessible. A homogenous well ordered surface alloy covering the whole surface can be easily prepared by evaporation of more than 0.33 ML Pb and subsequent annealing at 700 K as mentioned in Ch. 5.4. Therefore it is well suited for a photoemission investigation.

The photoemission data presented here have been obtained at the Swiss Light Source with a Scienta photoemission spectrometer. The detector has an energy resolution of 5 meV and an angular resolution below 1°. Fig. 6.5 shows the band structure of the surface alloy along the $\overline{\Gamma}\,\overline{\mathrm{K}}$ direction recorded with a photon energy of 21.2 eV. Contributions from bulk bands and those related to the surface electronic structure can be distinguished by their different symmetry properties. Surface related bands are symmetric with respect to the surface high symmetry points, bulk bands are not. Thus, the band that is crossing the $\overline{K}$-point around E_F and the low lying Ag d-bands around 4 eV below E_F can be identified as bulk bands.

A steeply downward dispersing band around $\overline{\Gamma}$ shows the highest intensity. A closer look yields the existence of a further band in close vicinity to the

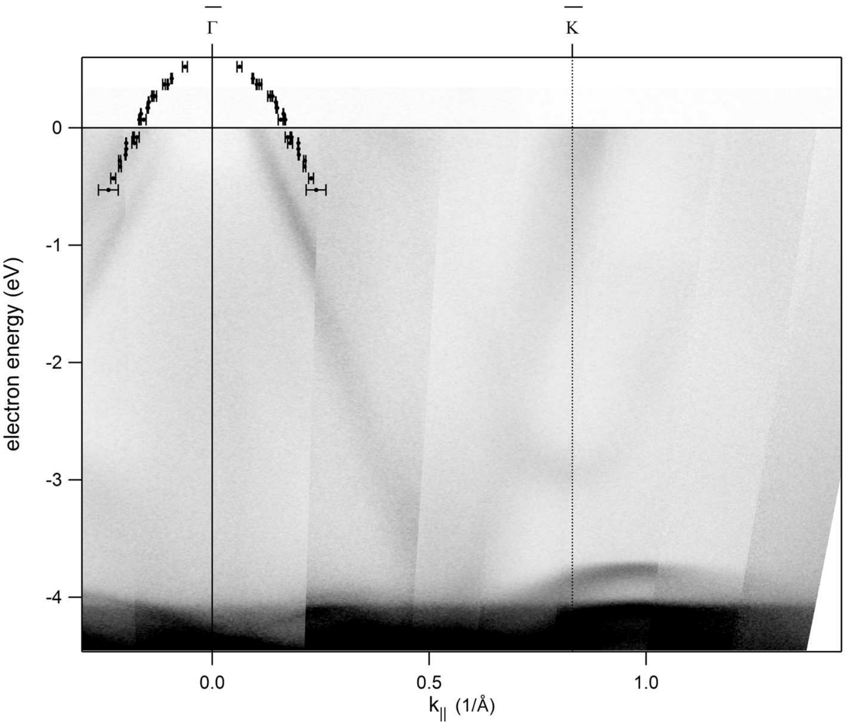

Figure 6.5: Photoemission data of the surface alloy band structure along $\overline{\Gamma}\,\overline{\mathrm{K}}$. The dispersion relation determined by STS is added for comparison.

intense one. Another surface related band has its minimum at the $\overline{K}$-point 3 eV below E_F and disperses towards higher energies. The data obtained by STS (see Ch. 6.1.2) are superimposed to the photoemission plot. It appears that the STS data points are located in between the two neighboring steeply downward dispersing bands.

Recent measurements on the $(\sqrt{3} \times \sqrt{3})$R30° Bi/Ag(111) surface alloy reveal a similar band structure compared to the Pb/Ag surface alloy with the band maxima shifted below the Fermi level. The observed neighboring bands are degenerate in their onset energy but shifted by a wave vector $\pm k_0$ with respect to $\overline{\Gamma}$. This gives strong evidence — also for the Pb/Ag system — that the spin degeneracy is lifted and the bands are spin-polarized due to spin-orbit interaction [97]. The SOC-induced splitting of a parabolic band can not be observed in standing wave STM-images as discussed in Ch. 6.1.1.

Instead, the dispersing band determined by STS is located in between the spin-orbit split branches. The comparison of the dispersion relation found by STS with the photoemission data (Fig. 6.5) imply that this is indeed the case for the Pb/Ag surface alloy.

6.1.4 The Signature of Spin-Orbit Coupling in STS

The following considerations concerning the SOC-induced band splitting reveal a general way to detect a large splitting by STS. As derived in Ch. 6.1.1 a splitting of the original parabolic dispersion relation into two branches occurs for the two-dimensional electron gas in the surface alloy with energy

$$E = E_0 + \frac{\hbar^2}{2m^*}(k \pm k_0)^2. \tag{6.4}$$

These branches are visible in the photoemission data and schematically illustrated in Fig. 6.6a. The rotational symmetry around $\overline{\Gamma}$ is indicated by the horizontal cut through the dispersion relation, leading to concentric circles in the k-space as shown in Fig. 6.6b. The density of states (DOS) of the spin-split bands can be written as

$$D(E) = \int \delta(E - E(\overrightarrow{k}))\frac{d\overrightarrow{k}}{4\pi^2} \tag{6.5}$$

While the DOS of a spin-degenerate band ($k_0 = 0$) increases step-like at the onset energy E_0 one finds for the DOS of the two-dimensional spin-orbit split electron gas (Eq. 6.4)

$$D(E) = \begin{cases} \frac{|m^*|}{\pi\hbar^2} \cdot \frac{k_0}{\sqrt{\frac{2m^*}{\hbar^2}(E-E_0)}} & ; \sqrt{\frac{2m^*}{\hbar^2}(E - E_0)} \leq k_0 \\ \\ \frac{|m^*|}{\pi\hbar^2} & ; \sqrt{\frac{2m^*}{\hbar^2}(E - E_0)} > k_0 \\ \\ 0 & ; m^*(E - E_0) < 0. \end{cases} \tag{6.6}$$

According to that calculation the lateral shift of the energy bands towards $\pm k_0$ induces a singularity in the DOS at the state onset energy E_0 as shown in Fig. 6.6c. The DOS shows a $1/\sqrt{E}$-dependence from E_0 up to the crossing point of the two branches at $\overline{\Gamma}$. This is quite surprising because this behavior is similar to that of one-dimensional systems. Below the crossing point the

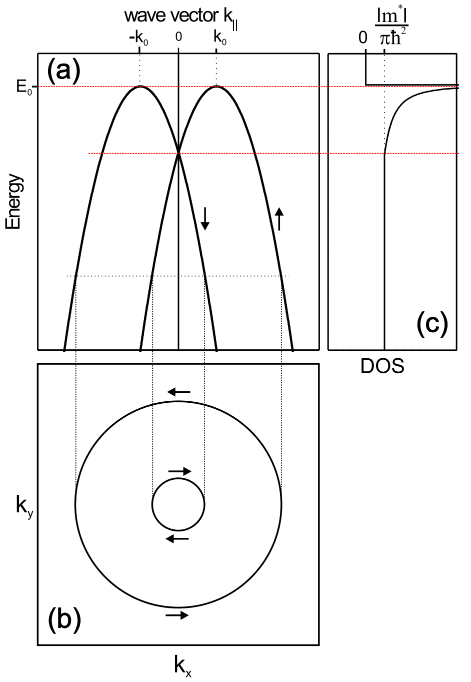

Figure 6.6: (a) Schematic plot of the spin-split surface alloy state. Due to the broken symmetry at the surface the spin degeneracy is lifted. The spin-split parabolic bands are shifted in the k-space symmetrically around $\overline{\Gamma}$. (b) Cut along the dashed red line. It illustrates the rotational symmetry of the bands around $\overline{\Gamma}$. The band maxima at $k \neq 0$ give rise to a singularity in the DOS (c) that is detected in the dI/dV spectrum (Fig. 6.4).

DOS adopts a constant value which is characteristic for a two-dimensional nearly-free electron gas.

In reality this singularity is broadened by the finite lifetime of the alloy state electrons. However, it gives rise for the peak in the dI/dV-spectrum in Fig. 6.4 which is located just at the onset of the alloy state. Fitting the peak by taking the broadening and the exponential increase of the tunneling current for higher bias into account, leads to an excellent agreement with the experimental data (red line). The fit parameters are $E_0 = 0.657\,\mathrm{eV}$, $k_0 = 0.06\,\text{Å}^{-1}$ and an effective Lorentzian broadening $\Gamma_L = 36\,\mathrm{meV}$. The measured spin-splitting with a shift $k_0 = 0.06\,\text{Å}^{-1}$ is also in good agreement with $k_0 \approx 0.045\,\text{Å}^{-1}$ obtained by photoemission. It is about four times larger than the splitting of the Au(111) surface state band. That is the first time, that a feature detected in a STS-spectrum can be directly related to the SOC-band splitting of an electronic state at the surface.

It appears that surface alloying is a promising new way to fabricate strongly spin-split two-dimensional states on a surface. These striking results obtained by two complementary experimental techniques demonstrate the great potential of combined STS/ARUPS-studies.

6.1.5 Standing Waves as Probe for the Growth Process

The existence of the new electronic state, and thus the observable standing wave pattern on the ordered surface alloy phase, allows for a simple identification of structures evolving during the growth of Pb on Ag(111) which has been discussed in Ch. 5 in detail. Two examples for this connection shall be given here.

The first example concerns the distinction of ordered and disordered alloy regions. At a coverage of 0.35 ML Pb evaporated at room temperature (see Fig. 5.4a) a dI/dV-map has been recorded simultaneously together with the topographic image at a bias voltage of 100 mV as is shown in Fig. 6.7a. One can clearly distinguish three regions with different contrast, areas in light gray, darker regions and patches exhibiting the standing wave patterns of the new state. A direct comparison with the topographic image yields that the standing waves appear close to step edges and on the surface alloy islands that are surrounded by the network of pure Pb islands imaged dark in the dI/dV map.

The light gray areas are identical with the disordered alloy between the islands, embedded in the surface layer. The brighter contrast reveals a higher local density of states in this phase compared to the pure Pb phase on top. But it is even more notable that no standing wave pattern has evolved there. That means that, in contrast to the surface alloy islands, the alloy phase in the surface is too disordered to develop a coherent electronic state. Thus, the existence of a standing wave pattern is a sensitive measure of the local degree of order in the surface alloy system.

In a second example the electronic properties of the ordered surface alloy are used to study the subsurface composition of the system. When discussing the formation of surface alloy islands the question arose, whether they grow on pure Ag or not. The dI/dV image of a droplet island that has formed after annealing 0.35 ML Pb at 520 K in Fig. 6.7b provides an answer. Again, the standing wave pattern is apparent all over the place except for the island facets that are decorated by pure Pb. The first example discussed here leads to the conclusion that the whole surface alloy area, the alloy island and its surrounding, is uniformly well ordered.

The Fourier transform of that image (inset of Fig. 6.7b) yields a circular distribution of momentum values as described in Ch. 6.1.2. Only one

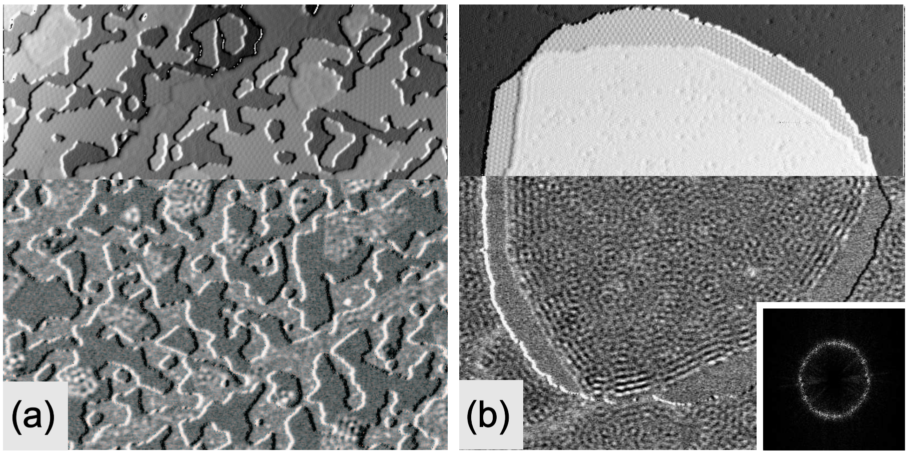

Figure 6.7: (a) 135×135 nm^2, 100 mV. dI/dV image of the Ag surface covered by 0.35 ML Pb after room temperature deposition. The ordered surface alloy phase can be distinguished from the disordered alloy phase by the standing wave pattern. The pure Pb phase appears darkest. (b) 135×135 nm^2, 200 mV. dI/dV image of a droplet island. The electronic structure of the alloy phase is unchanged on the droplet. This proves, that pure Ag is below.

distinct radius, i. e. momentum value, is found for both island and surface layer. Consequently, the electrons in both regions are exposed to the same potential. If the alloy island would grow on an area with different composition compared to the alloy in the surface layer, the potential landscape and thus the properties of the electronic state would alter. This proves that all surface alloy areas are covering the pure Ag surface as discussed in Ch. 5.

6.2 Localized Electronic States

Up to now, the discussion was focussed on the electronic properties of the perfectly ordered surface alloy state. Apart from that, the high spatial resolution of scanning tunneling spectroscopy reveals also local electronic effects at single atoms, defect sites and domain walls. The investigation of these local effects is presented in this section. First, the interaction of a single Pb atom that is incorporated in the surface layer with Ag(111) surface state electrons is studied. The quasi-free two-dimensional electron gas is found to

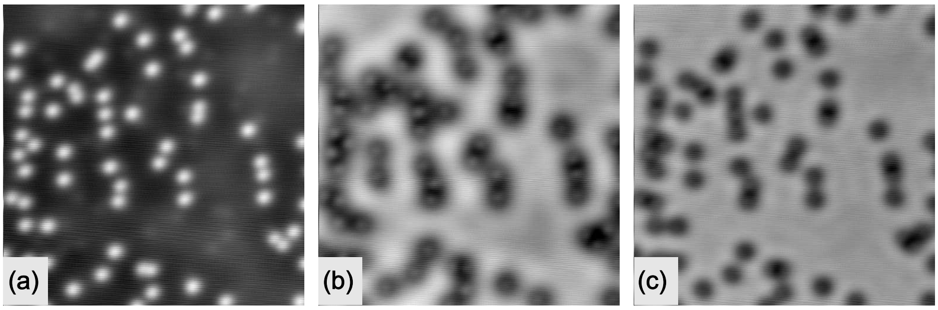

Figure 6.8: 20×20 nm^2, single Pb atoms in the Ag(111) surface imaged at (a) -0.5 V, (b) +0.2 V (c) +0.5 V. The contrast of the Pb atoms shows a strong bias dependence.

form a localized bound state at the Pb atom site that appears in the dI/dV spectrum as resonance peak. This peak broadens in the dilute disordered alloy. This is the first reported observation of a resonant bound state for incorporated atoms. It proves the predicted universality of this phenomenon. Finally, also defects and domain walls yield peculiar electronic properties that are observed in dI/dV images.

6.2.1 Surface State Localization at Single Pb Atoms

Fig. 6.8 shows three examples for the appearance of incorporated Pb atoms in an STM image depending on the bias voltage. The Pb atoms appear as bright protrusions at -0.5 V, are additionally surrounded by a dark depletion at +0.2 V and appear completely dark at +0.5 V. This bias dependence can be studied in detail by spatially resolved scanning tunneling spectroscopy. The topographic image of a single Pb atom in the center is shown in Fig. 6.9a. Several dI/dV spectra where recorded while the tip was scanning across the atom (the first scan line of Fig. 6.9a corresponds to the tip position). Fig. 6.9b shows the differential conductance data $dI/dV(E, x)$ represented by gray levels as function of the lateral distance x and bias energy E. Apart from the atom position one recognizes a rather sharp transition from black (low LDOS values) at energies below -60 meV to bright (high LDOS) above. This is the onset of the Ag(111) surface state as mentioned above.

A 1 nm wide seam of high LDOS also below -65 meV interrupts that transition at the Pb site in the center of the plot. It has sharp borders, broadens towards lower energies and develops a peak at -65 meV in the center

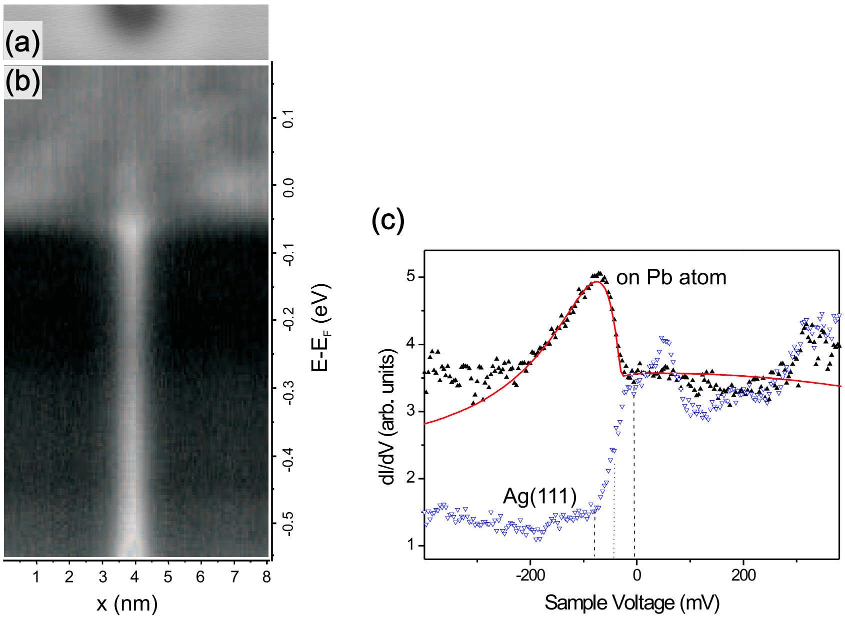

Figure 6.9: (b) Plot of the differential conductance dI/dV for a single Pb atom incorporated in the Ag(111) surface as function of the lateral distance x and of bias energy $E = eV$ with respect to E_F. The spectra are taken along the first scan line of the image (a). (c) Point spectrum in the center of a Pb atom (black triangles) and on the bare Ag(111) (blue triangles). The red line gives the theoretically predicted peak shape and is fitted to the experimental data.

of the Pb atom. Above the maximum at the surface state onset the LDOS on top of the Pb atom starts to decrease. From the onset on an about 1.5 nm broad depletion evolves around the Pb atom. It becomes more narrow with higher energies and dominates the on atom LDOS at higher energies.

The bias dependent contrast shows that the tunneling current always contains a combination of structural and electronic contributions. The complexity of the behavior of the tunneling current is under ongoing theoretical investigation [98, 99, 100, 101]. Nieminen *et al.* investigated the contrast mechanism for O_2 molecules on Ag(100) theoretically. The observed contrast changes are very similar to the ones reported here for single Pb atoms. In the formalism used by Nieminen *et al.* the contribution of different tunneling channels (for example tunneling from the tip through the adsorbate or directly to the surface) and their phase relations is analyzed. The p_z orbitals of the oxygen atoms within the molecule are found to be independent from each other which allows for the comparison with a single Pb atom. As for the O_2 molecule the p_z orbital is believed to contribute most to the tunneling current through an adsorbed Pb atom because it extends rather far to the vacuum. According to the calculations the contrast changes originate from the bias dependent change in the phase relation of different tunneling channels. That leads to constructive or destructive interference between the tunneling channels and finally to the observed image contrast.

A single dI/dV-spectrum recorded right in the center of a Pb atom is shown in Fig. 6.9c (black triangles). It is compared with the point spectrum on the bare Ag(111) surface (blue triangles). The peak which can be recognized also in the graylevel plot is located at the lower edge of the step like surface state onset. A similar feature has been observed for Ag, Co and S adatoms on the Ag(111) surface [102, 103] and for Cu and Co adatoms on the Cu(111) surface [102, 104]. For all these examples the observed peak position is just below the surface state band edge and does not depend on the onset energy or adatom species.

The peak can be attributed to the localization of the two-dimensional Shockley type Ag(111) surface state at the Pb atom. According to a fundamental theorem by Simon any two-dimensional electron gas forms a bound state due to a localized attractive potential [105]. It gives rise for a resonance in the local density of states located just below the surface state band edge. The Newns-Anderson Hamiltonian, describing a single adsorbate level of energy ε_a interacting with the bulk Bloch states, leads to the LDOS of the adsorbate [106]. The LDOS including the interaction with the two-dimensional surface state can be expressed as

$$n_a(E) = \frac{1}{\pi} \frac{\Delta(E)}{[E - \varepsilon_a - \Lambda(E)]^2 + \Delta(E)^2}, \tag{6.7}$$

where $\Delta(E)$, the imaginary part of the self energy $\varepsilon = \Lambda + i\Delta(E)$, contains contributions from the coupling of the adsorbate level to the bulk and the surface states, respectively. The results presented here reveal exactly the predicted behavior. This is proved by adapting the theoretically predicted curve to the experimental data as demonstrated by the red solid line in Fig. 6.9c. The overall agreement is very good. The slight deviation of the theoretical curve from the experimental data remains to be clarified. It is worth mentioning that the data in this energy range are not shown in the publication of Limot *et al.* [102].

These findings extend the reported observations of the surface state localization from adatoms also towards substitutional atoms in the first surface layer. That confirms the expected universal behavior of this fundamental phenomenon.

6.2.2 Coexistence of the Ag(111) Surface State and the Disordered Alloy

Fig. 6.10a gives an impression of the electronic structure that evolves for the disordered alloy which forms during annealing Pb coverages below 0.3 ML at 520 K (see Ch. 5.2.1). The spectroscopic data were acquired along the yellow dashed line in the topographic image at the bottom of Fig. 6.10a. From the intensities of the gray scale plot one can recognize at the Pb sites a higher LDOS below the surface state onset than for a single Pb atom. Due to the equal distribution of the Pb atoms the surface state electrons get more and more confined with increasing coverage. The surface state onset in the remaining Pb free regions is furthermore strongly broadened.

Two point spectra are extracted from Fig. 6.10a as marked by the colored dashed lines and serve as examples for regions with and without Pb. They are plotted in Fig. 6.10b. The green data points are taken on free spots of the Ag substrate. The onset of the Ag surface state is apparent around E_F. It has a width of 240 meV which is strongly broadened compared to 70 meV in Fig. 6.9c and its center is shifted about 25 meV towards E_F. This assignment was carried out according Ref. [107]. The depopulation of the Ag surface state is ascribed to the lateral confinement of the surface state electrons due to the surrounding Pb atoms. A similar depopulation effect has been reported for the surface state electrons confined to small Ag(111) terraces [89]. The increase in the LDOS around 0.15 V originates from the standing wave maximum that exists at the respective lateral position.

The dI/dV spectrum recorded on the disordered alloy phase (red data points corresponding to the dashed red line in Fig. 6.10a) has changed compared to spectrum on top of a single Pb atom in Fig. 6.9c. However, it still remains correlated with the surface state spectrum. The former sharp and resonant peak feature is split into two contributions. At first, a broad maximum reaches from -0.2 V to +0.15 V. This broad feature is superimposed by

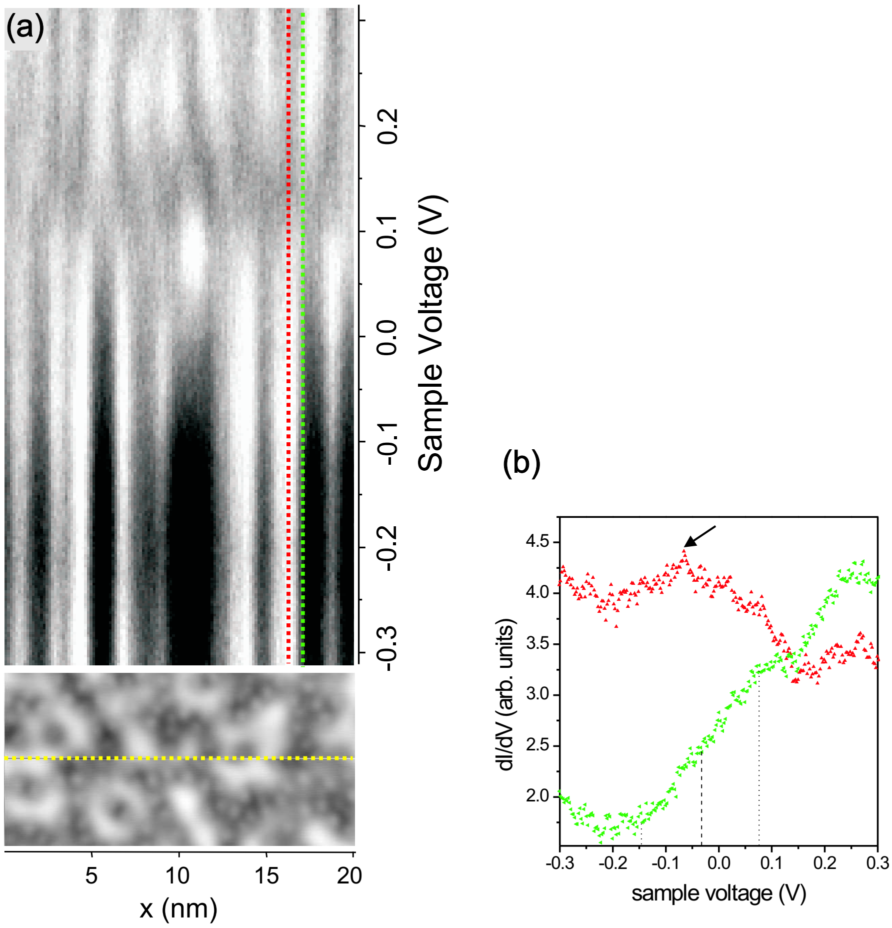

Figure 6.10: (a) Plot of the differential conductance dI/dV for the disordered Pb/Ag(111) surface alloy as function of the lateral distance$x$ and of bias energy $E = eV$ with respect to E_F. The spectra are taken along the dashed yellow line in the image below. (b) dI/dV spectra along the color coded dashed lines in (a). Both features, the resonant bound state (red) and the surface state onset (green) have strongly broadened. The black arrow depicts a small sharp peak visible only directly on the Pb atoms.

a very narrow peak marked by the arrow. It is located at -65 mV which is the peak position also for the single Pb atom. Its width has decreased from 50 mV to 30 mV. This sharp resonance does not appear in all line spectra.

It is rather detected only when the tip is positioned directly on top of a Pb atom and is therefore assumed to still originate from the interaction of the Pb atom with the remaining Ag surface state electrons.

The broad feature that appears in the disordered alloy phase is believed to be due to the interaction between the incorporated Pb atoms. It can possibly be interpreted as a precursor of the two-dimensional electronic state that exists in the ordered ($\sqrt{3}$ x $\sqrt{3}$)R30° surface alloy phase as studied in detail in Ch. 6.1.2.

6.2.3 Defects and Domain Walls

In this section local changes in the electronic structure of the ordered ($\sqrt{3} \times \sqrt{3}$)R30° surface alloy are demonstrated. The defects in the surface alloy were argued to be Ag atoms that have not been substituted by Pb during the alloying process. The domain walls separate different commensurate surface alloy domains (see Ch. 5.2.2). Consequently, these sites perturb the electronic structure of the perfectly ordered surface alloy. One effect of this perturbation is the scattering of the alloy state electrons. The resulting standing wave pattern is observed in dI/dV-maps (Fig. 6.2b and c) and enables to determine the dispersion relation of the new state as explained in Ch. 6.1.2.

A further effect appears in dI/dV-images at bias voltages around the onset of the surface alloy state. Fig. 6.11a,c,d and (e) show dI/dV images on the surface alloy at 0.66 eV, 0.68 eV, and 1.2 eV, respectively. The defects appearance in these LDOS maps is energy dependent. At 0.66 eV and 0.68 eV the defects appear as star-like rings with a black spot in the center (Fig. 6.11a and d). From the atomical resolved data in Fig. 6.11b one can conclude that the tips of the star structure point between the Pb atoms of the alloy. This is illustrated schematically by a dashed line. At 1.2 eV (Fig. 6.11d) they appear as white spots on a dark background. At lower bias voltage the standing wave pattern of the surface alloy state evolves. At 0.66 eV (Fig. 6.11a), which is still at the very beginning of the alloy state onset, their wavelength is large and defects and standing waves do not seem to be correlated. At 0.63 eV in contrast (Fig. 6.11c) most of the bright rings are embedded in and interconnected by a dark depletion zone while a high local density of states due to the standing wave maxima fills the space in between.

The domain walls show a similar bias dependence in the dI/dV images. Around the alloy state onset they appear as gray lines in a black groove (see

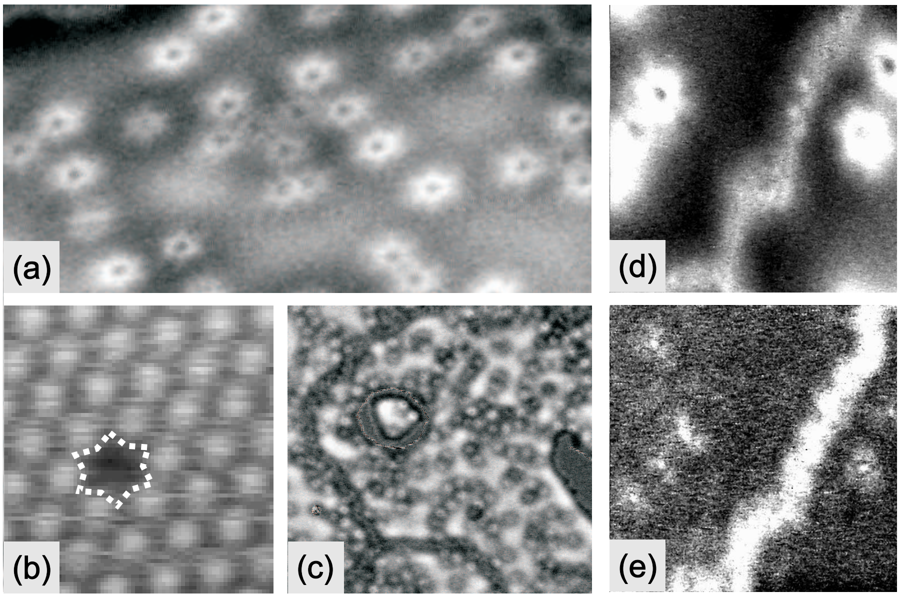

Figure 6.11: Small scale dI/dV-images resolve the star like structure of the defect appearance. (a) 42×42 nm^2, 0.66 V (b) 29×29 Å. Atomically resolved Pb atoms of the surface alloy. The defect area is indicated by the dashed star (c) 100×100 nm^2, 0.63 V (d) 19×19 nm^2, 0.68 V (e)21×21 nm^2, 1.2 V

Fig. 6.11c). They can also be recognized at energies above the alloy state onset. One can see that the domain wall brightness has further increased in Fig. 6.11e at 1.2 V while the defects have shrunk to small white spots.

The origin of these changes in the local electronic structure of the surface alloy is not clarified yet. In analogy to a single Pb atom in the Ag(111) surface it could well be that the defects induce a resonant bound state of the alloy state electrons. A possible explanation for the increased LDOS in the domain wall regions at energies above the alloy state might be the formation of a one-dimensional surface state along the domain walls. Such a state has been reported for the Fe(100) surface after alloying with Si [108]. Its onset is shifted from 0.3 eV for the two-dimensional surface state on clean Fe(100) to 0.6 eV in the one-dimensional case. Also for the Si/Fe alloy the domain walls appear in dI/dV images at the respective energies as bright lines in the dark alloy. Further experiments and complementary theoretical investigations are needed to gain further insights in the nature of these effects.

6.3 Electronic Properties of the Pure Pb Overlayer

The moiré pattern evolving on the pure Pb overlayer was explained in Ch. 5.3 to originate from the 4.5° rotation of the overlayer with respect to the Ag substrate. In this section the interplay between structural and electronic effects will be elucidated. While the ball model in Fig. 5.13b was sufficient to reproduce the geometrical relations between the lattice parameters and the moiré pattern it has to be refined to cope with the additional observations presented here.

6.3.1 Inverse Corrugation and Contrast Reversal

The contrast of the moiré pattern appears to be inverted compared to a simple ball model. In such a model the Pb atoms occupy hollow sites as well as positions on top of the substrate due to the rotation of the overlayer with respect to the Ag substrate. Consequently, Pb atoms on on-top sites would appear highest. Experimental and theoretical investigations of the 4×4 Pb superstructure on Cu(111) reveal in contrast a corrugation opposite to the one obtained by a simple ball model [71]. The reason for this inverse corrugation is a strong relaxation of the first Cu substrate layer to reduce the energy cost for the unfavored on top constellation. Thus, the contrast is lowest for on top positions.

The black, gray and white filled circles in Fig. 6.12c indicate the resulting contrast expected for different sites in the ball model. By adding also the second Ag layer to the model, very good agreement between the STM image in Fig. 6.12b and the ball model with corrected contrast is obtained also for the Pb overlayer on the Ag(111) surface. The three intensities visible in the STM image (black, gray and white in the model) that induce an additional structure between the maxima can be reproduced only with the second Ag layer included. The electronic nature of this effect is discussed further below in connection with the observation of a changing image contrast around 2.6 eV above the Fermi energy.

Fig. 6.12a and (b) belong to one single STM image where the bias voltage is changed from 2.5 V (a) to 0.42 V (b) after half the scan. The moiré pattern in Fig. 6.12a changes contrast upon switching the bias voltage. The upper half of the image (high bias) has a larger contrast which is equalized to

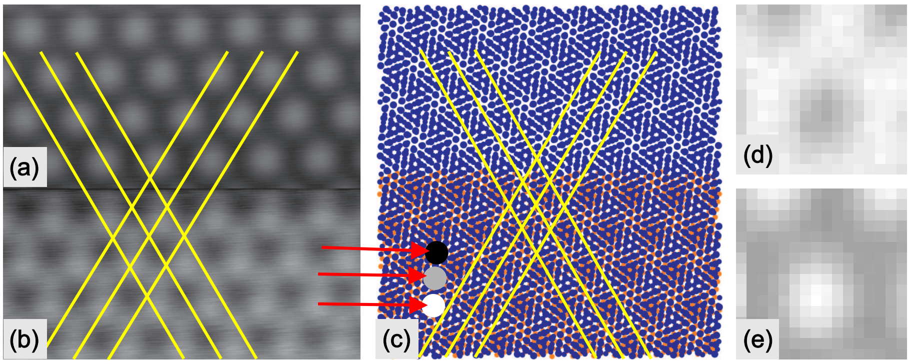

Figure 6.12: (a)/(b) $14\times14\,\mathrm{nm}^2$. The contrast of the moiré pattern in the STM image is reversed, when the bias voltage is switched from (a) 2.5 V to (b) 0.42 V during the scan. (c) Ball model of the observed patterns. The solid lines prove the contrast inversion. In the upper half the second layer of Ag atoms is not drawn. (d) $2.8\times2.8\,\mathrm{nm}^2$. The dI/dV-images of the moiré pattern at 2.8 V and (e) 2.5 V show that the contrast changes back again at higher sample voltages.

simplify the comparison of the patterns. The solid yellow lines indicate the inversion of the moiré contrast. Furthermore, the structure between the maxima that is visible in Fig. 6.12b has disappeared in Fig. 6.12a.

Fig. 6.12d and (e) show dI/dV maps of the moiré pattern at 2.8 V and 2.5 V, respectively. These maps reveal that the reversed contrast switches back again at 2.8 V. STS measurements with different tunneling resistances prove that the effect does not depend on the on the tip-sample distance. To investigate the nature of this evidently electronic effect STS measurements have been performed on the Pb overlayer. A strong peak around 2.7 V shown in Fig. 6.13a dominates the dI/dV spectrum. A zoom in the inset of Fig. 6.13a depicts two spectra recorded on top and beside the moiré maximum at 2.5 eV. A double peak structure appears where the peak at 2.66 V or at 2.76 V dominates depending on the lateral tip position. From DFT calculations for a free standing Pb monolayer [109] one can conclude that the strong feature in the dI/dV spectrum corresponds with the onset of the Pb $6p_{x,y}$-bands.

The splitting of this $6p$-resonance can be understood in terms of changing lateral interactions of the Pb atoms in the Pb overlayer. Analogous to the explanation of Grimm *et al.* for a Xe layer on graphite [110] the rotation of

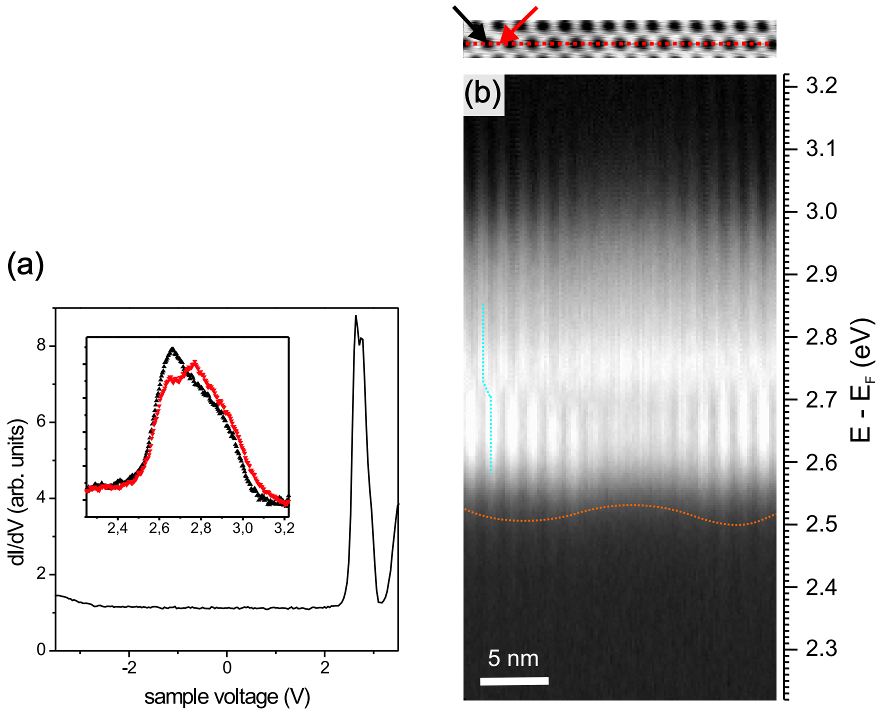

Figure 6.13: (a) dI/dV spectrum on the pure Pb phase. Inset: Zoom in the strong peak around 2.7 V: Two spectra at different positions as marked in (b) reveal the position dependence of the peak. (b) Plot of the differential conductance dI/dV for the pure Pb overlayer along the moiré maxima as function of the lateral distance x and of bias energy $E = eV$ with respect to E_F. The spectra are taken along the dashed red line in the topographic image above. Beside the contrast reversal one observes a long-range modulation of the band onset indicated by the dashed blue line.

the overlayer with respect to the substrate leads to a periodical change in the overlap of the Pb $6p$-orbitals. Thus the electron density varies periodically in the overlayer. One can assume that the overlap for Pb atoms sitting in hollow sites is larger than for the on-top positions. The higher electron density in these regions leads then to a band broadening and possibly an upward shift of the onset of the $6p_{x,y}$-band energy. Consequently, regions with high or low electron density show dark or bright contrast depending on the bias voltage and vice versa. The double peak structure is always visible in the dI/dV spectra independent from the tip position which indicates a large lateral extent of the respective wave functions.

The simple ball model gives an impression for the origin of the observed change in the inner structure of the moiré pattern. The atoms of the second Ag layer are not drawn in the first half of Fig. 6.12c. It is evident from that model that their electronic influence on the Pb overlayer generates the structure observed between the moiré maxima. Due to the fact that the moiré pattern in STM images originates from changes in the electronic structure and electron scattering at the nanometer sized interface modulations [111] the energy dependence of the electronic structure is considered to be responsible for the observed contrast change. The dI/dV spectrum in Fig. 6.13a implies a negligible contribution of the second Ag layer to the electronic properties of the overlayer when the $p_{x,y}$-bands dominate the local density of states. This observation corresponds with the fact, that no large overlap with substrate orbitals is expected for the $p_{x,y}$-bands because they extend mostly parallel to the surface. At low bias voltages on the other hand the electronic structure is expected to be dominated by s- and p_z-orbitals. First results of tight binding calculations indeed yield an sp_z hybridization around the Fermi level [97]. Thus, a significant overlap of these orbitals especially due to the strong substrate relaxation is expected and it is a plausible explanation for the change in the pattern structure.

6.3.2 An Additional Superstructure

The plot of the differential conductance $dI/dV(E, x)$ along the moiré maxima as function of the lateral distance x and of bias energy $E = eV$ with respect to E_F (Fig. 6.13b) reveals a long-range modulation of the 6p-band onset in addition to the alternating contrast. This modulation can be recognized in large scale topographic STM images as shown in Fig. 6.14a which is recorded at a bias voltage of 2.55 V. Bright maxima appear on the whole Pb overlayer with a spacing between 6 nm and 9 nm. The pattern seems to be influenced and distorted by defects in the overlayer that hinder a regular hexagonal order. This behavior is closely related to the 6p-band onset and must therefore have again an electronic origin.

As explanation for this phenomenon beating effects of interfering 6p-wave functions are suggested. The large lateral extend of the 6p-wave functions is indicated by the simultaneous detection of laterally differing onset energies as described above. A rough estimation for the effective mass of the

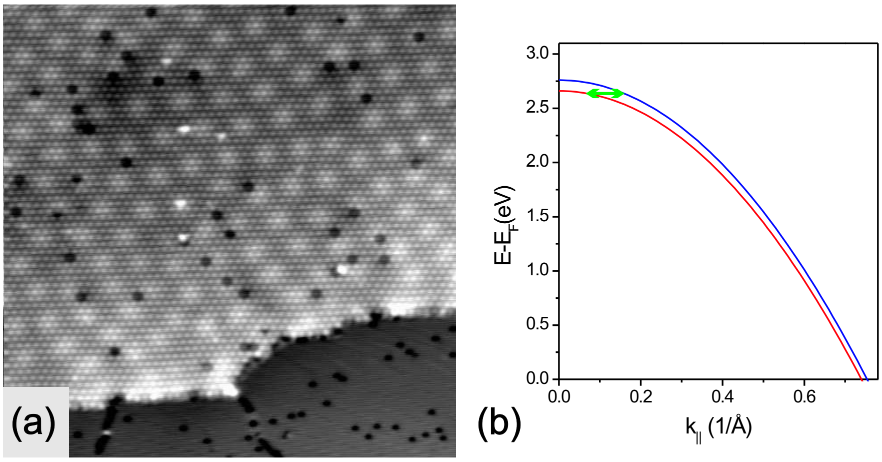

Figure 6.14: (a) 90×90 nm^2, 2.55 V The moiré pattern is superimposed by an additional periodic modulation of the surface. From Fig. 6.13b it can be associated with a periodic modulation of the onset energy of the $6p_{x,y}$-bands. (b) Schematic drawing of the site dependent $6p_{x,y}$-bands that might interfere due to the apparent large lateral extent of the wave functions.

$6p_{x,y}$-bands is achieved by extrapolating photoemission data of a Pb overlayer on Ag(111) [97] to the onset energy of the Pb $6p_{x,y}$-bands determined by STS by means of a parabolic fit. The resulting effective mass m^* is about $m^* = 4.9m_e$. The position dependent energy splitting of the $6p_{x,y}$-bands can be determined from the dI/dV spectra and is about 100 meV. The two bands that depend on the lateral position are drawn schematically in Fig. 6.14b. The beating around 2.6 eV caused by the interference of these bands is indicated in Fig. 6.14b by the green arrow. It leads to a modulation on a scale of about 8 nm which agrees very well with the periodicity observed in Fig. 6.14a.

6.4 Summary

Within this chapter several effects and phenomena regarding the electronic properties of the Pb/Ag(111) system have been elucidated.

The most striking discovery is the observation is a two-dimensional electronic state confined to the $(\sqrt{3} \times \sqrt{3}\,)$R30° surface alloy. This alloy state exhibits a quasi-free electron dispersion with a negative effective mass and has thus a completely different electronic structure than the Ag(111) surface state. The spin-orbit interaction gives rise to a strong band splitting which leads to a peak in the LDOS at the alloy state onset. This peak is detected by Scanning Tunneling Spectroscopy for the first time.

In the low coverage regime the universal phenomenon of the surface state localization at an impurity has been observed for a single Pb atom incorporated in the Ag(111) surface. It is the first reported observation of the bound state for a substitutional atom in the surface layer. This effect appears to broaden in the disordered alloy phase. It has been suggested that due to the interaction of the Pb atoms a new band evolves that leads with increasing coverage to the electronic state that governs the electronic properties of the well ordered $(\sqrt{3}\,\mathrm{x}\,\sqrt{3}\,)$R30° Pb/Ag surface alloy.

Finally, also the pure Pb overlayer yields remarkable electronic effects. A bias dependent reversal of the image contrast around 2.7 eV is explained by the lateral change of the $6p_{x,y}$-band onset energy. This change is believed to be the result of a periodical and site dependent variation of the electron density in the overlayer due to its incommensurate structure. The appearance of an additional superstructure superimposed to the moiré pattern at the $6p$-band onset is ascribed to the interaction of the energetically differing bands due to their large lateral extension. The periodicity of the superstructure can be nicely reproduced by considering beating effects of the respective electron waves.

Chapter 7

Conclusions and Outlook

The realization of a low temperature UHV-STM with 14 T magnet, capable of temperatures below 1 K by means of a cryostat with integrated Joule-Thomson cycle, has been described in Ch. 3. Single atom spectroscopy for Co adatoms on Au(100) and the measurement of the BCS gap of Pb demonstrate a performance with high spatial and spectroscopical resolution. Furthermore the image potential states of the Au(100) surface were found to be a sensitive probe for changes in the surface electronic structure caused by the quasi-hexagonal (5×27)-reconstruction (Ch. 4).

Experiments regarding the growth of Pb on Ag(111) and the characterization of the resulting structures by means of scanning tunneling spectroscopy (STS) show that low temperature STM is a great tool to discover new effects in the surface electronic structure with high spatial resolution. The submonolayer growth of Pb on Ag(111) has been studied in detail in Ch. 5. Pb is found to form a surface alloy within the first Ag surface layer. The results imply an alloying mechanism at room temperature similar to the one found for Sn on Cu(111). That is, pure Pb islands form upon Pb deposition, move across the Ag surface and randomly exchange Pb and Ag atoms on the way. By this, single atoms and clusters are incorporated in the surface and ordered $(\sqrt{3} \times \sqrt{3})$R30° Pb/Ag(111) surface alloy islands form on top.

Annealing leads to a complete incorporation of the Pb atoms in the Ag surface layer up to a coverage of 0.33 ML. At 0.33 ML the Pb atoms form a well ordered $(\sqrt{3} \times \sqrt{3})$R30° Pb/Ag(111) surface alloy structure that covers the whole surface. This alloy has been studied with atomic scale resolution by STM. At even higher coverages de-alloying dominates the growth process, the Pb atoms segregate to the surface and form a compact pure Pb overlayer. The overlayer induces a two-dimensional faceting of steps and island edges which offers a new way of assembling two phases in nanostructures. An example for that faceting induced nanostructuring are large surface alloy islands that evolve on large terraces during annealing at 520 K. At a coverage of 0.36 ML the pure Pb induces a reorientation of the islands facets. The higher stability of facets along substrate direction leads to a selective faceting which in turn results in an edge selective pure Pb formation.

Ch. 6 is a survey of the electronic properties of the Pb/Ag(111) system. First the observation of a two-dimensional electronic state confined to the ordered surface alloy is reported. In contrast to the well known Ag(111) surface state it shows a *p*-like electron dispersion with a negative effective mass. Photoemission experiments reveal furthermore a huge spin-splitting of that state which is about four times larger than the spin splitting of the Au(111) surface. A peak at the onset of the surface alloy state measured in STS can be ascribed to this spin splitting. This is in particular the first time, that spin splitting is detected by STS.

The interaction of single embedded Pb atoms with the Ag(111) surface state electrons leads to the formation of a bound state that shows up as resonance located just below the edge of the surface state onset. Defects and domain walls in the $(\sqrt{3} \times \sqrt{3})$R30° surface alloy interact in turn with electrons of the alloy state.

Finally, also the pure Pb phase shows remarkable electronic effects. A bias dependent reversal of the image contrast around 2.7 eV is explained by the lateral change of the $6p_{x,y}$-band onset energy. This change is believed to be the result of a periodical and site dependent variation of the electron density in the overlayer due to its incommensurate structure. The spatial variation of the electron density in turn leads to a laterally differing band onset. The appearance of an additional superstructure superimposed to the moiré pattern at the $6p$-band onset is consequently ascribed to the interaction of electron wave functions of these differing bands due to their large lateral extent. The periodicity of the superstructure can be nicely reproduced by considering beating effects of the respective electron waves.

Outlook

The possibility to completely alter the electronic properties of the Ag(111) surface by surface alloying opens up a new field of research. Beside Pb also other elements, Sb or Bi for example, are known to form an ordered

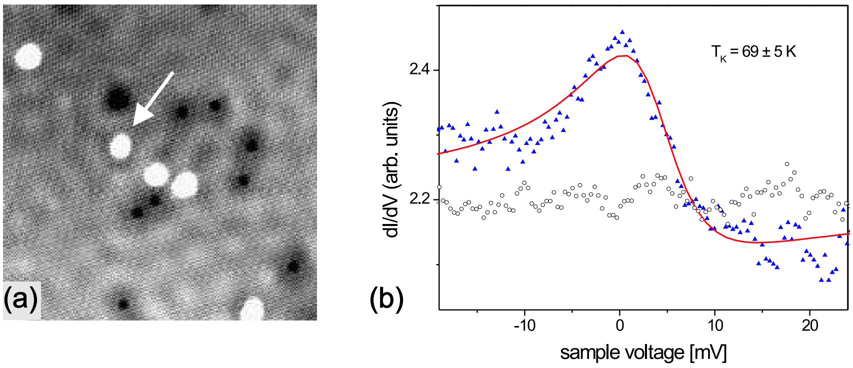

Figure 7.1: (a) Single Co adatoms on the surface alloy. (b) dI/dV-spectra taken on the Co atom marked with the white arrow (blue triangles) and on the bare alloy (black open circles). The red line depicts the fit of a Fano line shape to the data.

surface alloy phase on Ag(111) [55, 112, 113, 97], In forms an ordered phase on Cu(111) [114], Sn on Cu(111), Ni(111) and Pt(111) [115]. The detailed electronic structure of all these systems is still unknown. All elements just mentioned are in direct neighborhood to Pb in the periodic table. It can be expected that the electronic properties will depend greatly on the order realized in these systems and are different compared to disordered systems. Thus, a similar electronic state on their alloy phase and changes in the spin-splitting are quite probable. By this the surface alloy can act as a model system for a new form of two-dimensional electronic states. By altering the substrate and/or the alloying element, one can study the effect of the orbital overlap, the hybridization between adsorbate and substrate and the spin-splitting characteristics in the potential gradient at the surface.

Due to the influence of the surface state, the surface composition, and the geometrical surface structure on the chemical reactivity, different chemical properties of the surface alloy phase can also be expected. Further insights in this respect can be gained by the study of adsorption and dissociation of molecules on surface alloys [20, 19, 18].

An other interesting topic is the interaction of magnetic adatoms with the modified surface. First experiments in this context provide promising results.

The topographic STM image in Fig. 7.1a shows the ordered surface alloy layer with single Co atoms on top. The Co atoms have been evaporated in situ at about 20 K with a Co filament. The spectroscopical data in Fig. 7.1b are a dI/dV spectrum on top of the Co atom marked with a white arrow (blue triangles) and the "off-spectrum" on the bare surface alloy (black open circles). A narrow peak-like feature around the fermi energy can be observed at the adatom site while the spectrum stays flat on the surface alloy.

The red line fits a Fano line shape to the on-atom data. This Fano line shape is characteristic for the resonant interaction of an unpaired adatom spin with the conduction electrons of the nonmagnetic substrate, known as the Kondo effect [116]. A Kondo resonance shows up as a sharp peak in the local density of states which is pinned to the fermi energy and has a width proportional to the Kondo temperature T_K. The agreement between fit and experimental data is quite well. Therefore the observed feature can be identified as a Kondo resonance with a Kondo temperature $T_K = 69 \pm 5\,\mathrm{K}$ compared to 92 K on the bare Ag(111) surface.

Even though this value appears to be reasonable and might point towards a stronger hybridization that lowers T_K it is a preliminary result so far since the influence of the specific adsorption site might be substantial. The standing wave pattern around the investigated adatom indicates that the Co atom is located at a defect site, because in general the adatoms influence on the standing wave pattern is negligible. The detailed knowledge of the adatoms nearest neighbor configuration is of fundamental influence on T_K [116], therefore an appropriate discussion requires further results regarding reproducibility and site dependence of the observed Kondo resonance. A detailed study of the Kondo resonance on surface alloys may lead to a deeper understanding of the influence of the direct environment on the Kondo temperature and the line shape of the resonance and might enable to custom tailor new Kondo systems.

The new 1 K-UHV-STM-system with 14 T magnet offers the possibility to study all these new observations at very low temperatures and in high magnetic fields to gain deeper insights in the underlying physics and to discover new phenomena.

Bibliography

[1] G.Binnig, H. Rohrer, Ch. Gerber, and E. Weibel. Surface Studies by Scanning Tunneling Microscopy. *Physical Review Letters*, 49(1):57–61, 1982.

[2] V. Madhavan, W. Chen, T. Jamneala, M.F. Crommie, and N.S. Wingreen. Tunneling into a Single Magnetic Atom: Spectroscopic Evidence of the Kondo Resonance. *Science*, 280:567–569, 1998.

[3] H.H. Weitering, J.M Carpinelli, A.V. Melechko, J. Zhang, M. Barkowiak, and E.W. Plummer. Defect-Mediated Condensation of a Charge Density Wave. *Science*, 285:2107–2110, 1999.

[4] K.-F. Braun, S. Fölsch, G. Meyer, and K.-H. Rieder. Observation of Charge-Density Wave Domains on the Cr(110) Surface by Low-Temperature Scanning Tunneling Microscopy. *Physical Review Letters*, 85(16):3500–3503, 2000.

[5] M. Bode, S. Heinze, A. Kubetzka, O. Pietzsch, X. Nie, G. Bihlmayer, S. Blügel, and R. Wiesendanger. Magnetization-Direction-Dependent Local Electronic Structure Probed by Scanning Tunneling Spectroscopy. *Physical Review Letters*, 89(23):237205:1–4, 2002.

[6] O. Pietzsch, A. Kubetzka, M. Bode, and R. Wiesendanger. Observation of Magnetic Hysteresis at the Nanometer Scale by Spin-Polarized Scanning Tunneling Spectroscopy. *Science*, 292:2053–2056, 2001.

[7] M. Pratzer, H.J. Elmers, M. Bode, O. Pietzsch, A. Kubetzka, and R. Wiesendanger. Atomic-Scale Magnetic Domain Walls in Quasi-One-Dimensional Fe Nanostripes. *Physical Review Letters*, 87(12):127201–127204, 2001.

[8] Ali Yazdani, B.A. Jones, C.P. Lutz, M.F. Crommie, and D.M. Eigler. Probing the Local Effects of Magnetic Impurities on Superconductivity. *Science*, 275:1767–1770, 1997.

[9] Anatoli Polkovnikov, Subir Sachdev, and Matthias Vojta. Impurity in a d-Wave Superconductor: Kondo Effect and STM Spectra. *Physical Review Letters*, 86(2):296–4362, 2001.

[10] M. Jourdan, M. Huth, and H. Adrian. Superconductivity mediated by spin fluctuations in the heavy-fermion compound UPd_2Al_3. *Nature*, 398:47–49, 1999.

[11] K. Ishida, H. Mukuda, Y. Kitaoka, K Asayama, Z.Q. Mao, Y. Mori, and Y. Maeno. Spin-triplet superconductivity in Sr_2RuO_4 identified by ^{17}O Knight shift. *Nature*, 396:658–660, 1998.

[12] R. Matzdorf, Z. Fang, ISmail, J. Zhang, T. Kimura, Y. Tokura, K Terakura, and E.W. Plummer. Ferromagnetism Stabilized by Lattice Distortion at the Surface of the p-Wave Superconductor Sr_2RuO_4. *Science*, 289:746–748, 2000.

[13] W. Buckel and R. Kleiner. Supraleitung. *Wiley-VCH*, 2004.

[14] P. LeClair, J.S. Moodera, J. Philip, and D. Heimann. Coexistance of Ferromagnetism and Superconductivity in Ni/Bi Bilayers. *Physical Review Letters*, 95:037006:1–4, 2005.

[15] A.J. Heinrich, J.A. Gupta, C.P. Lutz, and D.M. Eigler. Single-Atom Spin-Flip Spectroscopy. *Science*, 306:466–469, 2004.

[16] J. Tersoff. Surface-confined Alloy Formation in Immiscible Systems. *Physical Review Letters*, 74(3):434–437, 1995.

[17] A. Christensen, A.V. Ruban, P. Stoltze, K.W. Jacobsen, H.L. Skriver, J.K. Nørskov, and F. Besenbacher. Phase diagrams for surface alloys. *Physical Review B*, 56(10):5822–5834, 1997.

[18] José A. Rodriguez. Physical and chemical properties of bimetallic surfaces. *Surface Science Reports*, 24:223–287, 1996.

[19] E. Bertel, P. Roos, and J. Lehmann. Promotion of catalytic reactions by depopulation of surface states. *Physical Review B*, 52(20):R14384–R14387, 1995.

[20] F. Besenbacher, I. Chorkendorff, B. S. Clausen, B. Hammer, A. M. Molenbroek, J . K. Nørskov, and I. Stensgaard. Design of a surface alloy catalyst for steam reforming. *Science*, 279(5358):1913–1915, 1998.

[21] J. Honolka. private communication.

[22] J. Tersoff and D.R. Hamann. Theory of the scanning tunneling microscope. *Physical Review B*, 31(2):805–813, 1985.

[23] G. Binnig, K.H. Frank, H. Fuchs, N. Garcia, B. Reihl, H. Rohrer, F. Salvan, and A.R. Williams. Tunneling Spectroscopy and Inverse Photoemission: Image and Field States. *Physical Review Letters*, 55(9):991–994, 1985.

[24] E.N. Smith and R.C. Richardson. Experimental techniques in Condensed Matter Physics at Low Temperatures. *Addison Wesley*, 1988.

[25] C. Wittneven, R. Dombrowski, S. H. Pan, and R. Wiesendanger. A low-temperature ultrahigh-vacuum scanning tunneling microscope with rotatable magnetic field. *Review of Scientific Instruments*, 68(10):3806–3810, 1993.

[26] S. H. Pan. Piezo-electric motor, international Patent publications No. WO93\19494, International Bureau, World Intellectual Property Organization (30. Sept. 1993).

[27] W. Chen, V. Madhavan, T. Jamneala, and M.F. Crommie. Scanning Tunneling Microscopy Observation of an Electronic Superlattice at the Surface of Clean Gold. *Physical Review Letters*, 80(7):1469–1472, 1998.

[28] Paniago, R. Matzdorf, G. Meister, , and A. Goldmann. Temperature-dependence of Shockley type surface-energy bands on Cu(111), Ag(111) and Au(111). *Surface Science*, 336(1-2):113–122, 1995.

[29] A.C. Hewson. The Kondo problem to heavy fermions. *Cambridge University Press*, 1993.

[30] J. Bardeen, L.N. Cooper, and J.R. Schrieffer. Theory of Superconductivity. *Physical Review*, 108(5):1175–1204, 1957.

[31] L. Kuipers, M. S. Hoogemann, and J.W.M. Frenken. Jump to Contact and Neck Formation between Pb Surface and a STM Tip. *Surface Science*, 340(3):231–244, 1995.

[32] Ch. Renner, Ph. Niedermann, A.D. Kent, and Ø. Fischer. A vertical piezoelectric inertial slider. *Review of Scientific Instruments*, 61(3):965–967, 1990.

[33] U. Höfer, I.L. Shumay, Ch. Reuß U. Thomann, W. Wallauer, and Th. Fauster. Time-Resolved Coherent Photoelectron Spectroscopy of Quantized Electronic States on Metal Surfaces. *Science*, 277:1480–1482, 1997.

[34] P.M. Echenique and J.B. Pendry. The existence and detection of Rydberg states at surfaces. *Journal of Physics C: Solid State Physics*, 11:2065–2075, 1978.

[35] A. Goldmann, V. Dose, and G. Borstel. Empty electronic states at the (100), (110), and (111) surfaces of nickel, copper, and silver. *Physical Review B*, 32(4):1971–1980, 1985.

[36] F.J. Himpsel and J.E. Ortega. Electronic structure of Cu(100), Ag(100), and $Cu_3Au(100)$ from inverse photoemission. *Physical Review B*, 46(15):9719–9723, 1992.

[37] W. Berthold, U. Höfer, P. Feulner, E.V. Chulkov, V.M. Silkin, and P.M. Echenique. Momentum-Resolved Lifetimes of Image-Potential States on Cu(100). *Physical Review Letters*, 88(5):056805:1–4, 2002.

[38] Ch. Reuß I.L. Shurnay, U. Thomann, M. Kutschera, M. Weinelt, Th. Fauster, and U. Höfer. Control of the Dephasing of Image-Potential States by CO Adsorption on Cu(100). *Physical Review Letters*, 82(1):153–156, 1999.

[39] P. Wahl, M. A. Schneider, L. Diekhöner, R. Vogelgesang, and K. Kern. Quantum Coherence of Image-Potential States. *Physical Review Letters*, 91(10):106802:1–4, 2003.

[40] T. Jung, Y.W. Mo, and F.J. Himpsel. Identification of Metals in Scanning Tunneling Microscopy via Image States. *Physical Review Letters*, 74(9):1641–1644, 1995.

[41] Y.J. Choi, I.C. Jeong, J.-Y. Park, S.-J. Kahng, J. Lee, and Y. Kuk. Surface alloy formation of Fe on Cr(100) studied by scanning tunneling microscopy. *Physical Review B*, 59(16):10918–10922, 1999.

[42] F. Ercolessi, E. Tosatti, and M. Parinello. Au(100) Surface Reconstruction. *Physical Review Letters*, 57(6):719–722, 1985.

[43] J.F. Jia, K. Inoue, Y. Hasegawa, W.S. Yang, and T. Sakurai. Variation of the local work function at steps on metal surfaces studied with STM. *Physical Review B*, 58(3):1193–1196, 1998.

[44] R. Smoluchowski. Anisotropy of the Electronic Work Function of Metals. *Physical Review*, 60:661–674, 1941.

[45] H. Ishida and A. Liebsch. Calculation of the electronic structure of stepped metal surfaces. *Physical Review B*, 46(11):7153–7156, 1992.

[46] José A. Rodriguez. Metal-metal bonding on surfaces: molecular orbital study of Pd/Ti(001) and Pd/Ru(001). *Surface Science*, 303:366–376, 1994.

[47] H. Brune. Microscopic view of epitaxial metal growth: nucleation and aggregation. *Surface Science Reports*, 31(4-6):121–229, 1998.

[48] Z. Zhang and M.G Lagally. Atomic Processes in the Early Stages of Thin-Film Growth. *Science*, 276:377–383, 1997.

[49] L.P. Nielsen, F. Besenbacher, I. Stensgaard, E. Laegsgaard, C. Engdahl, P. Stoltze, K.W. Jacobsen, and J.K. Nørskov. Initial growth of Au on Ni(110): Surface alloying of immiscible metals. *Physical Review Letters*, 71(7):754, 1993.

[50] L.P. Nielsen, F. Besenbacher, I. Stensgaard, E. Laegsgaard, C. Engdahl, P. Stoltze, and J.K. Nørskov. "Dealloying" Phase Separation during Growth of Au on Ni(110). *Physical Review Letters*, 74(9):1159, 1995.

[51] M. J. Gibson K. J. Rawlings and P. J. Dobson. Epitaxial-growth of lead and thallium on (111) silver and copper. *Journal of Physics D: Applied Physics*, 11(14):2058, 1978.

[52] Kai-Felix Braun. Investigation of surfaces and atomic manipulation with a scanning tunnelling microscope at low temperature. *PhD thesis, FU Berlin*, 2001.

[53] C. Nagl, O. Haller, E. Platzgummer, M. Schmid, and P. Varga. Submonolayer Growth of Pb on Cu(111) - Surface Alloying and De-Alloying. *Surface Science*, 321(3):237–248, 1994.

[54] R. Q. Hwang A. K. Schmid, N. C. Bartelt. Alloying at surfaces by the migration of reactive tow-dimensional islands. *Science*, 290(5496):1561–1564, 2000.

[55] D.P. Woodruff and J. Robinson. Some structural issues in surface alloys and alloy surfaces: rumpling, stacking faults and disorder. *Applied Surface Science*, 219(16):1–10, 2003.

[56] H. M. Polatoglou, M. Methfessel, and M. Scheffler. Vacancy-formation energies at the (111) surface and in bulk Al, Cu, Ag and Rh. *Physical Review B*, 48(3):1877–1882, 1993.

[57] H. Brune, K. Bromann, H. Röder, K. Kern, J. Jacobsen, P. Stoltze, K. Jacobsen, and J. Nørskov. Effect of strain on surface diffusion and nucleation. *Physical Review B*, 52(20):R14380–R14383, 1995.

[58] C. Ratsch, A.P. Seitsonen, and M. Scheffler. Strain dependence of surface diffusion: Ag on Ag(111) and Pt(111). *Physical Review B*, 55(11):6750–6753, 1997.

[59] J. Camarero, J. Ferrón, V. Cros, L. Gómez, A. L. Vázquez de Parga, J. M. Gallego, J. E. Prieto, J. J. Miguel, and R. Miranda. Atomic Mechanism of Surfactant-Assisted Epitaxial Growth. *Physical Review Letters*, 81(4):850–853, 1998.

[60] J.E. Prieto, J. de la Figuera, and R. Miranda. Surface energetics in a heteroepitaxial model system: Co/Cu(111). *Physical Review B*, 62(3):2126–2133, 2000.

[61] S. Oppo, V. Fiorentini, and M. Scheffler. Theory of Adsorption and Surfactant Effect of Sb on Ag(111. *Physical Review Letters*, 71(15):2437–2440, 21993.

[62] S.A de Vries, W.J. Huismann, P. Goedkindt, M.J. Zwanenburg, S.L. Bennett, I.K. Robinson, and E. Vlieg. Surface atomic structure of the $(\sqrt{3} \times \sqrt{3})$R30°-Sb reconstructions of Ag(111) and Cu(111). *Surface Science*, 414:159–169, 1998.

[63] R.J. Baxter. Exactly solved Models in Statistical Mechanics, Academic Press, London. 1982.

[64] M.L. Anderson, M. J. D'Amat, P. J. Feibelman, and B. S. Swartzentruber. Vacancy-Mediated and Exchange Diffusion in a Pb/Cu(111) Surface Alloy: Concurrent Diffusion on Two Length Scales. *Physical Review Letters*, 90(12):126102:1–4, 2003.

[65] R. van Gastel, E. Somfai, S.B. van Albada, W. van Saarloos, and J.W.M. Frenken. Nothing Moves a Surface: Vacancy Mediated Surface Diffusion. *Physical Review Letters*, 86(8):1562–1565, 2001.

[66] J.W.M. Frenken, R. van Gastel, S.B. van Albada, E. Somfai, and W. van Saarloos. Diffusion in a surface: the atomic slide puzzle. *Applied Physics A*, 75:11–15, 2002.

[67] N. Knorr, H. Brune, M. Epple, A. Hirstein, M.A. Schneider, and K. Kern. Long-range adsorbate interactions mediated by a two-dimensional electron gas. *Physical Review B*, 65:115420:1–5, 2002.

[68] J. Repp, F. Moresco, G. Meyer, and K.-H. Rieder. Substrate Mediated Long-Range Oscillatory Interaction between Adatoms: Cu/Cu(111). *Physical Review Letters*, 85:2981–2984, 2000.

[69] P. Zeppenfeld, Klaus Kern, Rudolf David, and George Comsa. Diffraction from domain-wall systems. *Physical Review B*, 38(6):3918–3924, 1988.

[70] H. Hong, R.J. Birgeneau, and M. Sutton. Low-temperature structures of Xe on graphite in the one- to two-layer regime. *Physical Review B*, 33(5):3344, 1986.

[71] C. Nagl, M. Schmid, and P. Varga. Inverse corrugation and corrugation enhancement of Pb superstructures on Cu(111) and (110). *Surface Science*, 159-168:369, 1996.

[72] A. D. Novaco and J. P. McTague. Orientational Epitaxy - the Orientational Ordering of Incommensurate Structures. *Physical Review Letters*, 38(22):1286–1289, 1977.

[73] T. Wiederholt, H. Brune, J. Wintterlin, R. J. Behm, and G. Ertl. Formation of a 2-dimensional sulfide phase on Al(111) - an STM study. *Surface Science*, 324(2-3):91–105, 1995.

[74] M. Bohringer, R. Berndt, and W.D. Schneider. Transition from three-dimensional to two-dimensional faceting of Ag(110) induced by Cu-phthalocyanine . *Physical Review B*, 55(3):1384–1387, 1997.

[75] S. Rousset, S. Gauthier, O. Siboulet, W. Sacks, M. Belin, and J. Klein. Scanning-Tunneling-Microscopy Observation of Adsorbate-Induced Two-Dimensional Step Faceting on the S/Cu(111) Surface. *Physical Review Letters*, 63(12):1265–1268, 1989.

[76] E. Kopatzki and R.J. Behm. Step Faceting: Origin of the Temperature Dependent Induction Period in Ni(100) Oxidation. *Physical Review Letters*, 74(8):1399–1402, 1995.

[77] N. Memmel and E. Bertel. Role of surface states for the epitaxial growth on metal surfaces. *Physical Review Letters*, 75(3):485–488, 1995.

[78] José A. Rodriguez and D. Wayne Goodman. The Nature of the Metal-Metal Bond in Bimetallic Surfaces. *Science*, 257:897–903, 1992.

[79] S. LaShell, B.A. McDougall, and E. Jensen. Spin Splitting of an Au(111) Surface State Band Observed with Angle Resolved Photoelectron Spectroscopy. *Physical Review Letters*, 77(16):3419–3422, 1996.

[80] L. Petersen and P. Hedegård. A simple tight-binding model of spin-orbit splitting of *sp*-derived surface states. *Surface Science*, 459:49–56, 2000.

[81] Jiutao Li, Wolf-Dieter Schneider, and Richard Berndt. Local density of states from spectroscopic scanning-tunneling-microscope images: Ag(111). *Physical Review B*, 56(12):7656–7659, 1997.

[82] O. Jeandupeux, L. Bürgi, A. Hirstein, H. Brune, and K. Kern. Thermal damping of quantum interference patterns of surface-state electrons. *Physical Review B*, 59(24):15926–15934, 1999.

[83] G. Nicolay, F. Reinert, S. Schmidt, D. Ehm, P. Steiner, and S. Hüfner. Natural lindewidth of the Ag(111) L-gap surface state as determined by photoemission spectroscopy. *Physical Review B*, 62(3):1631–1634, 2000.

[84] G. Nicolay, F. Reinert, S. Hüfner, and P. Blaha. Spin-orbit splitting of the L-gap surface state on Au(111) and Ag(111). *Physical Review B*, 65(3):33407:1–4, 2001.

[85] F. Reinert, G. Nicolay, S. Schmidt, D. Ehm, and S. Hüfner. Direct measurements of the L-gap surface states on the (111) face of noble metals by photoelectron spectroscopy. *Physical Review B*, 63(11):115415–115421, 2001.

[86] Jiutao Li, Wolf-Dieter Schneider, Richard Berndt, and S. Crampin. Electron Confinement to Nanoscale Ag Islands on Ag(111): A Quantitative Study. *Physical Review Letters*, 80(15):3332–3335, 1998.

[87] H. Hövel, B. Grimm, and B. Reihl. Modification of the Shockley-type surface state on Ag(111) by an adsorbed xenon layer. *Surface Science*, 477:43–49, 2001.

[88] F.J. Palomares, M. Serrano, A. Ruiz, F. Soria, K. Horn, and M. Alonso. ARPES study of the surface states from Au/Ag(111): evolution with coverage and photon energy. *Surface Science*, 513:283–294, 2002.

[89] Karina Morgenstern, Kai-Felix Braun, and Karl-Heinz Rieder. Surface-State Depopulation on Small Ag(111) Terraces. *Physical Review Letters*, 89(22):226801:1–4, 2002.

[90] C. Kittel. Quantum Theory of Solids, Wiley, New York. 1963.

[91] H. Cercellier, Y. Fagot-Revurat, B. Kierren, F. Reinert, D. Popović, and D. Malterre. Spin-orbit splitting of the Shockley state in the Ag/Au(111) interface. *Physical Review B*, 70:193412:1–4, 2004.

[92] E. Rotenberg, J.W. Chung, and S.D. Kevan. Spin-Orbit Induced Surface Band Splitting in Li/W(110) and Li/Mo(110. *Physical Review Letters*, 82:4066–4069, 1999.

[93] Y.M. Koroteev, G. Bihlmayer, J.E. Gayone, E.V. Chulkov, S. Blügel, P.M. Echenique, and Ph. Hofmann. Strong Spin-Orbit Splitting on Bi Surfaces. *Physical Review Letters*, 93:046403:1–4, 2004.

[94] J.I. Pascual, G. Bihlmayer, Yu M. Koroteev, H.-P. Rust, G. Ceballos, M. Hansmann, K. Horn, E.V. Chulkov, S. Blügel, P.M. Echenique, and Ph. Hofmann. Role of Spin in Quasiparticle Interference. *Physical Review Letters*, 93(19):196802:1–4, 2004.

[95] L. Peterson, P. T. Sprunger, Ph. Hofmann, E. Lægsgaard, B. G. Briner, M. Doering, H.-P. Rust, A. M Bradshaw, F. Besenbacher, and E. W. Plummer. Direct imaging of the two-dimensional Fermi contour: Fourie-transform STM. *Physical Review B*, 57(12):R6858–R6861, 1998.

[96] A.P. Seitsonen. private communication.

[97] C. Ast. private communication.

[98] N.D. Lang. Spectroscopy of single atoms in the scanning tunneling microscope. *Physical Review B*, 34(8):5947–5950, 1986.

[99] N.D. Lang. Apparent Size of an Atom in the Scanning Tunneling Microscope as a Function of Bias. *Physical Review Letters*, 58(1):45–48, 1987.

[100] J. Nieminen, S. Lahti, S. Paavilainen, and K. Morgenstern. Contrast changes in STM images and relations between different tunneling models. *Physical Review B*, 66:165421:1–9, 2002.

[101] F. Calleja, A. Arnau, J.J. Hinarejos, A.L. V*á*zquez de Parga, W.A. Hofer, P.M. Echenique, and R. Miranda. Contrast Reversal and Shape Changes of Atomic Adsorbates Measured with Scanning Tunneling Microscopy. *Physical Review Letters*, 92(20):206101:1–4, 2004.

[102] L. Limot, E. Pehlke, J. Krger, and R. Berndt. Surface-State Localization at Adatoms. *Physical Review Letters*, 94(3):036805:1–4, 2005.

[103] Ph. Avouris, I. W. Lyo, and P. Molinàs-Mata. STM studies on the interaction of surface state electrons on metals with steps and adsorbates. *Chemical Physics Letters*, 240:423–428, 1995.

[104] F.E. Olsson, M. Persson, A.G. Borisov, J.-P. Gauyacq, J. Lagoute, and S. Fölsch. Localization of the Cu(111) Surface State by Single Cu Adatoms. *Physical Review Letters*, 93(20):206803:1–4, 2004.

[105] B. Simon. Bound-State of Weakly Coupled Schrodinger Operators in One and Two Dimensions. *Annals of Physics (N.Y.)*, 97:279–288, 1976.

[106] D.M. Newns. Self-Consistent Model of Hydrogen Chemisorption. *Physical Review*, 178(3):1123–1135, 1969.

[107] Jiutao Li, Wolf-Dieter Schneider, Richard Berndt, O.R. Bryant, and S. Crampin. Surface-State Lifetime Measured by Scanning Tunneling Spectroscopy. *Physical Review Letters*, 81(20):4464–4467, 1998.

[108] A. Biedermann, O. Genser, W. Hebenstreit, M. Schmid, J. Redinger, R. Podloucky, and Peter Varga. Scanning Tunneling Spectroscopy of One-Dimensional Surface States on a Metal Surface. *Physical Review Letters*, 76(22):4179–4182, 1996.

[109] F. Baumberger, A. Tamai, M. Muntwiler, T. Greber, and J. Osterwalder. The electronic structure of a surfactant layer: Pb/Cu(111). *Surface Science*, 532:82–86, 2003.

[110] B. Grimm, H. Hövel, M. Pollmann, and B. Reihl. Physisorbed Rare-Gas Monolayers: Evidence for Domain-Wall Tilting. *Physical Review Letters*, 83(5):991–994, 1999.

[111] K. Kobayashi. Moiré pattern in scanning tunneling microscopy: Mechanism in observation of subsurface nanostructures. *Physical Review B*, 53(16):11091–11099, 1996.

[112] T.C.Q. Noakes, D.A. Hutt, C.F. McConville, and D.P. Woodruff. Structural investigation of ordered Sb adsorption phases on Ag(111) using coaxial impact collision ion scattering spectroscopy. *Surface Science*, 372:117–131, 1997.

[113] E.A. Soares, C. Bittencourt, V.B. Nascimento, V.E. de Carvalho, C.M.C. de Castilho andC.F. McConville, A.V. de Carvalho, and D.P. Woodruff. Structure determination of Ag(111) $(\sqrt{3} \times \sqrt{3}\,)$R30°-Sb by low-energy electron diffraction. *Physical Review B*, 61(20):13983–13987, 2000.

[114] H. Wider, V. Gimple, W. Eveson, G. Schatz, J. Jaworski, J. Prokop, and M Marszalek. Surface alloying of indium on Cu(111). *Journal of Physics: Condensed Matter*, 15:1909–1919, 2003.

[115] S.H. Overbury and Yi sha Ku. Formation of stable, two-dimensional alloy-surface phases: Sn on Cu(111), Ni(111), and Pt(111). *Physical Review B*, 46(12):7868–7872, 1992.

[116] P. Wahl, L. Diekhöner, M. A. Schneider, L. Vitali, G. Wittich, and K. Kern. Kondo Temperatur of Magnetic Impurities at Surfaces. *Physical Review Letters*, 93(17):176603:1–4, 2004.

Danksagung

Zum Schluss danke ich all jenen, die zum Gelingen dieser Arbeit beigetragen haben bzw. sie erst ermöglicht haben:

- Prof. Dr. Klaus Kern für die Bereitstellung des Themas
- Prof. Dr. G. Schatz und Prof. Dr. M. Fuchs von der Universität Konstanz für ihre prompte Bereitschaft als Gutachter und Prüfer für meine Arbeit zu fungieren
- Alexander Schneider für die Betreuung der Doktorarbeit
- Christian Ast für die tatkräftige Hilfe während der drei Monate, die er beim STM-Aufbau dabei war, und für die Einführung in die Synchrotron-Welt.
- Peter Wahl, Christian Ast, Ralf Vogelgesang, Lucia Vitali, Lars Diekhöner und Alexander Schneider für anregende Diskussionen
- Der Tieftemperaturservicegruppe um Jürgen Kienle für die stete Bereitschaft zu außerplanmäßiger Hilfe, für ein immer offenes Ohr in allen Belangen und die tolle Zusammenarbeit
- Wolfgang Stiepany für seine Hilfsbereitschaft und Mithilfe
- Peter Wahl, Christian Ast, Ralf Vogelgesang, Lars Diekhöner, Dominik Hoffmann und vielen mehr für ihre angenehme, freundschaftliche, aufmunternde, unterstützende, ... Gesellschaft während der letzten Jahre

Mein größter Dank gilt meiner Frau Almut für ihr Verständnis und ihren Rückhalt und meinen Eltern, die mich immer unterstützt, gefördert und auf meinem Weg begleitet haben.